Alma Mater Studiorum · Università di Bologna

Scuola di Scienze
Corso di Laurea Magistrale in Fisica

Quantum transport in monolayer WTe_2

Relatore:
Prof.ssa Daniela Cavalcoli

Presentata da:
Giulia Tenasini

Correlatore:
Prof. Alberto Morpurgo

Sessione II
Anno Accademico 2016/2017

A miei meravigliosi genitori
Vilma e Alfredo

"There's Plenty of Room at the Bottom."

Richard Feynman

Abstract

Tungsten ditelluride (WTe_2) belongs to the family of transition metal dichalcogenides (TMDs), which plays nowadays a prominent role, besides graphene, in the research field of two-dimensional (2D) materials. Thanks to a layered structure with van der Waals interactions between different planes, these materials can be indeed easily exfoliated down to atomically thin thickness, when electronic properties are often drastically different from the bulk.
Monolayer WTe_2 has recently attracted attention because of the theoretical prediction to be a two-dimensional topological insulator (TI) in presence of strain. TIs are a novel class of materials characterized by an insulating bulk and unconventional conducting states at their physical boundaries, referred as helical states. Although edge conduction consistent with a 2D TI, also dubbed Quantum Spin Hall insulator, has already been experimentally observed in quantum wells heterostructures of semiconductors, the systems analysed so far still present several puzzles. Realization of a 2D TI in monolayers TMD would be a breakthrough due to the wide availability and great versatility of these materials, allowing considerable advantages in the study of this exotic state of matter.

In the present work we aim at studying the transport properties of monolayer WTe_2 in suitable nano-fabricated devices. Since the material is not completely stable in air, the oxidation of the surface significantly affects transport in few layers crystals, leading to a disorder induced metal-insulator transition. A possible solution to prevent the degradation, preserving at the same time the crystal quality, is an encapsulation of monolayer WTe_2 between layers of an inert 2D material, like hexagonal boron nitride (hBN). In that respect, one of the main goal of this experimental work was to develop a transfer technique which allows to pick up and align with micrometric precision different layers of atomically thin crystals in van der Waals heterostructures and contact the encapsulated flake electrically.
Selected samples are investigated by means of magnetotransport down to 0.250 K. Our measurements show the the presence of a gap in encapsulated monolayer WTe_2 below temperatures of ~100 K, whose order of magnitude is in accordance with results obtained by angle resolved photo emission spectroscopy (ARPES) and scanning tunnel microscopy (STM). In addition, the detection of a non-zero current inside the bulk bandgap, with a fairly constant value independent from gate voltage, constitutes a strong hint of edge conduction. Non-local measurements in different configurations support the hypothesis of helical edge states, following a trend in agreement with what is predicted by the Landauer-Büttiker formalism. The measured two-terminal conductance ($\sim 0.33\ e^2/h$), consistent with the value obtained by others research groups, is smaller than the one expected for an ideal 2D topological insulator. The reduced values of the conductance, confirmed also by non-local measurements, are probably linked to a suppression of

the edge current whose precise origin is still unknown. A possibility is that in these nano-devices the contacts quality has a non-neglecting influence on the transmission of electrons from the metal to the edge states, located at the boundaries of the crystal.
Then, data relative to encapsulated WTe_2 monolayers devices provide evidence of edge current, consistently with a scenario of a 2D topological insulator. Nevertheless, the absence of a precise conductance quantization confirms the puzzling nature of the quantum spin Hall effect and suggests that improving contacts in these devices could be a key step in the direction of a better comprehension of the phenomenon.

Il ditellurio di tungsteno (WTe_2) appartiene alla classe dei dicalcogenuri di metalli di transizione (TMDs), che rappresentano attualmente i materiali più promettenti, insieme al grafene, nel campo di ricerca dei cristalli bidimensionali (2D). Grazie ad una caratteristica struttura stratificata, in cui i diversi piani atomici sono legati da deboli interazioni di van der Waals, mediante esfoliazione meccanica è possibile isolare strati di spessore quasi-atomico di TMDs, detti "monostrati", con proprietà spesso molto differenti dal materiale *bulk* originario.
Il WTe_2, nella sua forma a monostrato, è stato recentemente oggetto di un acceso interesse scientifico, in quanto teoricamente predetto essere un isolante topologico (TI) bidimensionale -anche conosciuto come stato di hall quantistico di spin- in presenza di *strain*. Un isolante topologico è un materiale che internamente si comporta come un isolante elettrico ma che sulla superficie manifesta stati conduttivi, denominati stati elicoidali. Nonostante una conduzione localizzata sui bordi consistente con l'ipotesi di isolante topologico 2D sia già stata sperimentalmente osservata in pozzi quantici formati da eterostrutture di semiconduttori, i sistemi analizzati fino a questo momento lasciano ancora aperti molti interrogativi. Data la vasta disponibilità e versatilità di questi cristalli, l'identificazione di un monostrato di TMD come isolante topologico 2D costituirebbe una svolta, consentendo notevoli vantaggi nello studio di questo insolito stato della materia.

Lo scopo di questa tesi è studiare le proprietà si trasporto di monostrati di WTe_2 in microdispositivi realizzati con opportune tecniche di nanofabbricazione. L'ossidazione della superficie esterna del WTe_2, dovuta ad una non-perfetta stabilità in aria, influenza significativamente il trasporto elettronico in cristalli costituiti da pochi strati atomici ed è causa di una transizione metallo-isolante. Una possibile soluzione per evitare la degradazione del materiale e al contempo preservare la qualità del cristallo consiste nell' "incapsulamento" di un monostrato di WTe_2 fra materiali 2D chimicamente inerti, come il nitruro di boro esagonale (hBN). A tale proposito, uno degli obiettivi principali di questo lavoro sperimentale è stato lo sviluppo di una tecnica di "trasferimento" che permette di sollevare e allineare con precisione micrometrica strati di spessore atomico di differenti materiali, assemblando eterostrutture di van der Walls.
Campioni selezionati sono studiati mediante misure di magneto-transporto a bassa temperatura (fino a 0.250 K). I dati analizzati evidenziano, per temperature al di sotto di ~ 100 K, l'esistenza di un *gap* di energia in monostrati di WTe_2 il cui ordine di grandezza risulta in accordo con risultati ottenuti tramite spettroscopia di fotoemissione risolta in angolo (ARPES) e microscopia a effetto tunnel (STM). Inoltre, la presenza di una corrente non nulla e independente dal voltaggio di gate applicato, nella regione corrispondente al gap del materiale bulk, costituisce un forte segnale di conduzione localizzata sui bordi. L'ipotesi di stati di bordo elicoidali è supportata da misure di resistenza non-locali in differenti configurazioni, che seguono l'andamento predetto dal formalismo di Landauer-Büttiker. La conduttanza a due terminali ($\sim 0.33\ e^2/h$), consistente con il risultato ottenuto da altri gruppi sperimentali, risulta minore rispetto alla predizione teorica per un isolante topologico ideale 2D. Valori ridotti della conduttanza, confermati anche da misure non-locali, sono probabilmemte legati ad una soppressione della corrente di bordo, la cui origine precisa è ancora ignota. Una possibilità è che in questi nano-dispositivi la qualità dei contatti abbia un'influenza non trascurabile sulla trasmissione degli elettroni dal metallo agli stati di bordo localizzati sulle superfici del cristallo.
Quindi, i dati relativi a campioni sperimentali con monostrato di WTe_2 propriamente incapsulato dimostrano l'esistenza di una corrente localizzata ai bordi del sistema, coerentemente con

l'ipotesi di un isolante topologico 2D. Tuttavia l'assenza di una precisa quantizzazione della conduttanza se da un lato sottinea come, ancora una volta, l'effetto Hall quantistico di spin non sia del tutto compreso, dall'altro suggerisce come il miglioramento dei contatti in questi dispositivi possa rivestire un ruolo chiave nella direzione di una migliore comprensione del fenomeno.

Contents

1 Introduction **1**
1.1 2D Materials . . . 2
1.2 Topological Insulators . . . 5
1.3 QSHE in WTe_2 monolayer . . . 7
1.4 Motivation and outline . . . 8

2 Electronic transport in mesoscopic systems **11**
2.1 Gate modulated transport in nano-devices . . . 11
2.2 Characteristic lengths . . . 13
2.3 Landauer-Büttiker formalism . . . 14
2.3.1 Landauer formula . . . 15
2.3.2 Finite temperature case . . . 17
2.3.3 Multi-terminal generalization . . . 17
2.4 Quantum interference effects . . . 18
2.4.1 Weak localization . . . 19
2.4.2 Weak anti-localization . . . 21
2.4.3 Universal Conductance Fluctuations . . . 22
2.5 The Quantum Hall Effect . . . 23
2.5.1 Classical magnetotransport . . . 24
2.5.2 Landau levels . . . 26
2.5.3 IQHE . . . 28
2.5.4 Shubnikov-de Haas oscillations . . . 31
2.5.5 Topological nature of the QHE . . . 33
2.6 The Quantum Spin Hall Effect . . . 34
2.6.1 Spin-orbit interaction . . . 35
2.6.2 Protected helical edge states . . . 36
2.6.3 Transport of edge states . . . 37

3 WTe_2: from bulk to thin layers **43**
3.1 A compensated semimetal . . . 43
3.2 Thickness evolution of magnetotransport . . . 46
3.3 Edge states in monolayer T'-WTe_2 . . . 49

4 WTe_2 monolayer devices **53**
4.1 General aspects of nanofabrication 53
4.1.1 Substrate preparation 53
4.1.2 Micro-mechanical cleaving 54
4.1.3 Atomically thin crystals characterization 55
4.1.4 Metal contacts 58
4.2 Transfer technique 62
4.2.1 Transfer set up 64
4.3 Heterostructures 66
4.3.1 Platinum contacts on bottom hBN 66
4.3.2 Tunnel contacts through monolayer MoS_2 67

5 Electronic properties of WTe_2 crystals **69**
5.1 Measurement set-up 69
5.1.1 The cryostat 69
5.1.2 The insert 70
5.1.3 Measurement instrumentation 72
5.2 Characterization of bulk samples 72
5.3 Edge conduction in monolayer WTe_2 76
5.3.1 Observation of a gap 79
5.3.2 Non-local measurements 82
5.4 Results 84

Conclusions **84**

Acknowledgments **86**

Bibliography **90**

Chapter 1

Introduction

Condensed matter physics studies how simple particles, as ions or electrons, interact with each others and combine together to form different phases like crystalline solids and magnets, depending on external factors or intrinsic properties of the materials. The *Landau-Ginzburg theory* gives an universal description of these ordered states of matter in terms of *symmetry breaking*: in a crystal the lattice periodicity breaks the continuous symmetry of space under rotations and translations, while in magnets the privileged orientation of magnetic moments breaks some of the rotational symmetry of spin space and the time-reversal symmetry. According to this theory, a high-temperature symmetric state experiences a phase transition to a low-temperature, less-symmetric, symmetry-broken state, characterized by a peculiar *order parameter* with a non-vanishing expectation value.
The study of *Quantum Hall Effect* in 1980 led to the discovery of a completely different, topological, type of "order", which cannot be described with the previous formalism. It has been shown in fact that the presence of conductive edge states in the quantum Hall state is connected to the non-trivial topology of the electronic band structure. In recent years, a new class of materials has been predicted and observed, where the conduction is limited at the edges even in absence of an applied magnetic field, due to the presence of a strong *spin-orbit coupling.* These materials have been called *topological insulators* since they are insulators in the interior and have exotic metallic states present at their surfaces.
The experimental study of two-dimensional topological insulators, so far, has been mainly focused on quantum wells systems of $(Hg,Cd)Te$ and $InAs/GaSb$, but, recently, theoretical calculations predicted the existence of natural monolayer materials that are topological non trivial. It is the case of WTe_2, a *transition metal dichalcogenide* which, due to a layered structure with van der Waals interactions between planes, can be exfoliated down to atomic thickness. At this reduced dimensions materials show properties quite different from the bulk due to the quantum confinement, and they are a powerful platform to investigate intriguing physical phenomena.
Research on *two-dimensional materials*, which took off with the discovery of *graphene*, has been so far very fruitful and is still quite promising. Recently, in fact, the possibility to stack different layers together in *van der Waals heterostructures*, besides allowing to combine the characteristics of various compounds, opened a new route to explore interesting physical phenomena.

In this thesis we aim at studying the intrinsic properties of WTe_2 in the few layers form,

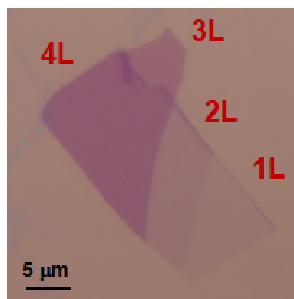

Figure 1.1: Graphene multi-layers flake on Si/SiO_2 substrate; it is possible to distinguish the different thickness looking at the optical contrast.

through the analysis of transport measurements in suitable nano-fabricated devices.
Before addressing in detail more technical aspects, in the following pages we give a brief overview of the state-of-the-art of research on 2D materials as well as on topological insulators; an introduction on these underlying topics is useful to talk properly of our experimental work on WTe_2.

1.1 2D Materials

Two-dimensional (2D) materials consist essentially of a limited number of crystalline layers of atomic thickness, characterized by electronic properties substantially different from those of their bulk parents compounds.
Research on 2D materials took off with the discovery of graphene, a sheet of carbon atoms arranged in a honeycomb lattice. Despite it was studied since the 1940s as a building block of graphite [1], when in 2004 Andre Geim and Konstantin Novoselov succeeded in the isolation of graphene using scotch tape [2], it was a great surprise for the scientific community as statistical mechanics calculations predicted the thermodynamically instability of a 2D crystal [3]. It is possible to explain this experimental result considering that, as these materials are "extracted" from 3D crystals, they are like quenched in a metastable phase; moreover, their strong inter-atomic bonds prevent thermal fluctuations to generate crystal defects even at high temperature [4] [5]. A picture of how a graphene multi-layer flake exfoliated on a Si/SiO_2 substrate looks like is shown in *figure 1.1*.
When exactly a thin crystal should be considered a 2D material is more a matter of definition: depending on the material, qualitative changes in the properties respect to the bulk can occur at various thickness. It also happens that a different number of layers of the same material gives rise to distinct 2D systems; in this sense each thickness can be considered as a new material. In graphene, for instance, the bilayer form shows a different energy dispersion from the monolayer while, considering the trilayer, it has been demonstrated that also the way in which the layers are stacked (ABA or ABC) matters in term of the physical phenomena observed. This suggest that new surprises could emerge from the study of "thick 2D materials", but in practice a limit is set by the high device quality requested experimentally [6].

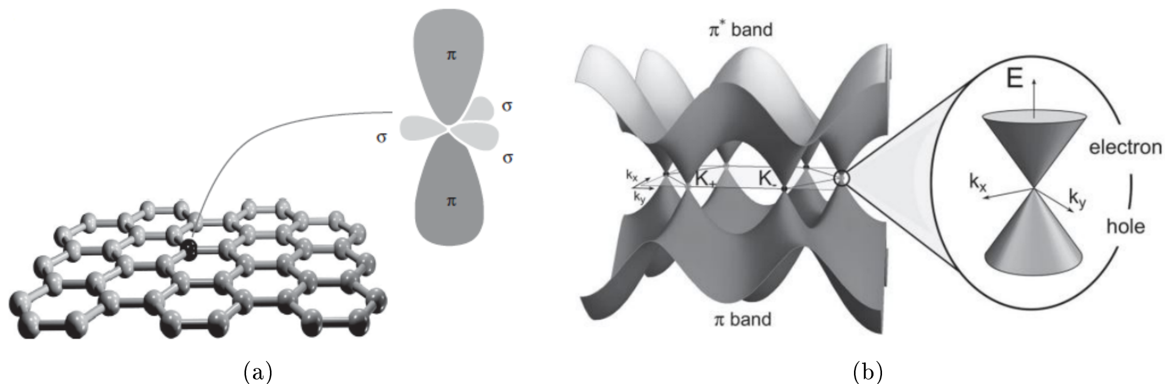

(a) (b)

Figure 1.2: (a) Graphene honeycomb lattice with a zoom-in on carbon atoms orbitals. (b) Band structure of graphene with a Dirac Cone magnified.

In recent years **graphene** has been subject of research in a variety of scientific domains because of its promising properties in many different fields, ranging from material science to electronics, and for the fascinating physical phenomena that shows.
The hexagonal lattice of graphene is formed by in-plane covalent σ bonds between the hybrid sp^2 orbitals of carbon atoms; besides, $2p_z$ electrons, with π orbitals out-of-plane, are weakly bonded and are responsible of the conduction *(fig. 1.2 a)*. The strong interatomic bonds prevent the presence of structural defects ensuring an almost perfect crystal quality; moreover, since also extrinsic disorder is small, charge carriers can exhibit very large mean free paths ($\sim \mu m$) and room temperature mobilities higher than 100 000 $\mathrm{cm^2/Vs}$ [7]. In addition to this, graphene is a zero-gap semiconductor, which enables electrons and holes transport, without the need of chemical doping, and gives the possibility to tune electrostatically the polarity of the carriers, through the application of a voltage to a suitably designed gate electrode [2]. These attractive properties make graphene a good candidate for electronic devices.
Looking a bit closer at the band structure of graphene, we can see that the conduction and the valence bands touch at specific points in the Brillouin zone, known as the *Dirac points* [8] (*fig. 1.2 b*). In a low energy approximation the electronic bands assume a conical shape, forming the so called *Dirac cones*, and the electrons turn out to be effectively described by the Dirac equation for massless relativistic particles, rather than the expected Schrödinger equation. This particular property can be understood considering electrons interacting with the periodic potential as new massless quasi-particles, called *Dirac Fermions*, which propagate at the Fermi velocity instead of the speed of light, like real relativistic particles [2]. Since in this low-energy regime the Fermi velocity is constant, independent of energy, the electron dynamics is described by a linear dispersion relation.

The discovery of graphene has raised broad interest on other 2D materials, and many different systems are currently being studied. In the "family" of 2D materials an important role is played by **transition metal dichalcogenides** (TMDs), characterized by the general chemical formula MX_2, where M is a transition metal (Mo, W, etc.) and X a chalcogen atom (S, Se or Te). They can be viewed as a stack of three-atom-thick layers with the transition metal plane

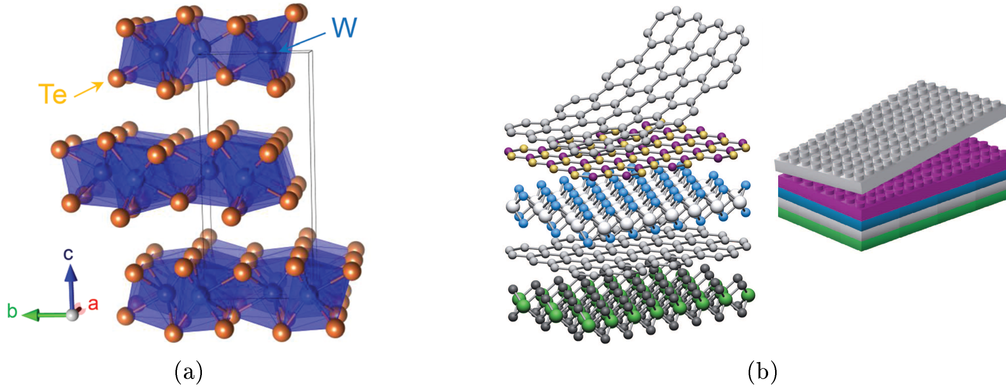

(a)

(b)

Figure 1.3: (a) Schematic representation of the layered structure of WTe_2. (b) An example of van der Waals heterostructure.

“sandwiched” between two chalcogen planes. Individual layers are held together by weak van der Waals forces (*fig. 1.3 a*). Due to this layered structure, these materials, like graphite, can be easily mechanically exfoliated down to atomically thickness.
In the monolayer form, several TMDs, such as MoS_2 and WSe_2, are direct band gap semiconductors which makes them potentially interesting for applications in electronics and optoelectronics [9]. Looking for example at transport properties, the presence of a band gap and an electron mobility comparable to that of silicon makes them more suitable to fabricate transistors than graphene, where the zero gap prevents switching off the conduction.
Another important feature of TMDs is that electrons have a strong spin-orbit interaction (SOI), a consequence of the heavy transition metal atoms they belong to. The coupling of the electron spin with its orbital motion introduces an energy splitting between spin-up and down states in both valence and conduction bands; the control of carriers confined in one of these valleys, between the two bands maxima-minima, opens up a new field of physics called *valleytronics* [10]. However, the most important implication for our work is that this strong spin-orbit interaction can induce topological insulating states in certain TMD compounds.

Nowadays it is also possible to combine the characteristics of different 2D materials, stacking several layers one on each others in so-called, **van der Waals heterostructures** (vdW), a name that underlines the weak inter-layer interaction (*fig. 1.3 b*).
VdW heterostructures were first assembled while searching for an ideal substrates for graphene devices. Experimental work in fact highlighted that the properties of graphene on SiO_2 were far from the one expected in the intrinsic material, due to an increase of disorder [11]. The research on 2D materials suggested that a thin layer of *hexagonal boron nitride* (hBN), atomically flat and chemically inert, could be a great alternative to SiO_2. This intuition was correct and the first heterostructures of graphene placed on hBN confirmed an improvement in the material properties [12].
These promising results led to try new combinations of 2D materials with the aim of exploiting the interfacial interactions to enhance physical properties of interest. For instance, recent research has shown that the strong spin-orbit coupling in WS_2 can induce an increase by a factor

of 100-1000 in the SOI of a graphene flake placed on top of it [13]. More in general, thanks to their versatility, in the last years, TMDs and graphene have been at the centre of attention as building blocks of various heterostructures, which could show new physical phenomena or interesting properties for potential applications [14] [15].
Recently, the possibility to "encapsulate" air-sensitive compounds between top-bottom protective layers has opened a route to study novel 2D materials. This is, for example, the case of *phosphorene* and WTe_2, whose encapsulation in hBN prevents the degradation and gives the access to new physics [16] [17].

1.2 Topological Insulators

Topological insulators (TIs) are a recently discovered class of materials which behave as insulators in their interior but whose surface contains conducting states, called *helical states*, protected by time reversal symmetry. The occurrence of helical states is intrinsically related to the non-trivial topology of the bulk bands, that in TIs is induced by the presence of a strong spin-orbit interaction. The electronic band structure of a TI is analogous to the one of an ordinary insulator in the bulk, with the Fermi level in the gap between valence and conduction band (*fig. 1.4 a*). The gap is though closed by spin polarized states localized at the surface, which are protected against backscattering and for this reason characterized by a quantized conductance. Due to the spin-momentum locking, in fact, the "U-turn" scattering is strongly suppressed since at a given energy the only available electronic states have different spin [19].
Topological insulators can be either two or tree dimensional. We will focus mainly on the 2D case without addressing in details three dimensional TIs, since their discussion goes beyond the purposes of the present work. In 2D TIs the SOI plays the role of the magnetic field in the Quantum Hall Effect (QHE), acting as a spin dependent force on the electrons which are moving through the crystal [21]. This can lead to the *Quantum Spin Hall Effect* (QSHE) that can be seen as a two-copy version of the QHE: if in the QHE there is only one *chiral* state per edge, in the QSHE there are two different conduction channels with opposite spin directions counter-propagating along every edge (*fig. 1.4 b-c*). For that reason the expected quantized conductance is $2e^2/h$, twice the quantum of conductance [22] [23].

We can see a link between physics and topology trough the concept of "smooth deformation". In mathematics, a deformation of shape that does not create any holes groups different geometrical entities into equivalence classes, which are characterized by the same topological index. According to this principle, objects can be classified by the number of holes in them: a perfect sphere is then equivalent to an ellipsoid and similarly a coffee cup to a donut, as we can see in *figure 1.5 (a)*. In physics, if we consider a many-particles system, we can define a smooth deformation as a change in the general Hamiltonian which does not close the energy gap separating the ground state from the excited states. Thus, one gapped state cannot be deformed to another gapped state in a different topological class, unless a quantum phase transition occurs where the system becomes gapless. For that reason, the interface between a non-trivial topological state and the vacuum, which is trivial, has to be metallic. The topological indexes are indeed different for the two phases and, since they are topological invariants, they cannot change as long as the material remains insulating [20]. An intuitive illustration that shows the

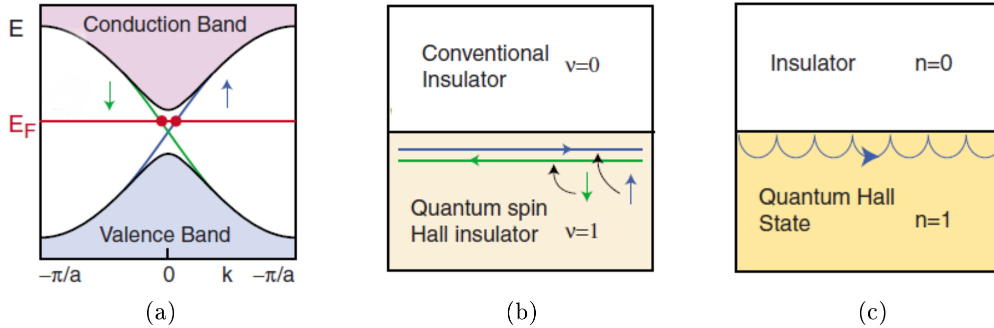

Figure 1.4: (a)Schematic representation of the band structure of a topological insulator. Interface between a conventional insulator and a quantum spin Hall insulator (b) or a quantum Hall state (c) with respectively chiral and helical edge states. [24].

connection with topology is given in *figure 1.5 (b)*.

The prediction of 2D topological insulators was theorized by Kane and Mele in 2005, who proposed that spin-orbit interaction in graphene could induce a state with a non-trivial topology [25]. However, because of the too small intrinsic spin-orbit coupling in carbon atoms, the QSHE has never been found in this material. A quantized charge conductance along the edges with no magnetic field was instead observed in (Hg,Cd)Te quantum wells in 2007 [26] [27] and a similar phenomenon was later discovered also in InAs/GaSb heterostructures in 2011 [28]. Debates are still on going to understand why the apparent quantization of the conductance in these systems is not at all precise.
In 2008 the analogous spin-orbit induced topological state in 3D systems was observed in the alloy $Bi_{1-x}Sb_x$, within a certain range of compositions x, by angle-resolved photoemission spectroscopy (ARPES) [29]. Simpler versions of 3D TIs were then discovered in Bi_2Se_3, Bi_2Te_3 and Sb_2Te_3, compounds with larger bulk gaps and helical states consisting of a single Dirac cone [30]. The surface states of the next-generation topological insulators are closely related to the Dirac electronic structure of graphene, i. e. they are characterized by a linear energy–momentum relationship. The main difference between the two is that topological insulators have only one Dirac point instead of two and no spin degeneracy. Moreover, while in graphene the density of carriers is highly tunable with an applied electrical field, the Fermi level of a topological insulator does not sit at the Dirac point, making the tuning of density more tricky. However, through a combination of surface and bulk chemical modification, tuning to the Dirac point in Bi_2Se_3 was recently demonstrated [31].

Besides their fundamental interest, topological insulators are predicted to have special properties that could be useful for applications, ranging from spintronics to quantum computation. For instance, since a charge current along the surface automatically yields a non-zero spin density, a heterostructure that combines a topological insulator with a ferromagnet could allow the latter to be switched by passing a current through the TI's surface. This could lead to the develop of a new type of spin torque device for magnetic memories [32].
However, the most intriguing feature is that helical states can host *zero-energy Majorana*

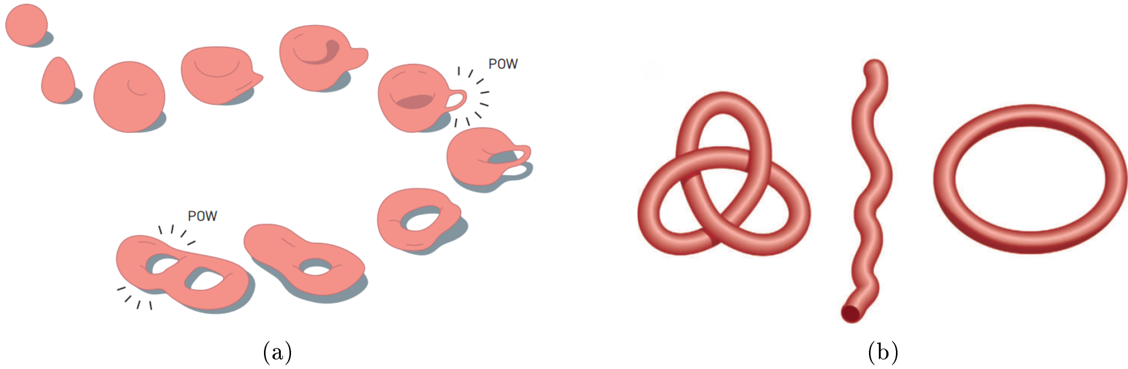

Figure 1.5: (a) Topological classification of geometrical objects according to the number of "holes" in them. (b) The trefoil knot represents a topological insulator and the closed loop an ordinary one. Since there is no continuous deformation by which one can be converted into the other, there must be a surface where the string is cut, shown as a string with open ends, to pass between the two knots. In a topological insulator, the component that is 'knotted' is the electron's wavefunction as it moves through momentum space and we can say that metallic states are born when a surface unties 'knotted' electron wavefunctions [21].

fermions if superconductivity is induced on the surface of 3D topological insulators via *proximity effects* [33]. The Majorana particle is a fermion which is its own antiparticle and then it has to be electrically neutral. In condensed matter physics, it can exist as a quasiparticle in superconductors or it can be bound to a defect at zero energy, forming a Majorana zero mode. The Majorana bound states are no longer fermionic and they are governed by non-abelian statistics, i.e. interchanging them changes the state of the system in a way that depends on the order in which the exchange was performed. For that reason, it is claimed that they could be used as building blocks for a topological quantum computer, which would be less susceptible to local decoherence processes and exceptionally well protected from errors [34].

1.3 QSHE in WTe_2 monolayer

Recently, theoretical calculations have predicted that strained WTe_2 monolayer could be a possible platform for two-dimensional topological insulators.
WTe_2 is a transition metal dichalcogenide characterized by a distorted version of the common $1T$ crystalline structure, called $1T'$ phase. This spontaneous lattice distortion induces an intrinsic band inversion - with the formation of two Dirac cones along the Y-Γ-Y direction in the Brillouin zone - and causes 1T'-WTe_2 to become topologically non trivial. The strong spin-orbit coupling then lifts the degeneracies at the Dirac points and opens a bulk bandgap leading to a Quantum Spin Hall insulator through a similar mechanism as the Kane-Mele model for graphene. Different calculation methods give various estimates on the size of the bandgap for strain-free 1T'-WTe_2 monolayers; however, even when it is predicted to be a semimetal, the negative fundamental gap can be easily lifted by a tensile strain as small as 1% [37].
Realization of a QSH insulator in natural 2D TMDs would be a breakthrough since these materials are widely available, they can be easily exfoliated and combined together in van der Waals

heterostructures, allowing great advantages for future applications and fundamental studies. Due to the small bandgaps exhibited by many candidate systems, so far the experimental study on QSHE has been limited to quantum wells heterostructures of three-dimensional (3D) semiconductor, designed to achieve an inverted bandgap. Even if edge conduction consistent with a QSH state has been observed, these systems still present several puzzles. First of all, the conductance is not perfectly quantized, it decreases in long edges and shows mesoscopic oscillations as a function of gate voltage, observations not in accordance with the predicted absence of elastic backscattering. Secondly the edges show signs of conductions even at high magnetic fields, contrary to the expectations for helical states when time-reversal symmetry is broken [18]. Finally, it has to be considered that a non-helical edge conduction could also be present, due for instance to band bending when a gate voltage is applied [17]. For these reasons the study of a natural monolayer 2D topological insulator would be helpful to clarify and explain all the still open questions.
Recent experimental works has achieved promising results in this direction, identifying the hallmarks of QSHE in WTe_2 by means of transport measurements, angle resolved photo emission spectroscopy and scanning tunnel microscopy (STM).
Edge conduction has been observed in monolayers WTe_2, encapsulated in hBN protective layers, at temperatures below about 100 K. The hypothesis of helical edge states seems consistent with the experimental evidence: the edge conduction is in fact suppressed by a magnetic field and is independent of gate voltage, except for mesoscopic fluctuations that increase on cooling. However, the measured edge conductance is about half the predicted value e^2/h [17].
Besides, a bulk gap between 45 and 55 meV has been observed with ARPES in epitaxially grown monolayer WTe_2 (*fig. 1.6 (a-b)*). The measured bandgap, confirmed by STM measurements, is an order of magnitude higher than gaps seen in quantum wells, fact that underlines the potentialities of monolayers TMDs as a large bandgap class of 2D TIs. Finally, STM spectra clearly show a modified electronic structure near the edge, consistent with the expectations for a QSH insulator (*fig. 1.6 c*) [36].

1.4 Motivation and outline

Motivated by this intriguing prediction and the promising results, we have realized suitable nano-devices to study the conduction properties of monolayer WTe_2.
Bulk WTe_2 has already attracted the attention in the past for its large, non saturating magnetoresistance. This peculiar feature could be explained considering the nature of the material, which is the first example of a nearly perfect compensated semimetal, i. e. the density of electrons and holes is about the same [35]. Recent experimental work has also highlighted the tunability of WTe_2 electronic properties with thickness: thinning the material down, the high mobility of the bulk gradually reduces and a metal-insulator transition appears below four layers thickness. Quantum effects observed in magnetotransport measurements, together with the absence of a gate dependence, strongly suggests that the insulating state is due to a disorder-induced localization of charge carriers, rather than to a change in band structure. The non perfect stability of the material in air leads in fact to an oxidation of the outermost layers, which starts to play an important role when the material is thinned down [38].

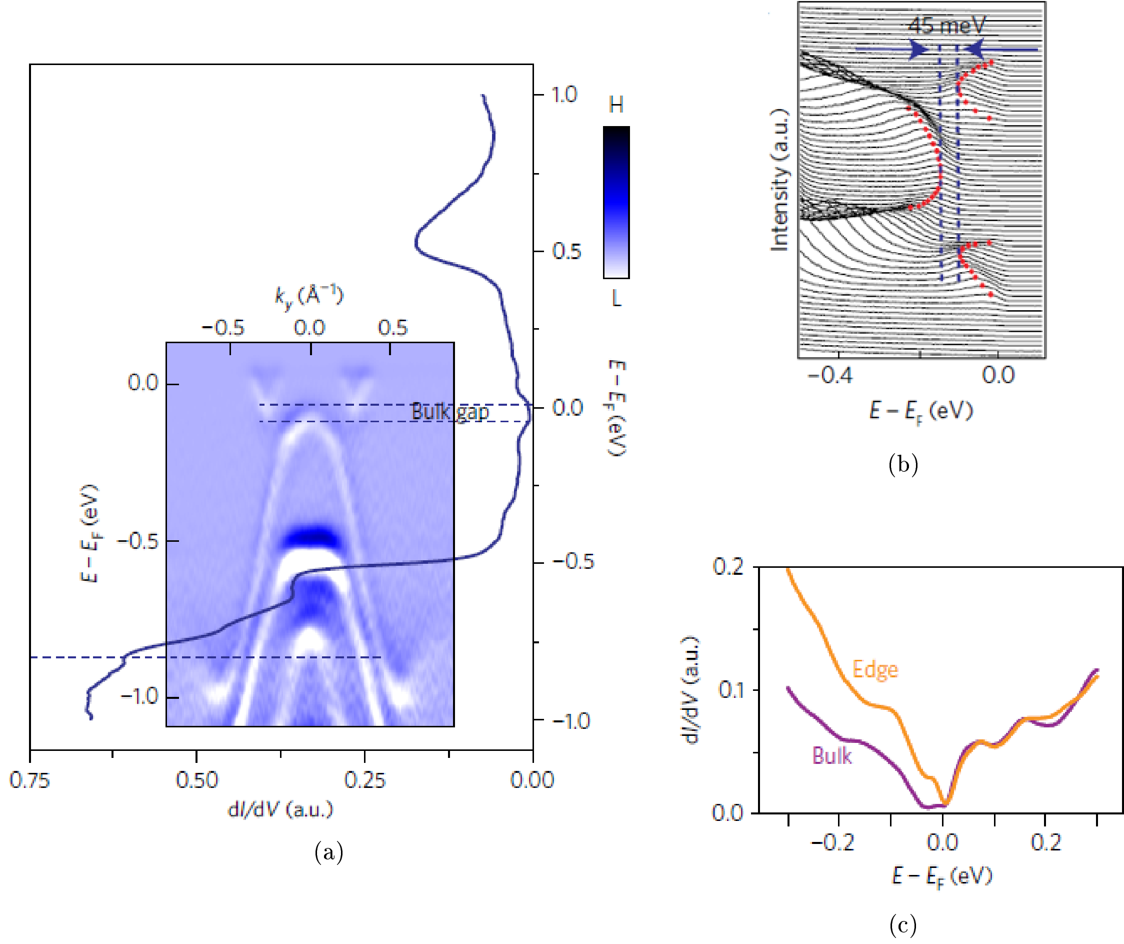

Figure 1.6: (a) Bulk STM dI/dV spectrum and high-symmetry ARPES cut along the Γ–Y direction. (b) Energy distribution curves (EDC) extracted by an ARPES spectrum; the size of the bandgap is estimated to be 45 meV. (c) STM dI/dV representative spectra taken at the edge and in the bulk of monolayer WTe_2 [36].

Since our goal is to study the intrinsic properties of few layers material, it is necessary to prevent the degradation, working in inert conditions. A possible solution is exfoliation under a protective atmosphere inside a *glovesbox* and an encapsulation of the monolayer between top-bottom layers of an inert material, like hBN. Previous experimental works have indeed already shown the capability of this structure to preserve the material quality [39] [40].
We then realized van der Waals heterostructures with an encapsulated monolayer WTe_2 with the aim of investigating the properties of this material and of trying to reach a deeper comprehension of the underlying physical phenomena. Our results confirm the presence, at low temperatures, of a bulk gap in monolayer WTe_2 and of an edge conduction with a conductance per edge of the order of e^2/h, consistently with previous experimental work. Moreover, new geometries and configurations have been explored in order to simplify the fabrication process

and to improve the imperfect transmission between the metal contacts and the crystal, which is most likely one of the main motivations for the reduced values of the measured conductances compared to the theoretical predictions.

After having introduced general concepts and the motivations for our studies, we define the outline of this thesis, which has the following structure.
Chapter 2 is a theoretical background of the main physical concepts useful for a better comprehension of our work. Starting with a general introduction on mesoscopic systems, whose main properties can be studied by means of gate modulated transport in nano-devices (*section 2.1-2.2*), in *section 2.3* we will treat the Landauer-Büttiker formalism, a very powerful approach to theoretically predict resistance values in multi-terminal configurations. In *section 2.4* we will describe some quantum interference phenomena which are often present in low dimensional structures, e.g. weak anti-localization, while in *section 2.5*, after a brief discussion on classical magnetotransport, the Quantum Hall Effect (QHE) will be addressed. With reference to the topological nature of the QHE, we will then introduce the concept of spin-orbit topological insulators, focusing manly on the Quantum Spin Hall Effect (QSHE), treated in *section 2.6*, with a particular attention to the transport properties of helical edge states.
Chapter 3 describes the main characteristics of WTe_2, starting from the bulk (*section 3.1*) which is analysed with a classical two bands model, and scaling down to thin layers. The evolution of magnetotransport with thickness is analysed in *section 3.2*, in reference to the problem of degradation due to air-sensitivity. We will then propose the solution of encapsulation in van der Waals heterostructures and in *section 3.3* we will discuss the conduction properties of monolayer WTe_2, with a special emphasis on the observation of edge current.
Chapter 4 describes the technical aspects of the device fabrication, which involves standard nano-fabrication techniques (*section 4.1*), and non-conventional methods. In this respect, a key step to assemble WTe_2 monolayers devices is developing a transfer technique, addressed in *section 4.2*, which allows to pick-up atomically thin crystals and to align different layers with micrometric precision. The heterostructures assembled in this way are described in *section 4.3*; in particular we will show two different alternative configurations.
Lastly in *Chapter 5*, after a brief description of the measurement set-up (*section 5.1*), we will analyse the data obtained by means of low temperature magnetotransport measurements. In *section 5.2* we will present a characterization of a bulk sample, based on previous research work and carried out to test the quality of the crystals. Finally, in *section 5.3-5.4* data related to a WTe_2 monolayer device are discussed and compared to the current experimental results of other research groups.

Chapter 2

Electronic transport in mesoscopic systems

Mesoscopic physic, from “meso” which means “intermediate”, deals with systems whose dimensions are much bigger than single atoms but smaller than macroscopic objects and far from the so-called *thermodynamic limit*. In this regime statistical fluctuations start to play an important role and a quantum mechanical treatment is necessary to describe the observed properties. In fact, beyond a certain length and energy scale the wave nature of electrons has to be taken in consideration and interesting new phenomena appear.
We will start this chapter with a description of the nano-devices we use to study transport in thin layers materials, whose operating principle is analogous to that of field effect transistors. Since in our devices we often deal with transport properties typical of mesoscopic physic, we will give a definition of the length scales that characterizes this regime of conduction. Next, after having introduced the Landauer-Büttiker formalism which is particularly useful in the description of mesoscopic conductors, we will treat some typical quantum interference effects, like the weak anti-localization and the universal conductance fluctuations. We will then address magnetotransport, starting from its classical treatment and ending up with the description of the quantum Hall effect in a 2DEG. Lastly, we will focus on the quantum spin Hall effect with the main goal of analysing the transport properties of helical edge states, which are very important for our work since they are expected to be observed in monolayer WTe_2.

2.1 Gate modulated transport in nano-devices

Many of the electronic properties of a mesoscopic system can be explored by means of low-temperature transport experiments across transistor devices, similar to the one sketched in *figure 2.1*. Metal contacts deposited on the material of interest allow to inject carriers and read voltages (or vice-versa to apply tensions and measure currents), while the Si/SiO_2 substrate can be used as a gate to tune the electronic density. In particular a *Hall bar geometry*, with two main contacts as source-drain and smaller lateral probes, is privileged for magnetotransport in order to measure independently the longitudinal R_{xx} and the transverse R_{xy} resistances.
Applying a voltage to the back gate V_G, the induced transversal electric field shifts the Fermi

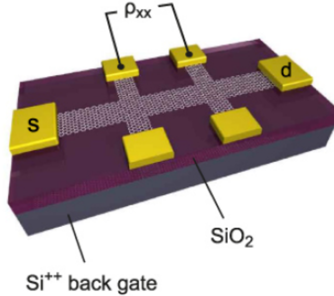

Figure 2.1: Scheme of a typical device for transport measurements.

level of the sample and if we deal, for instance, with a semiconductor, we can see ambipolar transport. The concentration of charge carriers n can be estimated from a parallel plate capacitor model, where

$$n = \frac{C_G V_G}{e} \qquad\qquad C_G = \frac{\epsilon_r}{d_{ox}} \tag{2.1}$$

where C_G is the gate capacitance per unit area, ϵ_r the relative permittivity ($\epsilon_r = 3.9\ \epsilon_0$ for SiO_2), d_{ox} the oxide thickness and e the electron charge. In particular for 300 nm SiO_2 and an applied gate voltage of 100 V we can induce a surface charge density of about $10^{17}\ m^{-2}{\cdot}V$ in our crystalline *flake*. This charge tuning is effective in case of materials with an electron concentration of the same order of magnitude, like for instance WTe_2. However, to induce a higher density is possible to use thin layers of insulating materials, like boron nitride, placed on top (or bottom) of the device, or for even higher concentration an alternative is given by the *ionic-liquid* gating [44].
In case of a semiconductor material, if we apply a bias between the drain and the source V_{DS}, the current I_{DS} is the one expected in a *field effect transistor* (FET) in the linear regime [45]

$$I_{DS} = \mu C_G \frac{W}{L}(V_G - V_T)V_{DS} \tag{2.2}$$

where V_T is the threshold voltage to accumulate charge, μ the mobility of charge carriers in the semiconductor, W and L the width and the length of the sample, respectively. We notice that, analysing the gate dependence of the conductance obtained in transport measurements, we can easily obtain the mobility:

$$\mu = \frac{L}{W}\frac{1}{C_G}\frac{1}{V_{DS}}\frac{\partial I_{DS}}{\partial V_{GS}}. \tag{2.3}$$

However, for ambipolar transport to take place, the device has to be equipped with electrodes capable of injecting both holes and electrons. This is not trivial to a achieve, as the energy level alignment between the metal contacts and the semiconductor usually favours the injection of one type of charge carriers. When a semiconductor is placed in close contact with a metal, indeed, the equilibration of the electrochemical potential between the two materials leads to charge transfer across the interface which, according to the energy alignment, results in either depletion or accumulation of carriers. [46]. The effect can be easily visualized in terms of

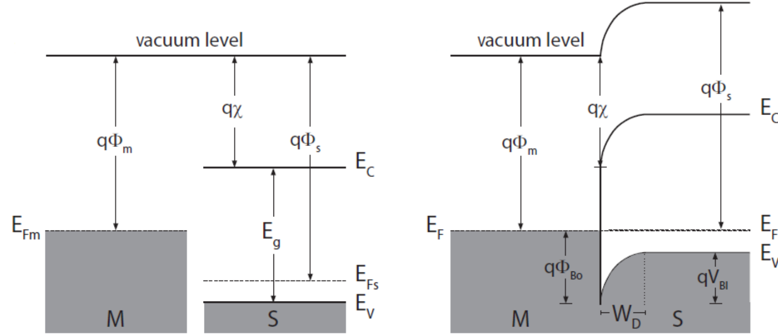

Figure 2.2: Energy band-diagrams at the interface between a metal and a p-type semiconductor, before contact (left) and in thermal equilibrium (right). W_D is the *depletion region* and V_{BI} the *built-in potential*.

energy band diagrams, as depicted in *figure 2.1 (b)* in the case of a *p-type* semiconductor. At the metal-semiconductor junction the Fermi levels align each others and, if the *work function* of the metal Φ_m is bigger than that of the semiconductor Φ_S, the bands of the p semiconductor bend downward. The *band-bending* is responsible for the creation of a potential barrier for holes across the interface, called *Schottky barrier*. In the *Schottky-Mott limit* the height of the barrier Φ_{Bo} is given by:

$$\Phi_{Bo} = \frac{E_g}{q} - (\Phi_m - \chi) \tag{2.4}$$

with E_g energy bandgap of the semiconductor, χ its *electron affinity* and q the elementary charge. The presence of the Schottky barrier has a deep impact on the flow of current across the junction: the injection of carriers is allowed only for one polarity of the applied bias, resulting in asymmetric characteristics and in a rectifying behaviour. Since in our device we need ohmic contacts, for a given semiconductor, the metal used for the electrode has to be chosen in order to minimize the Schottky barrier.

2.2 Characteristic lengths

To describe electronic transport in mesoscopic systems at low temperatures, three characteristic quantities are specially important: the *mean free path* l_m, the *Fermi wavelength* λ_F and the *phase coherence length* L_ϕ.
The mean free path, which is the average length travelled by one electron before undergoing scattering processes, determines the regime of conduction. Its value strongly depends both on material and temperature, but roughly for metals at room temperature can be estimated around 100 Å, so some tens of interatomic distances. Thus, generally, electrons scatter many times during their propagation in a crystal and the motion is *diffusive*. However, at low temperature and in very ordered systems, as in GaAs, l_m can be of the order of 10-100 microns, then even longer than the length of a nano-fabricated structure. In this case electrons propagate without being scattered and the conduction is called *ballistic*.

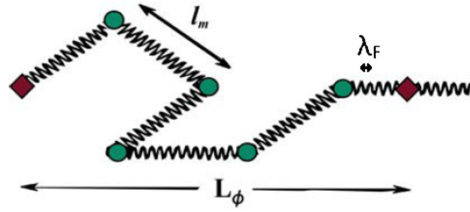

Figure 2.3: Illustration of an electron path in a conductor where $\lambda_F << l_m << L_\phi$: wiggled lines represent electron wave motion, green circles elastic collisions, which randomize the momenta, and red squares inelastic collisions, that affect the phase.

Estimating the value of the electron Fermi wavelength, we can understand whether the *semiclassical approximation* is suitable or not to describe transport in conductors of a certain dimension. In this model an electron in a state k is treated like a classical particle with a velocity v_k, given by the group velocity of the associated wave-packet centred on the k state. Since electrons are seen like "balls", with a position and a wave-vector simultaneously defined, according to the *Heisenberg principle*, they cannot be localized on distances less than their wavelength. It is then straightforward that, if the dimensions of the system are smaller of comparable to the Fermi wavelength, to describe the electron motion we have to go beyond the semi-classical approximation. From the wave-particle duality we have $\lambda = 2\pi/k$, which is connected to the carriers density since $k = \sqrt[3]{3\pi^2 n}$. While in the bulk of a metal an electron concentration of 10^{28} m^{-3} leads to a Fermi wavelength of the order of atomic dimensions, in a typical *two-dimensional electron gas* (2DEG) λ_F can reach the dozens of nanometers, so comparable to the characteristic lengths of a nano-structure.
Considering the wave nature of electrons, the other relevant quantity is the phase coherence length, that is the distance up to what particles propagate without loosing phase information. If L_ϕ is sufficiently long, interference phenomena typical of waves can be experimentally observed. This happens at sufficient low temperature ($\sim 1K$), when the probability of inelastic scattering events (electron-photon collisions or e-e interactions), that affect the waves frequency, considerately decreases [41].
An illustration of these three characteristic lengths is given in *figure 2.3*, relative to the case of a metal [42]. The conduction can be described in a classical way if the dimensions of the structure are much larger than each of these quantities; since for mesoscopic systems this condition is not fulfilled a quantum-mechanical treatment becomes necessary. As briefly mentioned, these length scales are strongly affected by the temperature and vary widely depending on the material. This is the reason why mesoscopic transport phenomena are observed in conductors of different dimensions, ranging from a few nanometers to hundred microns [43].

2.3 Landauer-Büttiker formalism

The Landauer-Büttiker formalism describes the conductance in terms of the probability that an electron is transmitted through a conductor. This approach is conceptually quite different from

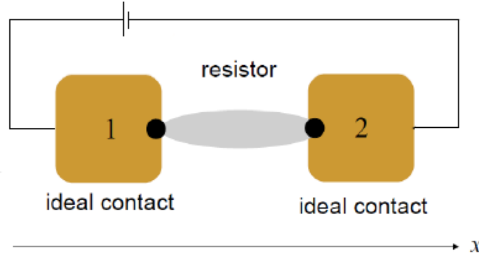

Figure 2.4: Schematic representation of a conductor connected with two bulk contacts at different chemical potential.

the classical way to think about the conduction, in which the conductivity is defined as a local property that connects the electric field and the current density in every point of the material. The transmission probability is, in fact, a global quantity that characterizes the whole structure and reflects the "ease" with which the electron can propagate in it.
In this section we will see an application of this powerful approach, calculating the conductance of a mesoscopic sample and deriving the well known *Landauer formula*. Then we will treat briefly the finite temperature case and finally we will describe how the two terminal conductance generalizes to a multi-terminal configuration, introducing the *Büttiker formula*.

2.3.1 Landauer formula

Let's consider a mesoscopic conductor connected to two large contacts, as the one shown in *figure 2.4*. The fact the contacts are wider compare to the conductor ensure we can treat them as "reservoirs" in quasi-equilibrium at chemical potential μ_1 and μ_2, i.e. they are not perturbed by the current flowing in the device. The occupation probability of the electrons in the contacts is then the *Fermi-Dirac distribution* $f(\epsilon_k)$, with a chemical potential determined by the applied bias. The current injected by the first reservoir, in the most general case, can be written as

$$I_1 = 2\frac{e}{2\pi}\int_0^{\infty} dk v_k f_1(\epsilon_k)T(\epsilon_k)M(\epsilon_k) \tag{2.5}$$

where the factor 2 takes into account the spin degeneracy, $\frac{1}{2\pi}dk$ is the density of states in a range dk, while v_k and $T(\epsilon_k)$ are respectively the electron velocity and the transmission probability for a state k. In the integral appears also the function $M(\epsilon_k)$, which tells us the number of *transverse modes* at energy ϵ. In a narrow conductors, in fact, the electron energy is quantized and each occupied sub-band constitutes an independent conducting channel that contributes to the total current [43].
Recalling that $v_k = \frac{1}{\hbar}\frac{dE}{dk}$, with $\hbar$ reduced Plank constant, we can rewrite the current in a simpler form

$$I_1 = \frac{2e}{h}\int_0^{\infty} d\epsilon f_1(\epsilon)T(\epsilon)M(\epsilon). \tag{2.6}$$

Besides I_1, which describes the electrons moving from left to right, there is an analogous term I_2 for the electrons injected by reservoir 2 and moving in the opposite direction.

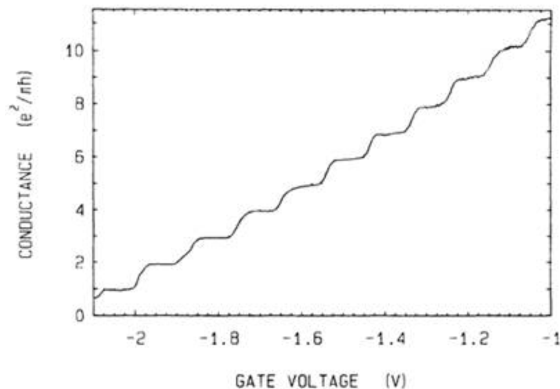

Figure 2.5: Conductance of a QPC as a function of the spit gates voltage; more negative potential increases the depletion of electrons [48].

Assuming the hypothesis of "reflectionless" contacts, i.e. electrons can enter them from the conductors without any reflections [43], the net current through the sample can be written simply as the difference of these two currents I_1 and I_2. If we consider to be at zero temperature, where $f_{1,2}(\epsilon) = 1$ if $E < \mu_{1,2}$ or 0 otherwise, we have

$$I = I_1 - I_2 = \frac{2e}{h}\left(\int_0^{\mu_1} d\epsilon T(\epsilon)M(\epsilon) - \int_0^{\mu_2} d\epsilon T(\epsilon)M(\epsilon)\right) = \frac{2e}{h}TM(\mu_1 - \mu_2) \quad (2.7)$$

which has been further simplified considering a small applied voltage on the scale of $k_B T$, so that we can neglect the energy dependence of the transmission probability and of the number of modes. The obtained total current corresponds to a conductance

$$G = \frac{2e^2}{h}MT \quad (2.8)$$

a very important expression, known as *Landauer formula*. While for a large conductor we have $G = \sigma W/L$, here the conductance is independent of the length L of the sample and does not decrease linearly with the width W. Instead it is proportional to the electron's transmission probability and it depends on the number of conducting channels, varying in discrete steps when the width is changed. In fact it can be shown that

$$M = Int\left[\frac{W}{\lambda_F/2}\right] \quad (2.9)$$

where $Int(x)$ represents the integer just smaller than x [43].
Particularly interesting is the case of a one dimensional ballistic conductor, where there is only one transverse mode ($M = 1$) and the transmission is perfect ($T = 1$). The conductance then turns out to be just a combination of fundamental constants

$$G = \frac{2e^2}{h} \quad (2.10)$$

and it corresponds to a quantized resistance $R_C \approx 13$ KΩ. Since in a ballistic conductor electrons propagate without scattering, the fact there is a non-zero resistance can be explained only taking in consideration the thermalization processes at the interface between the conductor and the reservoirs. For that reason R_C is called *contact resistance* and in the more general case of a mesoscopic conductor it is inversely proportional to the number of transverse modes. It is then clear that when we deal with wide conductors, having thousands of modes, R_c is small and tend to be unnoticed.
The quantized nature of conductance in a ballistic conductor was observed independently by two groups, led by B. J. van Wees and D. Wharam, in 1988, varying the gate voltage in a *quantum point contact* (QPC). A QPC is a short constriction whose width is comparable to the Fermi wavelength of the electrons and is normally realized using a *split gates* geometry. As we can see in *figure 2.5*, when the potential in the QPC region increases and the width of the constriction is reduced, the modes are "lifted" one by one above the Fermi energy, leading to a decrease of the conductance in steps of $2e^2/h$.

2.3.2 Finite temperature case

Generalizing the obtained result at the case of finite temperature is straightforward and it is interesting for the comprehension of real situations. The current can be written as

$$I = \frac{2e}{h}\int_0^\infty d\epsilon[f(\epsilon-\mu_1) - f(\epsilon-\mu_2)]T(\epsilon)M(\epsilon) \simeq \frac{2e}{h}\int_0^\infty d\epsilon\left(\frac{\partial f}{\partial\epsilon}\right)(\mu_1-\mu_2)T(\epsilon)M(\epsilon) \quad (2.11)$$

which comes back to the (2.3) in case of zero temperature, since $\frac{\partial f}{\partial \epsilon} \simeq \delta(\epsilon_F)$. Hence, at finite temperature, the electrons are broadened in energy on the scale of k_BT and possible variation of $T(E)$ on a smaller scale are "washed out" by the integral. For this reason, in order to see experimentally conductance steps originating form quantization effects, the temperature has to be low enough (<1K) so that k_BT is much smaller than the energy separation between the modes ($\simeq 0.1$ meV in a 2DEG).
This limited energy resolution, due to the thermal broadening of the Fermi distribution, is a common aspect in transport through mesoscopic structures and it has to taken carefully into account in planning experiments.

2.3.3 Multi-terminal generalization

Büttiker extended this approach to systematically treat voltage and current probes in multi-terminal devices. The generalization of the two-terminal Landauer formula (2.3) to multiple probes is given by

$$I_i = \frac{e}{h}\sum_{j\neq i}[T_{ji}\mu_i - T_{ij}\mu_j] \quad (2.12)$$

where the summation is over all the probes apart from the ith one and T_{ij} is the product of the number of modes and the transmission probability from probe j to i.
Considering that in stationary conditions the current is zero and all the probes have equal voltage, we must have

$$\sum_{j\neq i} T_{ji} = \sum_{i\neq j} T_{ij} \quad (2.13)$$

which, together with the relationship $V = -\mu/e$, allows to rewrite the (2.7) in an equivalent form

$$I_i = \frac{e^2}{h} \sum_{j \neq i} T_{ij}[V_i - V_j]. \tag{2.14}$$

This expression is known as *Büttiker formula* and enables to write the multi-terminal conductance in form of a compact matrices without knowing the specific pattern of the device. Since transport in nanostructures is viewed as a scattering problem of electrons that from an initial state in one lead could be scattered into a final state in another lead, calculating the expected current in one probe means considering the transmission coefficients between the involved contacts, each of which is given by the sum over all the probability amplitudes related to the possible paths.
In the simpler case of a three-terminal device the Büttiker formula is

$$\begin{pmatrix} I_1 \\ I_2 \\ I_3 \end{pmatrix} = \frac{e^2}{h} \begin{pmatrix} T_{12} + T_{13} & -T_{12} & -T_{13} \\ -T_{21} & T_{21} + T_{23} & -T_{23} \\ -T_{31} & -T_{32} & T_{31} + T_{32} \end{pmatrix} \begin{pmatrix} V_1 \\ V_2 \\ V_3 \end{pmatrix} \tag{2.15}$$

where the three equations are not independent for the conservation of the current $I_1 + I_2 + I_3 = 0$. Moreover, since the magnitude of the current depends only on voltage differences between the terminals, we can set an arbitrary probe to zero without loss of generality [49].
The Büttiker approach has become a standard technique to determine the conductance in a multi-terminal device. Setting the current sources and measuring the voltages experimentally, by solving the system it is possible to calculate the expected resistance values and compare them with the obtained measurements.
As we will see in the last section of the chapter, for our purposes this approach is particularly useful to study the transport of helical states, which are characterized by non-local conduction.

2.4 Quantum interference effects

As already mentioned before, when the temperature is sufficiently low, electrons maintain their phase coherence for a longer distance and their wave nature starts to play an important role. In particular in low-mobility samples it can happens that the phase-coherent length is much larger than the mean free path ($L_\phi \gg l_m$), leading to quantum interference phenomena.
There are two main classes of coherence effects, observed in systems of different dimensions.
The *sample specific* phenomena depend on the details of the system, such as the precise impurity configuration; belong to this class the *universal conductance fluctuations* (UCF), which appear in samples with dimensions inferior than L_ϕ, varying the magnetic field. The *ensemble averaged* phenomena, instead, as the name suggests, survive upon averaging their contributions on different coherent units and are observable also in bigger samples. This is the case of *weak-localization* and *weak anti-localization*, which manifest macroscopically as quantum corrections in the conductivity.
In the following section we will briefly describe these coherence effects, which can all be traced back to the interference between different possible trajectories of the electrons.
Concerning our work on WTe_2, the correction due to weak anti-localization is particularly useful

in the analysis of the magnetoresistance measurements of thin layers, where the disorder reflects in a strong localization of the carriers.

2.4.1 Weak localization

The weak-localization phenomenon manifests as an increase of resistance at very low magnetic field, observed at low temperature in phase coherent conductors.
We can trace the origin of this correction, analysing the diffusive motion of an electron in its random walk between two points.
In a scattering event, the probability for an electron in a mode m to be reflected in a mode n, considering all the possible Feynmann paths connecting the two states and the respective amplitudes A_k, is given by:

$$R(m \to n) = \left| \sum_k A_k \right|^2 = \sum_k a_k^2 + 2 \sum_{j<k} a_k a_j e^{i(\phi_k - \phi_j)} \\ with\ A_k = a_k e^{i\phi_k}. \tag{2.16}$$

Since usually the paths are uncorrelated, the phase ϕ are random and the crossed terms, related to interference effects, average out. We recover then the classical result given by the sum of probabilities.
However, in presence of *time reversal symmetry* (TRS), the trajectories in which an electron comes back to its initial state give rise to a non-vanishing contribution to the quantum interference term. As we can see intuitively in *figure 2.6*, for every clockwise self-crossing path exists in fact a correspondent anticlockwise loop with the same probability amplitude. Due to the exact compensation of the phases the two closed paths interfere constructively, leading to an enhanced probability for electrons to wander around in a circle, coming back to the starting position.
More formally, if we group all the self-crossing trajectories into two sets, such that every path A_k of the first set has the respective time-reversed parter A_{kR} in the second set, we obtain

$$\begin{aligned} R(m \to m) &= |(A_1 + A_2 + ...) + (A_{1R} + A_{2R}...)|^2 \equiv |A + A_R|^2 = \\ &= \sum_k a_k^2 + \sum_k a_{kR}^2 + 2 \sum_k a_k a_{kR} \underbrace{e^{i(\phi_k - \phi_{kR})}}_{1} = 4 \sum_k a_k^2 \equiv 4|A|^2 \end{aligned} \tag{2.17}$$

since $a_k = a_{kR}$ and $\phi_k = \phi_{kR}$.
Without phase-coherency or time reversal symmetry, the last term averages out and we have

$$R(m \to m) = |A|^2 + |A_R|^2 \equiv \sum_k a_k^2 + \sum_k a_{kR}^2 + 2 \underbrace{\sum_k a_k a_{kR} e^{i(\phi_k - \phi_{kR})}}_{0} = 2 \sum_k a_k^2 \equiv 2|A|^2 \tag{2.18}$$

which is exactly the half of probability found for coherent backscattering. Thus, the perfect coherence between the pairs of time-reversed paths leads to a doubling of backscattering probability which reflects in a tendency of electrons towards localization and macroscopically results in an increase of resistance.

The order of magnitude of the correction is $\sim 2e^2/h$, result that can be derived considering the Landauer formula:

$$G = \frac{2e^2}{h} MT \equiv \frac{2e^2}{h} M(1-R) \tag{2.19}$$

where R is the reflection probability. It is possible to show that classically, for a resistor of length L, we have

$$T = \frac{L_0}{L+L_0} \qquad R = \frac{L}{L+L_0} \tag{2.20}$$

with L_0 of the order of the mean free path. Assuming the scatterers as isotropic, the probability that an incident electron in mode m is reflected in a final state n ($n = 1, 2, ..., M$) is

$$R(m \to n) = \frac{1}{M}\frac{L}{L+L_0} \tag{2.21}$$

equal for all modes. If we take into account quantum interference this result still holds on the average for $m \neq n$, while is doubled for backscattering:

$$\langle R(m \to n)\rangle = \begin{cases} \frac{1}{M}\frac{L}{L+L_0} & m \neq n \\ \frac{2}{M}\frac{L}{L+L_0} & m = n. \end{cases} \tag{2.22}$$

Thus the average reflection probability turns out to be a little larger than the classical value

$$\langle R\rangle = \sum_n \langle R(m \to n)\rangle = (M-1)\frac{1}{M}\frac{L}{L+L_0} + \frac{2}{M}\frac{L}{L+L_0} = \frac{L}{L+L_0} + \frac{1}{M}\frac{L}{L+L_0} \tag{2.23}$$

and the transmission probability must then be smaller than its classical value from the same amount

$$\langle T_Q\rangle = T_{CL} - \frac{1}{M}\frac{L}{L+L_0} = T_{CL} - \frac{1}{M} \; since \; L >> L_0. \tag{2.24}$$

Hence from (2.19) we can easily obtain

$$\langle G_Q\rangle = G_{CL} - \frac{2e^2}{h}. \tag{2.25}$$

We can extend the same argument to conductors with dimension much larger than the phase-coherent length, considering them as a combination in series of independent phase-coherent units, each of length L_ϕ. This is the reason why the weak-localization (WL) effect survives also in bigger samples. For a two-dimensional conductor with width $W << L_\phi$ we find

$$\langle G_Q\rangle = \frac{\sigma_Q W}{L_\phi} = \frac{\sigma_{CL} W}{L_\phi} - \frac{2e^2}{h} \tag{2.26}$$

so that the correct conductivity is related to the classical one as follows:

$$\sigma_Q = \sigma_{CL} - \frac{2e^2}{h}\frac{L_\phi}{W}. \tag{2.27}$$

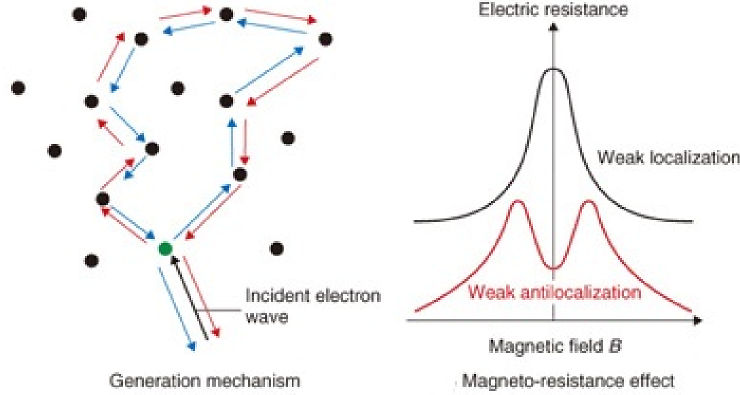

Figure 2.6: Time reversed self-crossing trajectories originating from the starting point indicated by the green scatterer (left). Resistance in function of magnetic field in regime of weak localization and weak anti-localization (right).

It can be shown that the generalization of this result for a 2D sample of arbitrary width is given by [43]:

$$\sigma_Q = \sigma_{CL} - \frac{2e^2}{\pi \hbar} ln \left(\frac{L_\phi}{l_m} \right). \tag{2.28}$$

The unique signature of weak localization is the fact that it can be destroyed by a small magnetic field, which breaks the time reversal symmetry. An applied field B leads indeed to a phase-shift $\Delta\phi_k$ in the amplitude of every path k, which is proportional to the line integral of the vector potential A along that path and whose sign is opposite for correspondent time-reversed paths:

$$\Delta\phi_k = -\frac{e}{\hbar} \int_k \mathbf{A} \cdot d\mathbf{l} \qquad \Delta\phi_{kR} = -\frac{e}{\hbar} \int_{kR} \mathbf{A} \cdot d\mathbf{l}_R = \frac{e}{\hbar} \int_k \mathbf{A} \cdot d\mathbf{l}. \tag{2.29}$$

The phase difference between every couple of closed trajectories is then

$$\Delta\phi_{kR} - \Delta\phi_k = \frac{2e}{\hbar} \oint_k \mathbf{A} \cdot d\mathbf{l} = \int_{S_k} (\nabla \wedge \mathbf{A}) \cdot dS_k = \frac{2e}{\hbar} \mathbf{\Phi} \tag{2.30}$$

where Φ is the magnetic flux through the area S_k enclosed by the path [50]. Since the possible counter-propagating trajectories enclose different areas, the phases are random and the interference terms giving rise to weak localization cancel out on the average. The lower backscattering probability when time reversal symmetry is broken is responsible for the decrease of resistance in function of magnetic field experimentally observed, which is sketched in *figure 2.6*.

2.4.2 Weak anti-localization

In systems with not negligible spin-orbit coupling, the interference between self-crossing paths leads to a correction in the resistance of opposite sign respect to WL, called for this reason weak anti-localization.

The previous discussion can be extended to these situations taking in consideration the spin

of the electrons, which plays now an important role. As we will see better in section 2.6.1, in presence of SOI the spin precesses randomly around a fictitious magnetic field that the electron sees in its reference frame. Thus the spin of the carriers rotates as it goes around a self-intersecting path and, due to the coupling to the momentum, the direction of the rotation is opposite for the two counter-propagating loops. It can be shown that this leads to a destructive interference between the paths which reflects in a lower resistance [51].
Similarly to weak localization, the phenomenon is suppressed by small magnetic fields, but, as we can see in *figure 2.6*, its signature is a decrease in resistance.
The precise WAL correction to the conductivity can be derived from the *Hikami-Larkin-Nagaoka* theory and, in two dimensions in case of spin-orbit interaction due to the presence of impurities, results to be [51]:

$$\begin{aligned}\Delta\sigma_{xx}(B) = -\frac{e^2}{\pi h}\Bigg[&\frac{1}{2}\Psi\left(\frac{1}{2}+\frac{B_\phi}{B}\right)-\frac{1}{2}\ln\left(\frac{B_\phi}{B}\right)-\Psi\left(\frac{1}{2}+\frac{B_\phi+B_{so}}{B}\right)+\\ &+\ln\left(\frac{B_\phi+B_{so}}{B}\right)-\frac{1}{2}\Psi\left(\frac{1}{2}+\frac{B_\phi+2B_{so}}{B}\right)+\frac{1}{2}\ln\left(\frac{B_\phi+2B_{so}}{B}\right)\Bigg].\end{aligned} \tag{2.31}$$

In this complex formula Ψ is the *digamma function*, B_ϕ is the phase coherence characteristic field, which is roughly the magnetic field required to destroy phase coherence, and B_{so} the spin-orbit characteristic field that can be considered a measure of the strength of the spin-orbit interaction. They are respectively related to the electron phase coherent time τ_ϕ and the spin relaxation time τ_{so} by the following expressions

$$B_\phi = \frac{h}{8\pi e D}\tau_\phi^{-1} \qquad\qquad B_{so} = \frac{h}{8\pi e D}\tau_{so}^{-1} \tag{2.32}$$

where D is the *diffusion constant* of the carriers.
As we will see in the next chapter, equation (2.31) is used to fit magnetoresistance measurements of thin layers WTe_2, material characterized by strong a spin-orbit coupling and thus expected to show weak anti-localization.

WL and WAL phenomena are precursor of *strong localization*, also called *Anderson localization*, which occurs at strong disorder. When the degree of randomness in a lattice is sufficiently large, the interference between multiple-scattering paths can completely localize the electron wavefunction inside the disordered medium. Thus a crossover from diffusive to hopping transport occurs and the system becomes an insulator [52].

2.4.3 Universal Conductance Fluctuations

In phase-coherent conductors having dimensions inferior to the phase-relaxation length, the interference of waves scattered from impurities is responsible for the appearance of conductance fluctuations.
The backscattering probability in (2.17) can be written in a more general way, considering also non time-reversed paths:

$$R(m \to m) = \sum_k a_k^2 + 2\sum_k a_k a_{kR} e^{i(\phi_k-\phi_{kR})} + 2\sum_{j<k} a_k a_j e^{i(\phi_k-\phi_j)} \tag{2.33}$$

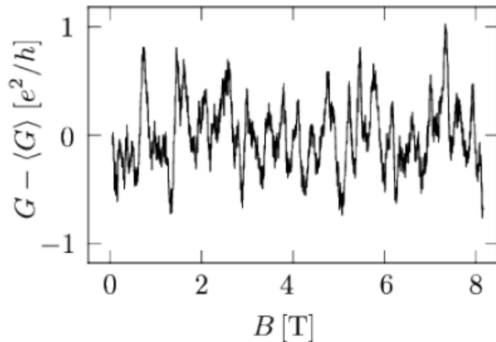

Figure 2.7: Conductance fluctuations as a function of magnetic field of a gold wire at 10mK. Adapted from [53].

where the first term is the classical probability, the second term is responsible to WL or WAL correction, while the third one gives a random contribution of magnitude $2e^2/h$. It is this last term that is responsible for the universal conductance fluctuations, which are not observed in larger systems because these random contributions cancel out when averaged over different coherent units. The interference pattern depends in fact on the relative position of the scatterers, which naturally is different from sample to sample.
Experimentally the universal conductance fluctuations are observed varying the electron density or the magnetic field, as shown in *figure 2.7.* In either case indeed the Fermi wavelength of the electrons is shifted and the phase relationship among different paths modifies randomly. From a statistical point of view, this has the same effect on the interference as a change in the impurity configuration of the system.
As their name suggests, the peculiarity of these fluctuations is the fact they are always of the same size in different mesoscopic samples even if the background conductance varies over several order of magnitude. For this reason and due to their reproducibility they cannot be confused with experimental noise.

In small samples the UCFs can eclipse the WL or WAL effect since both phenomena occur simultaneously and their magnitude is comparable. For that reason to highlight the quantum corrections to the conductivity is necessary to do an ensemble averaging procedure that cancels out the fluctuations. Since preparing many microscopically different samples is not feasible, what is usually done is to mimic a change in the impurity configuration by a small modulation of external parameters, like the carrier density or the magnetic field [54].

2.5 The Quantum Hall Effect

If a strong perpendicular magnetic field (10-20 T) is applied to a two-dimensional electron gas at very low temperature (T∼1.5 K), the cyclotron motion of the electrons leads to the observation of plateaus in the *Hall resistance* R_{xy}, that are quantized in units of h/e^2. This phenomenon, observed for the first time in 1980 by K. von Klitzing, is known as quantum Hall effect. Unlike the conductance of a ballistic conductors, which has been shown to vary in

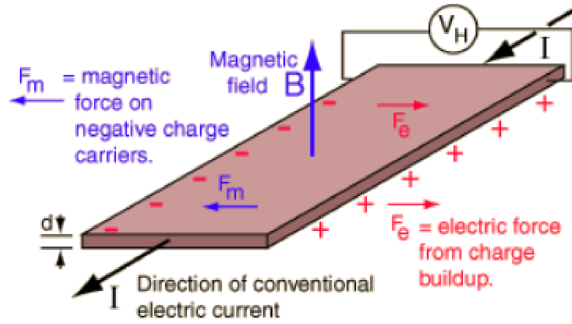

Figure 2.8: Schematic representation of the Hall effect.

discrete steps of $2e^2/h$ with deviations of few per cent, the value of R_{xy} has been determined with an accuracy of parts per billion. Thanks to this "exact quantization", the *von Klitzing constant* $R_K = h/e^2 \sim 25.8$ KΩ has been chosen by the International Committee for Weights and Measures as a resistance standard. The impressive accuracy of R_{xy} arises from the near complete suppression of momentum relaxation processes in the quantum Hall state, which then behaves as a truly ballistic conductor with mean free paths of the order of millimetres. The suppression of backscattering probability is not due to an unusual purity of the samples but is related to the formation of a "divided highway" for electrons. In the quantum Hall regime, in fact, states carrying current in one direction are localized on one edge of the sample, while those propagating in the opposite direction are localized on the other one.

We will start this section with an introduction on classical magnetotransport, particularly in relation to the Hall effect. First we will show an easy picture using the Drude model, then we generalize the results for a semimetal where both electrons and holes are present.
After that, will see how, in the quantum regime, an applied magnetic field on a 2DEG results in the formation of the *Landau levels*, fact that macroscopically reflects in the *Integer Quantum Hall effect* (IQHE) at high fields and in the *Shubnikov-de Haas oscillations* at low fields. We will finally discuss the topological nature of the QHE since is conceptually important for the discussion of the quantum spin Hall effect in 2D topological insulators, which will be addressed in the last part of the chapter.

2.5.1 Classical magnetotransport

Let's consider a thin conducting slab as the one shown in *figure 2.8*. Trivially, when a voltage is applied in the longitudinal direction a current will flow parallel to the induced electric field. Now, if we consider to apply a magnetic field perpendicular to the plane of the slab, the electrons will be deflected by the Lorentz force toward one side of the conductor. Thus a current density will flow in the direction orthogonal to the applied electric field, leading to a charge accumulation and to the consequent develop of a transversal electric field. In stationary condition this field exactly compensates the Lorentz force and no current flows perpendicular to the applied electric field. Hence, a voltage drop is established across the bar, that is called *Hall voltage* V_H and results to be linearly proportional to the magnetic field.

More formally, we can consider the equation of motion of an electron of momentum p and *effective mass* m^*, according to the *Drude model*

$$\frac{d\mathbf{p}}{dt} = -e\left(\mathbf{E} + \frac{\mathbf{p}}{m^*} \wedge \mathbf{B}\right) - \frac{\mathbf{p}}{\tau} \tag{2.34}$$

where the last term represents a frictional contribution due to collisions with a characteristic *relaxation time* τ.
For electrons moving in a plane xy and an applied magnetic field in direction z, in stationary conditions (d$\mathbf{p}$/dt=0), we have:

$$\begin{cases} eE_x = -\omega_c p_y - \frac{p_x}{\tau} \\ eE_y = \omega_c p_x - \frac{p_y}{\tau} \end{cases} \tag{2.35}$$

with ω_c *cyclotron frequency* of the electron inside a magnetic field:

$$\omega_c = \frac{e\mathbf{B}}{m^*}. \tag{2.36}$$

Using the Drude conductivity σ

$$\sigma = \frac{ne^2\tau}{m^*} \tag{2.37}$$

and considering the current density $j = -env$, where n is the electron density and v the velocity, we can rewrite equations (2.35) as follows:

$$\begin{cases} \sigma E_x = \omega_c \tau j_y + j_x \\ \sigma E_y = -\omega_c \tau j_x + j_y \end{cases} \tag{2.38}$$

which in a matrix form is

$$\begin{pmatrix} E_x \\ E_y \end{pmatrix} = \frac{1}{\sigma}\begin{pmatrix} 1 & \omega_c\tau \\ -\omega_c\tau & 1 \end{pmatrix}\begin{pmatrix} j_x \\ j_y \end{pmatrix}. \tag{2.39}$$

Recalling that $E = \rho j$ and introducing the *mobility* μ

$$\mu = -\frac{e\tau}{m^*} \tag{2.40}$$

we obtain for the *resistivity tensor* ρ:

$$\begin{pmatrix} \rho_{xx} & \rho_{xy} \\ \rho_{yx} & \rho_{yy} \end{pmatrix} = \frac{1}{\sigma}\begin{pmatrix} 1 & \omega_c\tau \\ -\omega_c\tau & 1 \end{pmatrix} = \frac{1}{\sigma}\begin{pmatrix} 1 & -\mu B \\ \mu B & 1 \end{pmatrix}. \tag{2.41}$$

Then, while the longitudinal resistivity is constant, the transversal resistivity, called *Hall resistivity* increases linearly with magnetic field [43]:

$$\rho_{yx} = -\rho_{xy} = \frac{\mu B}{\sigma} = -\frac{B}{ne} \tag{2.42}$$

We can generalize this simple model considering ambipolar transport. Summing the conductivity tensors for the two carriers, in a semimetal with an electron density n and a holes

density p, and inverting the sum [57], it is possible to find the longitudinal ρ_{xx} and transverse ρ_{xy} resistivities:

$$\rho_{xx} = \frac{(n\mu_e + p\mu_h) + (n\mu_e\mu_h^2 + p\mu_e^2\mu_h)B^2}{e[(n\mu_e + p\mu_h)^2 + (p-n)^2\mu_e^2\mu_h^2 B^2]} \tag{2.43}$$

$$\rho_{xy} = \frac{(p\mu_h^2 - n\mu_e^2)B + \mu_e^2\mu_n^2(p-n)B^3}{e[(n\mu_e + p\mu_h)^2 + (p-n)^2\mu_e^2\mu_h^2 B^2]}. \tag{2.44}$$

We notice that the behaviour is quite complicated and it depends on the relative values of the densities and mobilities for the two charge carriers. In particular the Hall resistivity is proportional to B at low field and to B^3 at high field, with proportionality coefficients sensibly related in magnitude and sign to n, p, μ_e and μ_h.
Analysing the dependence of the longitudinal resistance we can introduce another quantity, the *magnetoresistance*, which will be useful for the study of magnetotransport in WTe_2. Considering (2.43) we have:

$$\frac{\Delta\rho}{\rho} = \frac{\rho_{xx}(B) - \rho_{xx}(0)}{\rho_{xx}(0)} = \frac{(n\mu_e + p\mu_h)^2 + \mu_e\mu_h(n\mu_e + p\mu_h)(p\mu_e + n\mu_h)B^2}{(n\mu_e + p\mu_h)^2 + (p-n)^2\mu_e^2\mu_h^2 B^2} - 1. \tag{2.45}$$

A relevant simplification of this expression arises if we deal with a *compensated semimetal*, i. e. the concentration of holes and electrons is nearly equal. When $n \sim p$ the magnetoresistance increases quadratically without saturation:

$$\frac{\Delta\rho}{\rho} = \mu_e\mu_h B^2 \qquad if \quad (n\mu_e + p\mu_h)^2 \gg (p-n)^2\mu_e^2\mu_h^2 B^2. \tag{2.46}$$

A similar behaviour is observed experimentally in WTe_2, which for that reason has been hypothesized to be the first example of a compensated semimetal [38].

2.5.2 Landau levels

Let's consider now a two-dimensional electron gas in presence of a perpendicular magnetic field. The effective Hamiltonian is

$$H = \frac{1}{2m_e}\left(\mathbf{p} + \frac{e}{c}\mathbf{A}\right)^2 \tag{2.47}$$

where m_e is the electron mass. To solve the associated Schrödinger equation it is convenient to choose the *Landau gauge* in which the vector potential has the form:

$$\mathbf{A} = (-By, 0, 0). \tag{2.48}$$

The Schrödinger equation is then

$$\frac{1}{2m_e}\left[\left(p_x - \frac{e}{c}By\right)^2 + p_y^2\right]\psi = E\psi \tag{2.49}$$

that has solutions of the form

$$\psi(x.y) = \frac{1}{\sqrt{L_x}}e^{ik_x x}\phi(y) \tag{2.50}$$

whit L_x the confinement length in the x direction. Inserting these wavefunctions in (2.49) we obtain the following equation for $\phi(y)$

$$\frac{1}{2m_e}\left[\left(\hbar k_x - \frac{e}{c}By\right)^2 + p_y^2\right]\phi(y) = E\phi(y) \tag{2.51}$$

that can be rewritten as

$$\begin{gathered}\left[\frac{1}{2}m\omega_c^2(y-y_k)^2 - \frac{\hbar^2}{2m_e}\frac{\partial^2}{\partial y^2}\right]\phi(y) = E\phi(y) \\ with \quad y_k = \frac{\hbar c}{eB}k_x \quad and \quad \omega_c = \frac{eB}{mc}\end{gathered} \tag{2.52}$$

which is the Schrödinger equation for a harmonic oscillator with a cyclotron frequency ω_c and displaced from the origin by y_k. Hence, the presence of a magnetic field confines the electrons in circular closed orbits characterized by discrete energy values, the Landau levels (LLs)

$$E_{n,k} = \left(n + \frac{1}{2}\right)\hbar\omega_c \qquad with \quad n = 1, 2, 3... \tag{2.53}$$

that have an energy separation of $\hbar\omega_c = 2\mu_B B$, with $\mu_B = \frac{e\hbar}{2m_e c}$ *Bohr magneton.* The corresponding eigenfunctions are therefore given by the product of a plane-wave in the x direction and a quantum harmonic oscillator wavefunction along y

$$\psi(x,y) = \frac{1}{\sqrt{L_x}}e^{ik_x x}H_n\left(\frac{y-y_k}{l_B}\right)e^{-\frac{(y-y_k)^2}{2l_B^2}} \qquad with \quad l_B = \sqrt{\frac{\hbar c}{eB}} \tag{2.54}$$

where H_n are the *Hermite polynomials* and l_B the *magnetic length.*
Since the energy levels do not depend on the quantum number k, states with the same n and different k are degenerate. We can find the number of states associated to each Landau level imposing boundary conditions to the wavefunctions. The plane waves are periodic along the x direction so that the allowed values for the wave-vector are

$$k_x = j\frac{2\pi}{L_x} \tag{2.55}$$

with j integer and determined by the confinement in the y dimension L_y of the wavefunctions centred in y_k

$$0 < y_k = \frac{\hbar c}{eB}j\frac{2\pi}{L_x} < L_y. \tag{2.56}$$

Reversing this relation we can find the condition on j, whose maximum value represents the level degeneracy

$$N_{deg} = \frac{BL_xL_y}{\Phi_0} \qquad with \quad \Phi_0 = \frac{hc}{e} = 2.07 \cdot 10^{-15}\,Tm^2 \tag{2.57}$$

where Φ_0 is the so-called *quantum of magnetic flux.* The number of degenerate states in every Landau level is therefore the number of flux quanta through the system and is proportional

to the applied field. For typical values of magnetic fields and sample sizes, the degeneracy is usually very large.
The number of occupied levels at a given electron density n_{2D} it is given by:

$$\nu = \frac{N_{electrons}}{N_{deg}} = \frac{n_{2D}\Phi_0}{B} \tag{2.58}$$

quantity referred as *filling factor*. Thus, increasing the magnetic field, the degeneracy of each level increases and the number of occupied levels decreases.

It is easy to see that electrons in the Landau levels do not contribute to the current flowing through the system. Inserting the eigenfunctions (2.54) in the quantum mechanical expression of the current

$$\mathbf{J}_{n,k} = \int dxdy\, e \left[\frac{\hbar}{2im}(\psi^*\nabla\psi - \psi\nabla\psi^*) - \frac{e}{mc}|\psi|^2\mathbf{A} \right] \tag{2.59}$$

we find that the y component vanishes because $A_y = 0$ and the Hermite polynomials are real functions. Nevertheless, also the x component turns out to be zero, how we could expect from the fact the current is proportional to the group velocity of the plane wave, which is zero since the energy does not depend on k.
In conclusion the bulk of a Hall-bar in a 2DEG is an insulator, result which is surprising because without a current flown we would not be able to measure a Hall voltage, like we actually do. The solution of this paradox comes out considering that the finite dimensions of the system lead to the presence of a confining potential at the edges. This causes a k dependence in the energy spectrum which results in a non-zero group velocity of the wavefunctions, as we will see in the following paragraph.

2.5.3 IQHE

At the edges of a semiconducting heterostructure which hosts a 2DEG there is a a band bending due to the Schottky barrier at the interface with the vacuum. The presence of this confining potential modifies the Landau levels at the edges, where, as we can see from the dispersion relation in *figure 2.9 (a)*, there are allowed states with a continuous distribution of energies. These are referred to as *edge states* and they are responsible for the conduction in the quantum Hall state.
If the confining potential $V(y)$ is smooth on the scale of the magnetic length, which corresponds to the spatial extension of the wavefunction, it can be shown that the energy spectrum becomes

$$E_{n,k} = \left(n + \frac{1}{2}\right)\hbar\omega_c + V(y_k). \tag{2.60}$$

Hence, the associated group velocity

$$v_k = \frac{1}{\hbar}\frac{\partial V(y_k)}{\partial k} \tag{2.61}$$

assumes a finite value as long as the state is centred in the region where the potential is not constant, i.e. at the edges. It should be noticed that, since the derivative of the potential

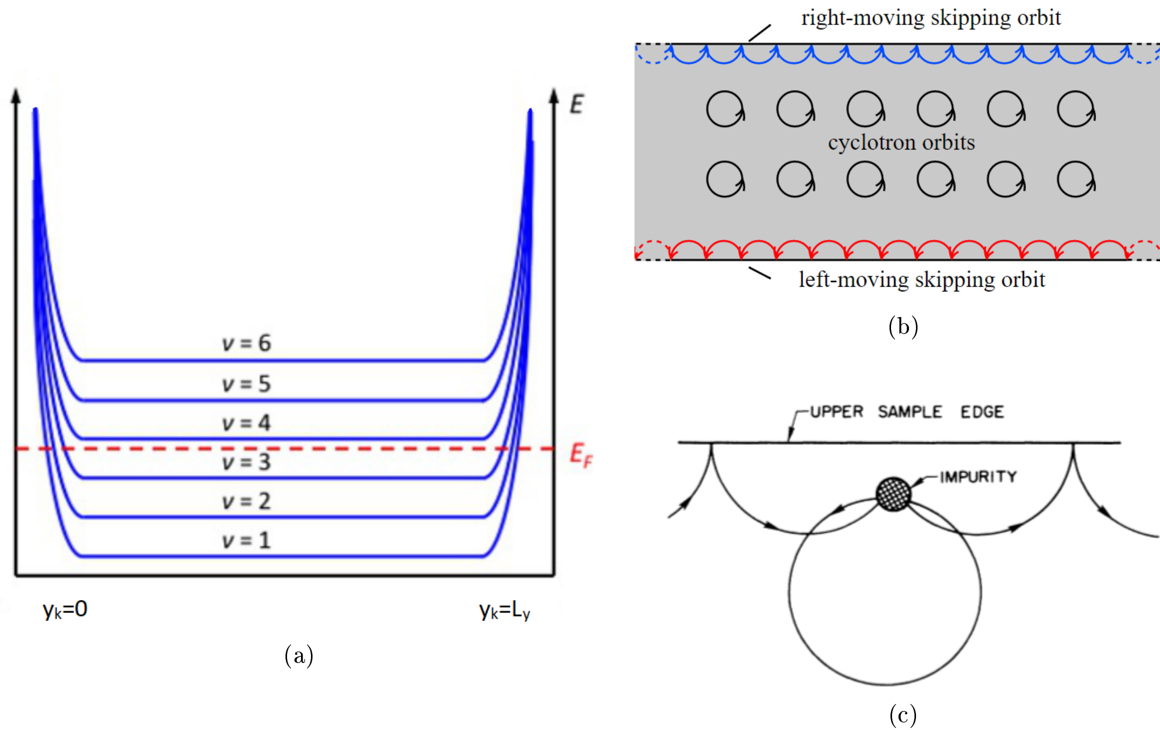

Figure 2.9: (a) Landau levels in the presence of a confining potential at the edges. (b) Representation of the classical orbits of 2D electrons in a perpendicular magnetic field, showing cyclotron orbits in the bulk and skipping orbits at the edge. (c) Ineffectiveness of a scatterer along one edge; at high magnetic field backscattering over distances large compared to the cyclotron diameter is suppressed [55].

changes sign at the two sides of the sample, the group velocities of electrons propagating along different edges are opposite. This is at the origin of the *chirality* of edge states, characterized by a defined direction at a given edge.
Now, if we consider the situation in which the Fermi energy lays in the gap between two Landau levels, we find that the edge states are still present and their number is equal to the filling factor, i.e. to the number of filled levels. Thus, when we apply a bias across two contacts on opposite sides of the 2DEG, even if the bulk is insulating the current can flow at the edges. In particular, according to what said before, all the electrons at one edge will have the same direction of motion that is opposite for opposite edges. This has an important implication: electrons at the edges cannot be easily scattered back because, in order to reverse their propagation direction, they have to cross the insulating bulk of the 2DEG. Since for distances longer than 1 micron the scattering rate of such a process is negligible, the chirality of the edge states results therefore in the suppression of the backscattering probability. As a consequence, electrons injected into these conducting channels are transmitted from one contact to the other with unit probability and the edge states are basically equivalent to one dimensional modes in a ballistic conductor. Then, recalling the (2.10) and considering the Zeeman splitting at high magnetic fields, we can easily conclude that each state is characterized by a conductance of e^2/h.

It is possible to understand most of the results we have obtained quantum mechanically,

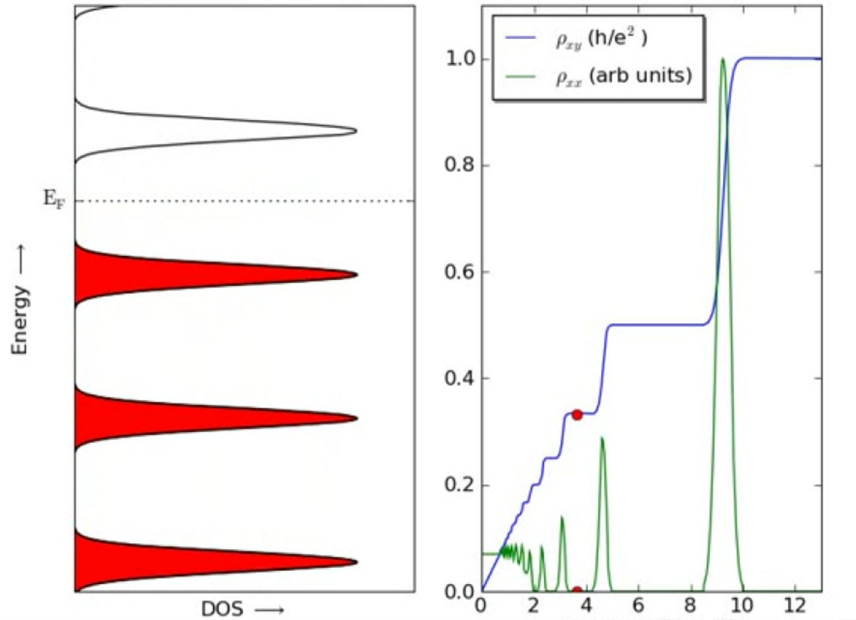

Figure 2.10: Quantum Hall effect in a 2DEG. When the Fermi energy is in the gap between two Landau level the Hall resistivity ρ_{xy} is quantized while the longitudinal resistivity ρ_{xx} vanishes.

analysing the electron motion in presence of a perpendicular magnetic field through a simple semiclassical picture. Classically, the Lorentz force generated by the field, in two dimensions, localizes the electrons in circular closed orbits which give no contributions to the current. However, close to the interface the electrons are reflected by the edge and the cyclotron orbits are modified in the so-called *skipping orbit*, as depicted in *figure 2.9 (b)*. It is easy to see that this causes the electrons to propagate along the edges and that the direction of propagation is opposite for the two edges. Moreover, as long as the distance between them is much larger than the diameter of the cyclotron orbit, the backscattering is not allowed because electrons at one side are not able to reach the other side. Looking at *figure 2.9 (c)*, we can intuitively see why scattering processes do not affect the edge states: when an electron is scattered by an impurity along one edge, after a cyclotron orbit it is scattered again and it returns in the initial trajectory.

Longitudinal and Hall resistance

The strong signature of the integer quantum Hall effect is the peculiar behaviour of the transverse (or Hall) resistance R_H and of the longitudinal resistance R_L in function of the magnetic field. As we can see in *figure 2.10*, R_H shows characteristic plateaus in correspondence of which R_L vanishes.
The name *integer* is related to the fact that the Hall conductance is quantized in integer multiples of e^2/h, differently to what happen at even higher magnetic fields where plateaus appear at fractional multiples of the von Klitzing constant. This phenomenon is the so-called *fractional*

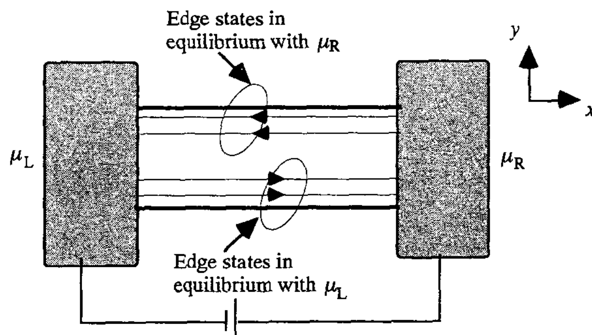

Figure 2.11: A conductor in the quantum Hall regime [43].

quantum Hall effect, which we will not describe in the present thesis.
Thanks to the considerations of the previous paragraphs, we have all the tools necessary to understand the characteristic behaviour of the resistance in the Quantum Hall (QH) regime. Let's consider a conductor in the QH state as the one depicted in *figure 2.11*, with two ideal contacts at opposite sides kept at different potentials. As a result of the ideality of the probes and of the complete suppression of backscattering, electrons originating in the in left contact and propagating toward the right one are completely in equilibrium with the left contact and have a chemical potential equal to μ_L. They are unaffected by the potential at the right contact μ_R since no electrons originating in this probe can access to their conductive channels due to the chirality of edge states. The same argument applies to states originating in the right contact which are in equilibrium at a potential μ_R. Then, the longitudinal voltage drop V_L measured by two probes located anywhere at the same side of the sample is zero, while the Hall voltage V_H between two probes on opposite sides is equal to the applied voltage:

$$V_L = 0 \qquad V_H = \frac{1}{e}(\mu_L - \mu_R). \tag{2.62}$$

The corresponding Hall resistance scales inversely to the number of occupied Landau levels and assumes the discrete values:

$$R_H = \frac{1}{\nu}\frac{h}{e^2} \qquad with \quad \nu = 1, 2, 3, ... \tag{2.63}$$

It is important to notice that this situation arises only if the Fermi energy lies in the gap between two Landau levels and thus the bulk is insulating. Otherwise, there would be a continuous distribution of allowed states from one edge to the other that would increase the backscattering probability. This is the origin of the maximum in the longitudinal resistance observed in correspondence of a bulk Landau level.

2.5.4 Shubnikov-de Haas oscillations

In real samples the density of states (DOS or D(E)) of the Landau levels has not the form of delta functions that we would expect from theory but it is broadened, as we can see in *figure*

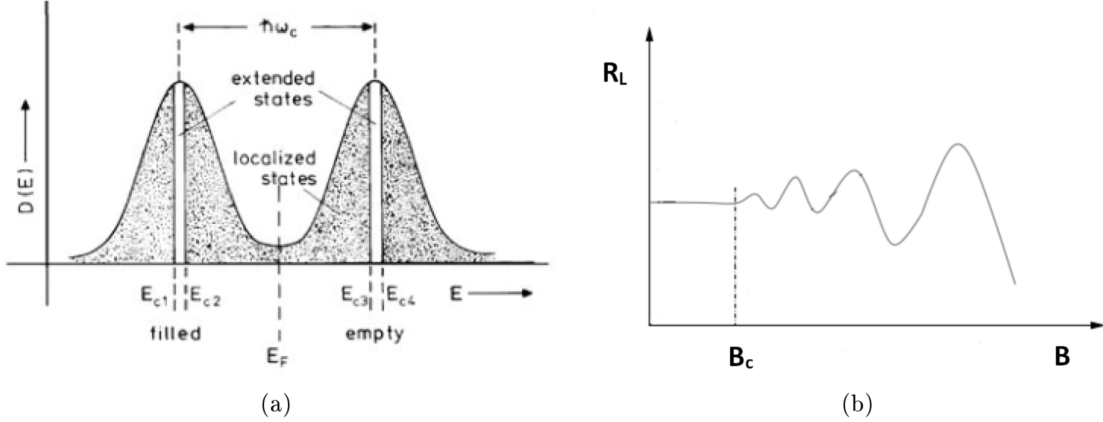

Figure 2.12: (a) Landau levels broadening in presence of disorder. (b) Shubnikov-de Haas oscillations of the longitudinal resistance, visible above the critical magnetic field.

2.12 (a). The inevitable presence of impurities and disorder leads indeed to the existence of states inside the gap between two LLs, the so-called *localized states*. As the name suggests, these states are related to closed equipotential orbits around a potential summit or valley and do not contribute to transport, differently from the *extended states* which are in correspondence of the Landau levels. The main consequence of the localized states is the experimental observation of non perfectly sharp jumps between two adjacent plateaus of the Hall resistance.
In presence of strong disorder the broadening of the Landau levels can be even larger than the energy separation between adjacent levels, leading to a continuum of available extended states. In this case, when the Fermi Energy sweeps the LLs the longitudinal resistance never reaches zero but still shows oscillations, known as Shubnikov-de Haas oscillations (SdH), whose periodicity is given by the level disposition. The phenomenon, which took the name of its discoverers, was observed for the first time in 1930, much before of the IQHE because of the lower quality required for the samples.
As we can see in *figure 2.12 (b)*, the SdH oscillations arises only above a certain value of magnetic field, referred as *critical field* B_c. In order for LL discretization to be relevant, in fact, the magnetic field has to be strong enough to allow electrons to complete at least a few orbits before losing its momentum due to scattering. This lead to the condition:

$$\omega_c^{-1} \ll \tau \tag{2.64}$$

We would have come to the same conclusion, arguing that the peaks in the density of states are well defined only if their spacing is much grater than the broadening caused by scattering:

$$\hbar\omega_c \gg \hbar/\tau \tag{2.65}$$

Recalling the (2.36) and the (2.40) the criterion can be rewritten as a condition on the field:

$$B \gg \mu^{-1}. \tag{2.66}$$

Thus the SdH oscillations are visible at lower magnetic fields for high mobility samples.
In our work on WTe_2 we observed these oscillations in the magnetoresistance and trough the analysis of their associated frequencies we have been able to extract the mobilities and the densities of the charge carriers, as we will see in the next chapter.

2.5.5 Topological nature of the QHE

The discovery of the QHE triggered considerable theoretical work which has resulted in several impressively deep ideas in condensed matter physics. One of these ideas was put forward by Thouless et al. in 1982, who were the first to realize the connection between the Hall conductivity and topology that we introduce here [58]. In particular, the edge states were formally shown to be a manifestation of the non-trivial topology of the insulating state. This pioneering work stimulated others studies and few years later Haldane proposed a model for graphene predicting that the quantum Hall effect could be generated in absence of Landau levels, provided that the time reversal symmetry and parity are broken [59]. A description of the Haldane model goes beyond the purpose of the present work and in the following paragraph we will just discuss the link between the topology of the bulk states and the existence of edge states. This is the key reason why the quantum Hall state can be effectively seen as a 2D topological insulator.
The concept of topology in insulating systems is associated to the existence of a so-called topological index that distinguishes insulators in different equivalence classes, in an analogous way as geometry objects can be classified according with the number of "holes" in their surfaces. This index, which is a topological invariant - i.e. it is insensible to continuous deformations of the bulk electronic band structure that do not close the energy gap- is known as *Chern number*. It is defined as:

$$C_n = \frac{1}{2\pi} \oint \oint_{BZ} \mathcal{F}_n(\mathbf{k}) d\mathbf{k}. \tag{2.67}$$

where $\mathcal{F}_n$ is the *Berry curvature* in the reciprocal space and the integral is over the whole Brillouin Zone. Considering Bloch waves

$$\psi_{n,\mathbf{k}}(\mathbf{r}) = u_{n,\mathbf{k}}(\mathbf{r}) exp(i\mathbf{kr}) \tag{2.68}$$

the Berry curvature of a band n at momentum point k is

$$\mathcal{F}_n(\mathbf{k}) = \iint_{UC} [\nabla_{\mathbf{k}} u_{n,\mathbf{k}}(\mathbf{r})]^* \wedge \nabla_{\mathbf{k}} u_{n,\mathbf{k}}(\mathbf{r}) d\mathbf{r} = \epsilon_{ij} \iint_{UC} [\partial_{k_i} u_{n,\mathbf{k}}(\mathbf{r})]^* \, \partial_{k_j} u_{n,\mathbf{k}}(\mathbf{r}) d\mathbf{r} \tag{2.69}$$

where ϵ_{ij} is the Levi-Civita symbol and the integral is performed on the unit cell.
For each band, it is possible to define such a topological index so that the total Chern number is given by the sum on all the filled bands:

$$C = \sum_{filled\ bands} C_n \tag{2.70}$$

The Chern number for an insulator assumes integer values and gives exactly the number of chiral edge states of a system: if $C = 0$ we have a trivial insulator, while if $C \neq 0$ we have a

topological insulator with C metallic edge states and a Hall conductivity of $\sigma_{xy} = Ce^2/h$.
The topological nature of the edge states is at the origin of the incredible accuracy of the Hall conductivity in a quantum Hall insulator. Since σ_{xy} is related to the topology of the quantum wavefunction, it does not vary as long the perturbation we apply to the system does not change the topological structure. Then if the perturbation is not strong enough to turn the insulating state into a metal, it does not matter at all. This is the reason why the edge states are so robust and they are said to be "topologically protected" .

2.6 The Quantum Spin Hall Effect

The Haldane model for spinless fermions in two dimensions can be generalized to an electron system with defined spin. This is what has been done by Kane and Male in 2005, who developed a model that can be simply regarded as the combination of two layers of the Haldane model for electrons with spin-up and spin-down. They introduced the spin-orbit coupling to replace the periodic magnetic flux and predicted that, if the spin-orbit interaction is strong enough to open a bandgap in the material, an insulating state with non trivial topology could exist even in absence of magnetic field. The model theorizes a new state of matter, the Quantum Spin Hall (QSH) state, which is characterized by a bulk bandgap closed by the presence of helical edge states. These helical states, localized at the boundaries of the material, are strongly connected to the non trivial topology of the band structure in systems with strong spin-orbit coupling. For that reason the QSH state is also referred as a two-dimensional topological insulator. In this respect, in the previous section we have seen how the topological nature of the quantum Hall effect is related to the existence of a topological index. In addition to the Chern number, if we require certain symmetries, it is possible to define other topological indices and if any of those indices is non-zero, the insulator is also a topological insulator. Differently from the quantum Hall state which exists only in 2D since the Chern number can be defined only in even dimensions, it can be shown that in presence of time-reversal symmetry we can have topological insulators also in three dimensions. With reference to the intrinsic origin of their helical states these materials have been called *spin-orbit topological insulators*.
For a topological insulator to form, spin–orbit coupling must be strong enough to modify the electronic structure significantly, which suggests that heavy-element, small-bandgap semiconductors are the most promising candidates. The magnitude of SOI is indeed proportional to the atomic number and, for the interaction to be effective, the bandgap of the material cannot be too large. Despite the progress made in synthesizing 3D topological insulators, the experimental realization of 2D TIs is still limited to quantum wells systems of (Hg,Cd)Te and InAs/GaSb. Nevertheless, recently strong hallmarks of the quantum spin Hall effect have been observed in monolayer 1T'-WTe_2, as we will see in the following chapter.

In the following section, we will first briefly describe the spin-orbit interaction that is responsible for the existence of *Kramers doublets* in these materials. Then we will outline the main features of helical edge states in the QSH state, with a particular focus to the transport properties which are analysed using the Landauer-Büttiker formalism.

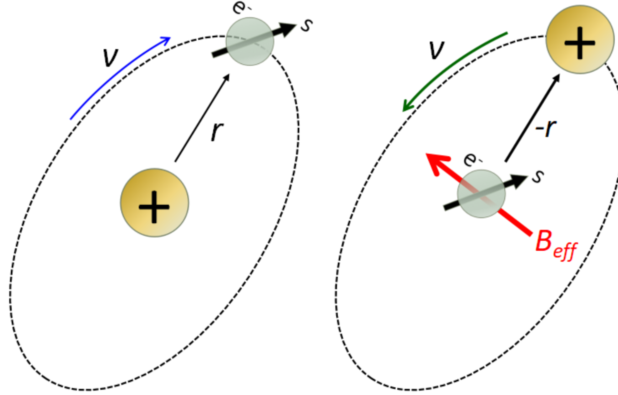

Figure 2.13: Representation of the mechanism behind spin-orbit interaction: in the rest frame of the electron the electric field is seen as an effective magnetic field which couples with the spin.

2.6.1 Spin-orbit interaction

The spin-orbit coupling is a relativistic effect which results, as suggested by the name, in an interaction between the electron spin with its orbital momentum. The origin of this effect can be understood by considering the orbital motion of an electron around the nucleus and analysing it from the rest frame of the electron. As we can see in *figure 2.13*, because of special relativity, the electric field is seen as an effective magnetic field B_{eff} by the electron. This fictitious field, whose orientation depends on the spin direction, couples to the magnetic dipole moment of the electron resulting in the following interaction potential

$$V_{so} = \frac{e}{m_e}(\mathbf{B_{eff}} \cdot \mathbf{s}) \propto \frac{Z^4}{\hbar^2}\mathbf{l} \cdot \mathbf{s} \tag{2.71}$$

where s is the spin angular momentum vector, l the orbital angular momentum and Z the atomic number of the element. It is then clear why spin-orbit interaction has a similar effect on the electron motion as an applied magnetic field. The strength of the coupling depends on the magnitude of the field that the electron feels and therefore is stronger in materials having larger atomic numbers, as we can notice from the Z^4 dependence in V_{so}. The presence of this additional interaction potential in the atomic Hamiltonian leads to a shift in the electron energy levels that lifts the spin-degeneracy and is responsible for the *fine-structure* of the atomic spectra. In a certain sense the effect can be viewed as a Zeeman splitting due to an internal field.
Since the spin-orbit Hamiltonian depends on the product of spin and momentum, the application of the time reversal operator leaves it invariant. Hence, SOI preserves time reversal symmetry (TRS) and, as a consequence, ensures the validity of the *Kramers degeneracy theorem*. According to this theorem, in systems with TRS, for each eigenstate there is always a corresponding time reversed state with the same energy. If the spin degeneracy is broken by spin-orbit coupling, the theorem leads to the following relation:

$$E(\mathbf{k}, \uparrow) = E(-\mathbf{k}, \downarrow). \tag{2.72}$$

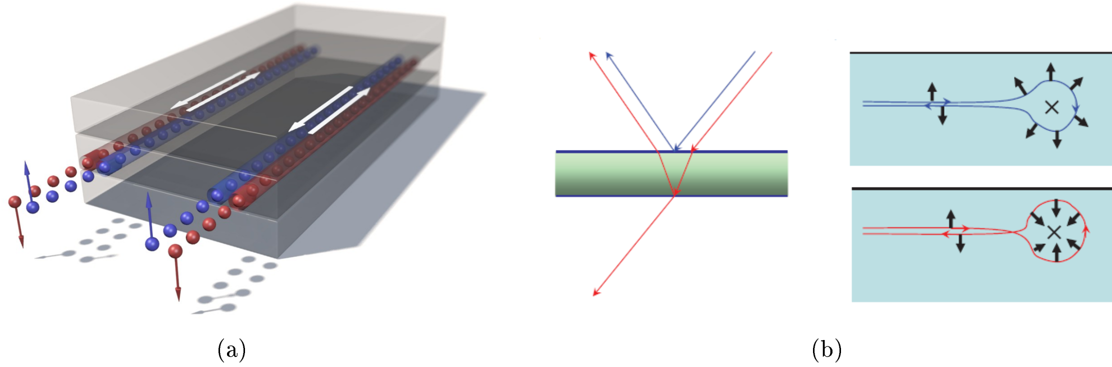

(a) (b)

Figure 2.14: (a) Schematic representation of the spin-polarized helical edge states in a quantum spin Hall insulator. (b) Mechanism behind a lens with anti-reflective coating: light reflected by top and bottom surfaces interferes destructively, leading to suppressed reflection (left). Two possible paths taken by an electron on a QSH edge when scattered by a non-magnetic impurity. The electron spin rotates by π clockwise along the blue curve and counter-clockwise along the red curve. A geometrical phase factor associated with this rotation of the spin leads to destructive interference between the two trajectories (right) [20].

i.e to the existence of at least a pair of degenerate states with opposite spin and momentum, known as *Kramers doublet*. This is exactly the nature of the helical states in spin orbit topological insulators.

2.6.2 Protected helical edge states

In 2D the helical states are basically constituted by two chiral states with opposite spin which counter-propagate at a given edge of the quantum spin Hall insulator, as we can see in *figure 2.14 (a)*. The name "helical" refers precisely to the fact that spin-polarized states propagate in opposite directions, in sharp contrast to the chiral edge states in the quantum Hall state which propagate in one direction only.
Similarly to the chiral states, also the helical states are protected against backscattering and characterized by a quantized conductance. In this case is the presence of time reversal symmetry that ensures the destructive interference between all possible paths taken by the electrons. Backscattering is suppressed in an analogous way as reflections are reduced by the anti-reflective coating which covers most eyeglasses and camera lenses nowadays. As sketched in *figure 2.14 (b)*, in a lens photons reflected from the top and bottom surfaces interfere destructively leading to perfect transmission. Coming back to helical states, when a forward moving electron with spin-up is "reflected" by a non magnetic impurity it can make either a clockwise or a counter-clockwise turn around the scatterer present on the quantum spin Hall edge. Since only spin-down electrons can propagate backward, the electron spin has to rotate adiabatically, either by an angle of π or -π, into the opposite direction (*fig. 2.14 (b)*). Consequently, the two time-reversed paths differ by a full rotation of the electron spin and, since the wavefunction of a spin $1/2$ particle picks up a negative sign under a 2π rotation, they interfere destructively leading to perfect transmission. Different is the situation in case of magnetic impurity, which would break the time reversal

symmetry allowing U-turn scattering processes. This semiclassical argument applies only to the case of a single pair of edge states. If there are two forward and two backward movers on a given edge, an electron can be indeed scattered from a forward-moving to a backward-moving channel without reversing its spin, spoiling the perfect destructive interference described above and leading to dissipation. For that reason, for the quantum spin Hall state to be robust, edge states must consist of an odd number of channels.

2.6.3 Transport of edge states

In the quantum Hall and quantum spin Hall regime the existence of edge states leads to the presence of *non-local transport* that invalidates the Ohm's law. This means that in a multi-terminal configuration a voltage drop could be measured across two probes between which we would not expect a current flown according to the normal diffusive transport. The Landauer-Büttiker formalism is particularly suitable to describe this regime of conduction, as we will show below.

For a general two-dimensional sample, the number of transmission channels scales with the width of the sample, so that the transmission matrix in the Büttiker formula is complicated and non universal. However a big simplification arises if the transport is entirely dominated by edge states.

In the quantum Hall regime chiral edge states are responsible for transport. Since these conducting channels are protected from backscattering, the ith electrode transmits perfectly to the neighbouring $(i+1)$th electrode on one side only. Then for a standard Hall bar with N probes, the transmission matrix elements will be simply

$$\begin{cases} T(QH)_{i+1,i} = 1 & for \;\; i = 1, 2, ..., N \\ 0 & otherwise \end{cases} \tag{2.73}$$

where $N + 1 = 1$ for periodic boundary conditions.

In the quantum spin Hall regime, the helical edge states can be seen as two copies of chiral edge states related by time-reversal symmetry. Therefore, the only non-vanishing matrix elements are given by

$$T(QSH)_{i+1,i} = T(QSH)_{i,i+1} = 1 \tag{2.74}$$

In particular, as we have one channel with spin-up ($\sigma =\uparrow$) and one with spin down ($\sigma =\downarrow$) which propagate in opposite directions, the transmission coefficients from one terminal j to its neighbour i are:

$$\begin{cases} T^{\uparrow}_{ij} = 1 \\ T^{\uparrow}_{ji} = 0 \end{cases} \qquad \begin{cases} T^{\downarrow}_{ij} = 0 \\ T^{\downarrow}_{ji} = 1 \end{cases} \tag{2.75}$$

Recalling the Büttiker formula (2.14), the current at the ith terminal, given by the sum of the currents with spin-up and spin-down, is:

$$I_i \equiv I^{\uparrow}_i + I^{\downarrow}_i = \frac{e^2}{h} \sum_{j \neq i, \sigma} (T^{\sigma}_{ij} V_j - T^{\sigma}_{ji} V_i). \tag{2.76}$$

For a better comprehension of the transport properties of helical states, it is useful to analyse and compare the QHE and the QSHE in the simplest cases of two-terminal and three-terminal configurations.

Two-terminal

As we can see from panel A in *figure 2.15*, in a 2D topological insulator, each side of the horizontal bar has a pair of spin polarized states, one allowing propagation to the left and another allowing propagation to the right. At equilibrium, when both states are equally populated, there is no net charge current. Otherwise, when a potential is applied, the non-equilibrium between the population of states results in a carrier flow. Clearly, a higher chemical potential for the left contact leads to transport to the right and the two states propagating in that direction, situated on opposite sides, are more populated.
From (2.74) and (2.76) it is easy to calculate the expected conductance. The transmission coefficients, in case of two-terminal geometry, are simply

$$T_{12}^{\sigma} = T_{21}^{\sigma} = 1 \tag{2.77}$$

and the current flowing out of terminal 2 is

$$I_2^{\uparrow} = I_2^{\downarrow} = \frac{e^2}{h}(V_1 - V_2). \tag{2.78}$$

If we have a difference of potential V between the two terminals, the conductance is

$$G = G^{\uparrow} + G^{\downarrow} = 2\frac{e^2}{h} \tag{2.79}$$

since there are two conducting channels from the left to the right.
We would have obtained the same conductance in analogous system in the quantum hall regime in presence of two chiral edge states ($\nu = 2$). The only difference is that in this case, the two edge channels which transport current are on the same side of the sample, as we can notice in panel B.

Three-terminal

A difference between the two regimes can be highlighted in a three terminal configuration with one contact playing the role of a voltage probe.
Let's consider first the simpler case of a quantum Hall state with $\nu = 2$, depicted in panel D. Recalling the (2.15) and considering (2.73) we have:

$$\begin{pmatrix} I_{left} \\ I_{probe} \\ I_{right} \end{pmatrix} = 2\frac{e^2}{h} \begin{pmatrix} 1 & 0 & -1 \\ -1 & 1 & 0 \\ 0 & -1 & 1 \end{pmatrix} \begin{pmatrix} V_{left} \\ V_{probe} \\ V_{right} \end{pmatrix} \tag{2.80}$$

At the voltage probe the net charge current vanishes due to the equilibration of the chemical potentials: electrons that leave the contact are replaced by electrons from the reservoir. In the

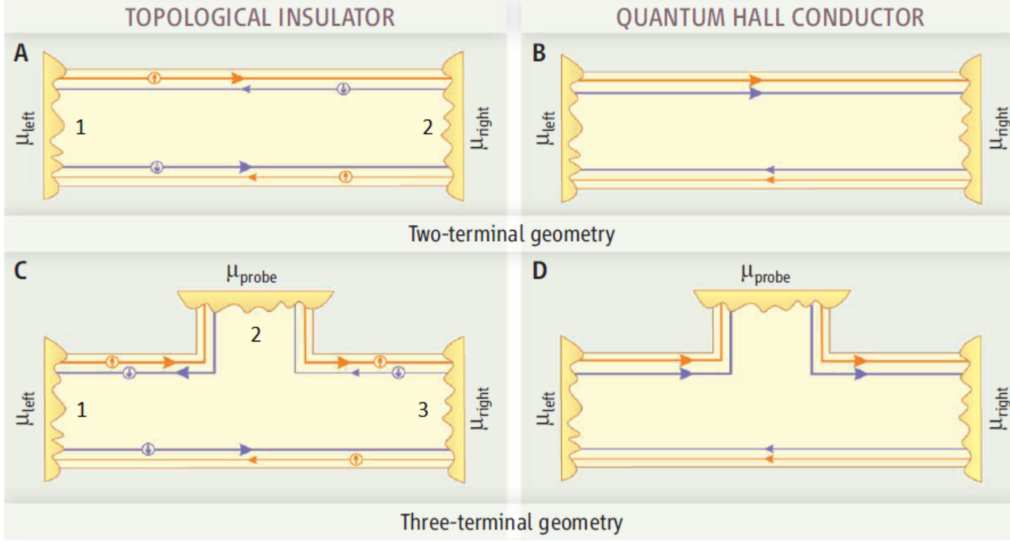

Figure 2.15: Edge states in a 2D topological insulator (A and C) and in a quantum Hall conductor (B and D). In all the examples, the higher chemical potential for the left contact leads to transport to the right. The higher occupancy of states is pictured with thicker lines. Adding a voltage probe has no effect for the quantum Hall conductor, but for the topological insulator, a current flows back from the probe to the left contact, cutting the overall conductance by half a conductance quantum [60].

quantum Hall state, in particular, two edge states from the left source contact enter the voltage probe and two edge states leave the probe directed to the right drain contact.

$$I_{probe} = 2\frac{e^2}{h}(V_{probe} - V_{left}) = 0 \tag{2.81}$$

Then, the potential of the probe is equal to that of the source and the current in the right contact is

$$I_{right} = 2\frac{e^2}{h}(V_{right} - V_{probe}) = 2\frac{e^2}{h}(V_{right} - V_{left}) \tag{2.82}$$

and the conductance has the expected value:

$$G_{QHE} = 2\frac{e^2}{h}. \tag{2.83}$$

The situation is very different for a topological insulator. From (2.15) and (2.75) we have

$$\begin{pmatrix} I_{left} \\ I_{probe} \\ I_{right} \end{pmatrix} = \frac{e^2}{h} \begin{pmatrix} 2 & -1 & -1 \\ -1 & 2 & -1 \\ -1 & -1 & 2 \end{pmatrix} \begin{pmatrix} V_{left} \\ V_{probe} \\ V_{right} \end{pmatrix} \tag{2.84}$$

and the equilibrium condition at the probe becomes:

$$I_{probe} = \frac{e^2}{h}(2V_{probe} - V_{left} - V_{right}) = 0 \tag{2.85}$$

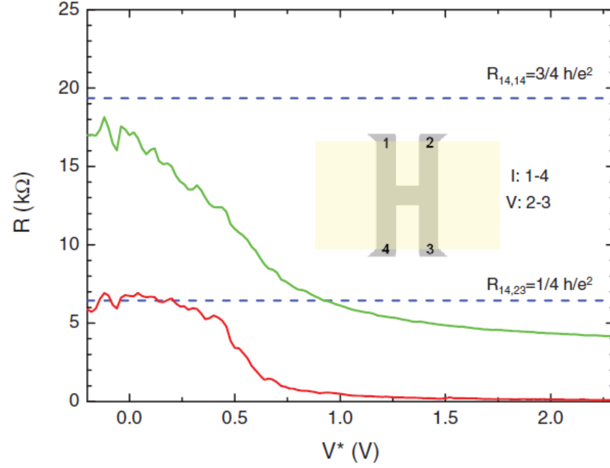

Figure 2.16: Non-local four-terminal resistance (red) and two-terminal resistance (green) measured on an H-bar device; the dotted blue line represents the theoretically expected resistance [61].

In this case, as we can see from panel C, only one edge state is directed from the source to the probe, while two other edge states leave the probes directed one to the source and one to the drain. The probe potential is then tuned halfway between the potentials of the left and right contacts, so that half current is directed back to the source and the condition of zero current is maintained:

$$I_{right} = \frac{e^2}{h}(2V_{right} - V_{left} - V_{probe}) = \frac{3}{2}\frac{e^2}{h}(V_{right} - V_{left}). \tag{2.86}$$

Thus the value conductance results to be affected by the voltage probe

$$G_{QSHE} = \frac{2}{3}\frac{e^2}{h} \tag{2.87}$$

and in particular reduced by $e^2/2h$.
In the topological insulator, a voltage probe that maintains zero current provides momentum relaxation because it forces half the carrier back against their direction of incidence. Then the conductance value depends on the number of the voltage probes the current has to pass through. This it might seem in contradiction with the dissipationless nature of the helical states. However it has to be considered that a voltage lead constitutes a reservoir containing infinitely degrees of freedom and the time reversal symmetry is effectively broken by the macroscopic irreversibility. The dissipation is due to the thermalization processes at the interface with the lead, which equilibrate the chemical potentials and destroy the phase coherence of wave functions. While the latter is a necessary condition for the validity of Kramers theorem and then for the existence of helical states, it is not required instead for chiral edge states that are topologically protected [61]. This is the reason why the conductance in the quantum Hall state is independent by the number of voltage probes in the current path.

Non-local measurements

In the previous paragraphs we have seen how is possible to detect the QSHE by means of transport measurements in a multi-terminal configuration. The most common way to prove the existence of helical edge states uses non-local voltage measurements. Considering a device like the one sketched in *figure 2.16*, two terminals act as current probes and the other two as voltage probes. The non-local resistance is defined as:

$$R_{ij,kl} = \frac{V_k - V_l}{I_{ij}}. \tag{2.88}$$

Using terminals 1 and 4 as current sources and contacts 2 and 3 as voltage probes we have the stationary conditions

$$\begin{cases} I_1 = -I_4 \\ I_2 = I_3 = 0 \end{cases} \tag{2.89}$$

with which the system of equations given by the Büttiker formula can be solved.
Hence, the expected values for the two-terminal resistance $R_{14,14}$ and the non-local $R_{14,23}$ resistance in presence of helical edge states are:

$$\begin{aligned} R_{14,14} &= \frac{V_1 - V_4}{I_1} = \frac{3}{4}\frac{h}{e^2} \\ R_{14,23} &= \frac{V_2 - V_3}{I_1} = \frac{1}{4}\frac{h}{e^2}. \end{aligned} \tag{2.90}$$

As we can see in the graph in *figure 2.16*, these values have been experimentally confirmed in HgTe/CdTe quantum wells, giving a strong proof of the existence of the quantum spin Hall state.

Chapter 3

WTe_2: from bulk to thin layers

Transition metal dichalcogenides are characterized by a layered structure which allows an easy *micro-mechanical exfoliation* down to atomic thickness. That opens up the possibility to study how the electronic properties of the materials are tuned changing the number of layers considered. In this respect, the behaviour of WTe_2 is particularly interesting: while the bulk shows extremely large magnetoresistance and high mobilities, below six layers the material behaves as in insulator. The metal-insulator transition is due to the an oxidation of the surface which can be prevented encapsulating the material between layers of inert compounds. With suitable van der Waals heterostructures, whose details are described in the next chapter, is then possible to observe the intrinsic properties of few layers material. Especially relevant is the monolayer form that has been predicted to be a 2D topological insulator in presence of strain.
In this chapter we will give an overview of the main properties of WTe_2 scaling from bulk to thin layers, on which our work is particularly addressed.

3.1 A compensated semimetal

As the others transition metal dichalcogenides, WTe_2 is constituted by a stack of three atom-thick layers, each of which is constituted by a plane of Tungsten atoms sandwiched between two Tellurium planes. Differently from most of the TMDs which crystallize in the 1H structure, in monolayer WTe_2 the hexagonally packed atoms are arranged in an ABC stacking. However, due to the instability of 1T phase in free-standing form, the structure undergoes a spontaneous lattice distortion into the 1T' phase (*fig. 3.1*). As we can see in column C, the periodicity in the x direction is doubled and the W atoms form a zig-zag one dimensional chain along the y direction.
Electronic structure calculations show WTe_2 to be a nearly perfect compensated semimetal, which means that the density of electrons and hole are approximately the same (*fig. 3.2 (a)*). In particular, as we can notice in *figure 3.2 (b)*, the Fermi surface is composed of two sets of electron and hole pockets splitted by spin-orbit coupling.
This hole-electron "resonance" condition is supposed to be at the origin of the extremely large magnetoresistance (MR) observed in bulk crystals of WTe_2. Ordinary magnetoresistance, which has been defined in *chapter 2*, is usually a relatively weak effect, commonly found in non-

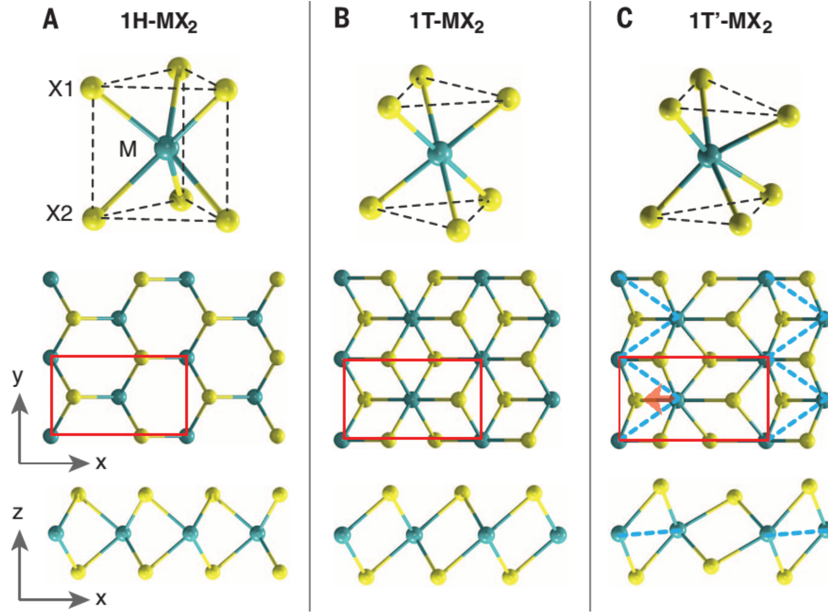

Figure 3.1: Atomic structures of monolayer transition metal dichalcogenides MX_2. (A) $1H$ in ABA stacking, (B) $1T$ in ABC stacking, (C) $1T'$ distorted structure. The unit cell is indicated by red rectangles [37].

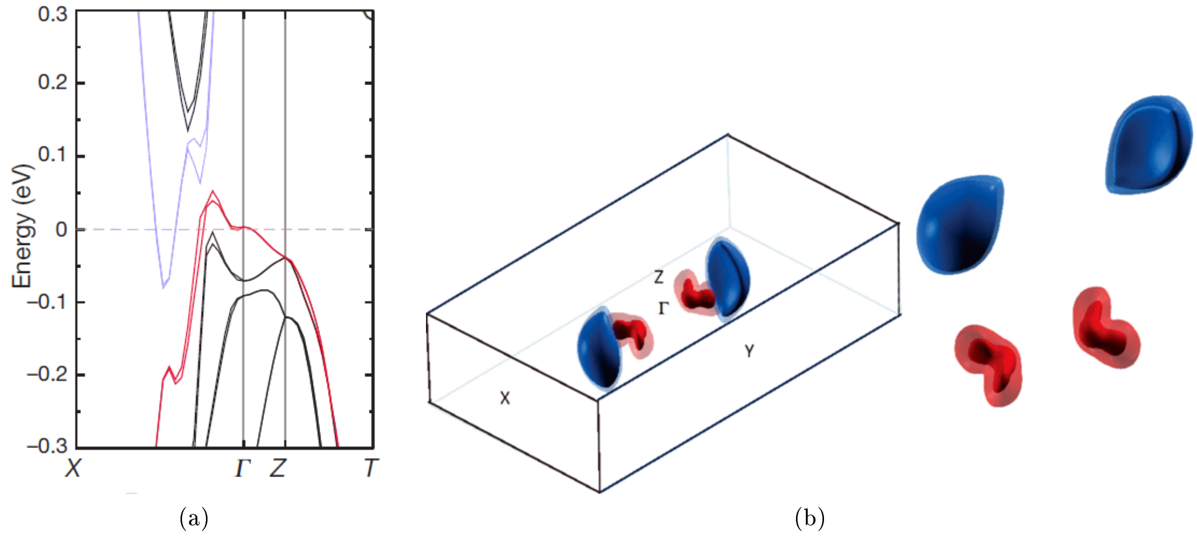

(a) (b)

Figure 3.2: (a) The electronic structure of WTe_2 in $\Gamma - X$ and $\Gamma - Z$ directions calculated including spin-orbit coupling [35]. (b) Fermi surface of WTe_2: the spin-orbit split electron pockets are shown in blue and in light blue colour, while hole pockets in red and in pink. [62].

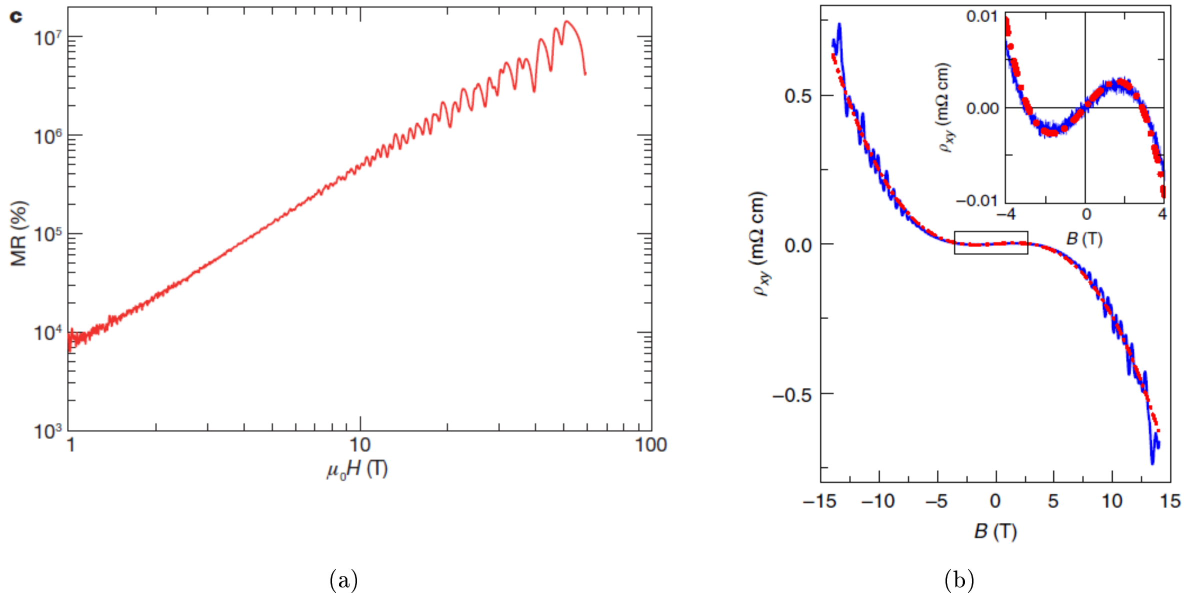

(a) (b)

Figure 3.3: (a) Magnetoresistance of bulk WTe_2 up to 60 T at 0.53 K, with the current parallel to y and the magnetic field along z [35]. (b) Transverse resistivity as a function of the magnetic field; the inset shows the peculiar behaviour predicted by equation (2.44) for $n > p$ and $\mu_p > \mu_n$ [38].

magnetic materials and with values of few percent for metals. In WTe_2 instead, when the current direction is along the tungsten chains and the magnetic field is applied perpendicular to the layers, MR reaches a value of 13 million percent at 0.53K and 60 T, without any signs of saturation (*fig 3.3 (a)*). The quadratic dependence of the magnetoresistance from the field is predicted by a classical two bands model for semimetals in case of nearly perfect compensation between electron and hole density ($n \sim p$), as we have seen in (2.45) and (2.46).
From the graph in *figure 3.3 (b)* and *figure 3.4 (a)* we can notice that the model quantitatively reproduces both the transverse resistivity and the magnetoresistance measured in the bulk, as we will see in more details in *chapter 5*. The agreement between theory and data is particularly remarkable for ρ_{xy}, where the fitting even predicts correctly the change in sign of the resistivity at small magnetic fields in accordance with equation (2.44) for particular values of the parameters n, p, μ_n and μ_h. In addition, Shubnikov-de Haas oscillations are clearly visible for B≥3T, confirming the high mobility of the carriers in the bulk. The analysis of the oscillations is particularly important to determine the values of densities and mobilities of electrons and holes. The Fourier spectrum shows four independent frequencies, visible in the inset in *figure 3.4 (b)*, which are attributed to the different electron-hole pockets. Assuming that the Fermi surface is approximately ellipsoidal, from the *Onsager relation* we can find the Fermi momentum k_F

$$F = \frac{hk_F^2}{4\pi e} \tag{3.1}$$

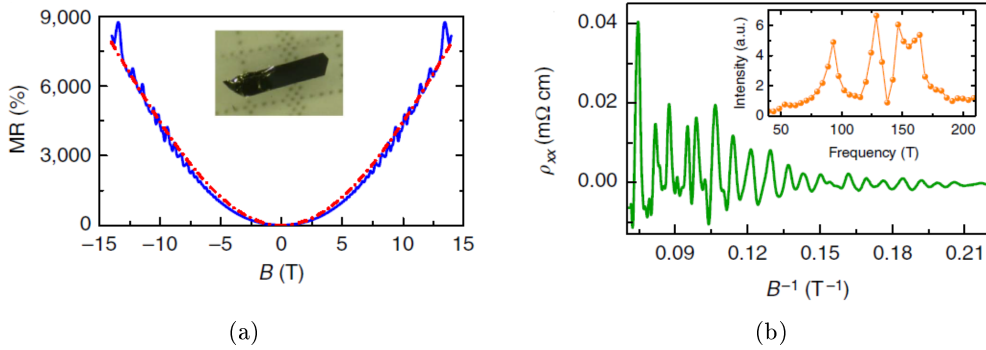

Figure 3.4: (a) Non-saturating, quadratic field dependence of the MR; the blue line represents the experimental data and the red dashed-dotted line the theoretical fit. The inset shows an optical image of a bulk crystal; the scale of the graded paper is 1x1 mm. (b) SdH oscillations obtained by subtracting the quadratic background from the longitudinal resistivity, plotted as a function of B^{-1}; the frequency spectrum in the inset, highlights four dominant peaks [38].

that is related to the density by the *Luttinger's theorem*

$$n = \frac{k_F^3}{6\pi^2}. \tag{3.2}$$

The value of the magnetic field at which SdH appear fixes instead the mobility of one type of the carriers while the other one can be estimated from the magnitude of the quadratic MR:

$$\begin{cases} \mu B \sim 1 \\ \frac{\Delta\rho}{\rho} = \mu_e \mu_h B^2. \end{cases} \tag{3.3}$$

Determining which type of charge carriers has one or the other mobility requires the full data analysis. For a bulk crystal, like that shown in the inset of *figure 3.4 (a)*, with thickness on the millimetre scale, both electron and hole mobilities are rather large ($5\,000 \div 10\,000$ cm^2 V^{-1} s^{-1}), as we can notice in *figure 3.5 (b)*.

3.2 Thickness evolution of magnetotransport

WTe_2 continues to behave as a compensated semimetal down to six layers thickness: the MR always exhibits a B^2 dependence while the transverse resistance varies consistently with the values of the relative magnitude of n p μ_e and μ_h according to (2.44). The classical two-bands model then gives a very accurate description of the trends regardless of the precise details of the material band structure, which on the energy scale of the band overlap - few tens of meV - is certainly different for the bulk and for atomic thick crystals. This insensitivity to details is very likely the reason why a two-band model works so well, despite the presence of more bands. Anyway since electrons (and holes) in different bands have essentially the same mobility is reasonable to expect that classical transport is only sensitive to their total density.

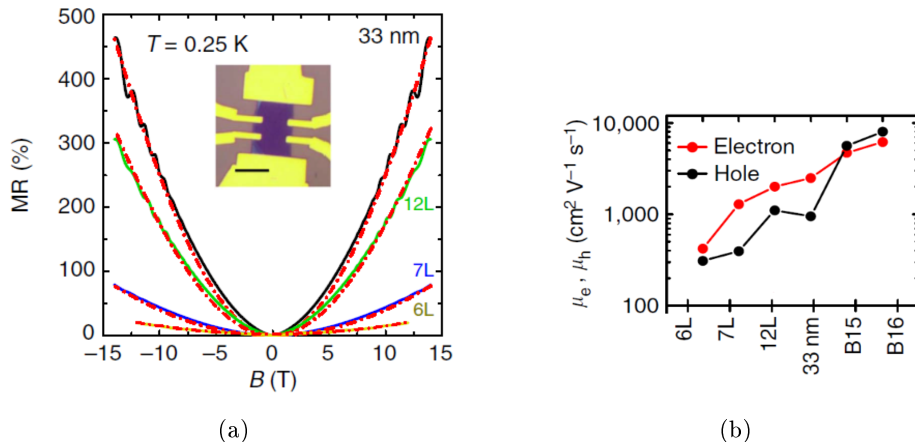

Figure 3.5: Evolution of magnetotransport from bulk (samples B15 and B16) to six layers crystals. (a) Longitudinal magnetoresistance for exfoliated crystals of different thickness; the inset shows an optical image of a seven layers device (scale bar, 5 mm). (b) Electron and hole mobility extracted from fitting the data [38].

Even if the magnetoresistance shows a quadratic dependence, its magnitude is very significantly suppressed, as we can notice in *figure 3.5 (a)*. That is mainly due to the large drop in carrier mobility which decreases by two order of magnitudes going from bulk to six layers samples (*fig 3.5 (b)*). When the crystal thickness becomes smaller than the mean free path, the scattering at the surface starts indeed to play an important role. This observation suggests that, although having comparable density of electrons and holes is important, it is the high mobility of the two carriers that is essential to achieve the very large MR measured in WTe_2.
As the thickness of the crystals is decreased even further to approach the ultimate limit of individual monolayers, the mobility continues to decrease and a metal-insulator transition occurs; the crossover is clearly visible in the temperature dependence of the *square conductance* $G_\square$ in *figure 3.6 (a)*. This quantity, which is the reciprocal of the *sheet resistance* R_s, is very useful to study thin films that are nominally uniform in thickness and can be considered as two-dimensional entities. R_s is connected to the resistance in a three-dimensional conductor by the following relationship

$$R = \frac{\rho}{t}\frac{L}{W} = R_s\frac{L}{W} \tag{3.4}$$

where L is the length of the conductor W is width and t is the thickness.
The insulating behaviour highlighted in the graph, which becomes progressively more pronounced for tri and bilayers (3L, 2L), sets in only at relatively low temperature so that, whereas at 300 K the resistivity increases by only a factor of five when comparing bulk crystals and bilayers, the increase is as large as five orders of magnitude at 250 mK. As we can notice in *figure 3.6 (b)*, the conductance in tri-layer WTe_2 depends monotonically by the gate. That means that the insulating state is not due to the formation of a gap in the band structure, but rather by an increase of disorder. In particular the occurrence of a metal-insulator transition at a conductivity per layer of e^2/h strongly suggests that carriers in very thin WTe_2 layers are Anderson localized.

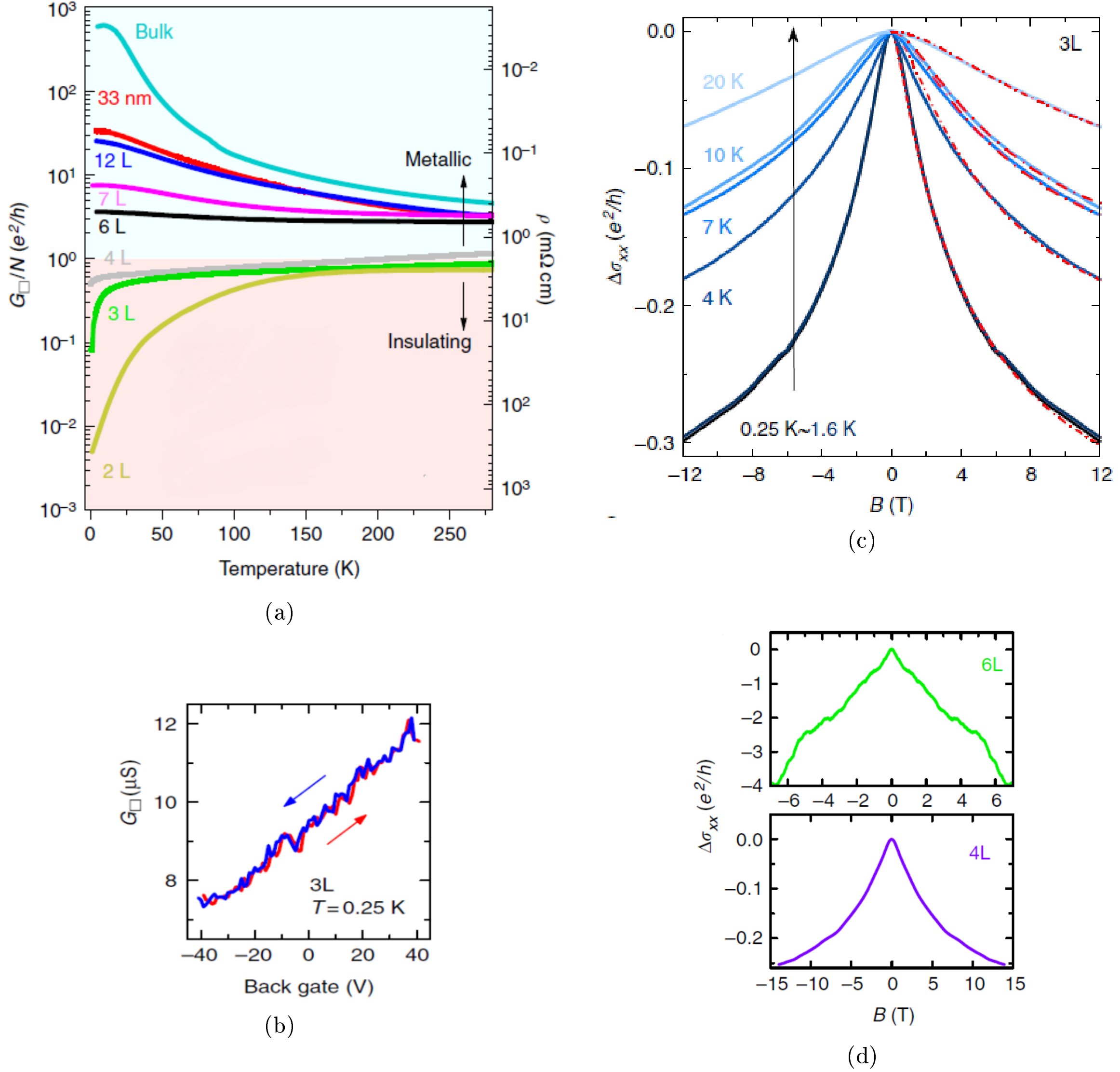

Figure 3.6: Metal–insulator transition in atomically thin WTe_2. (a) Temperature dependence of the conductance per square normalized to the number of layers, measured in crystals of different thickness. (b) Square conductance of a trilayer as a function of gate voltage; the red and blue curves correspond to data taken on sweeping the gate voltage in opposite directions and illustrate the reproducibility of the measurements. (c) Magnetoconductance of a trilayer device showing a decrease of the effect with increasing temperature, as expected for quantum interference effects; the experimental data are fitted with the theory for WAL. (d) Magnetoconductance of crystals of different thickness [38].

This hypothesis is confirmed by magnetotransport measurements in crystals below 10 layers thickness, which show signature of weak anti-localization, a quantum interference effect that,

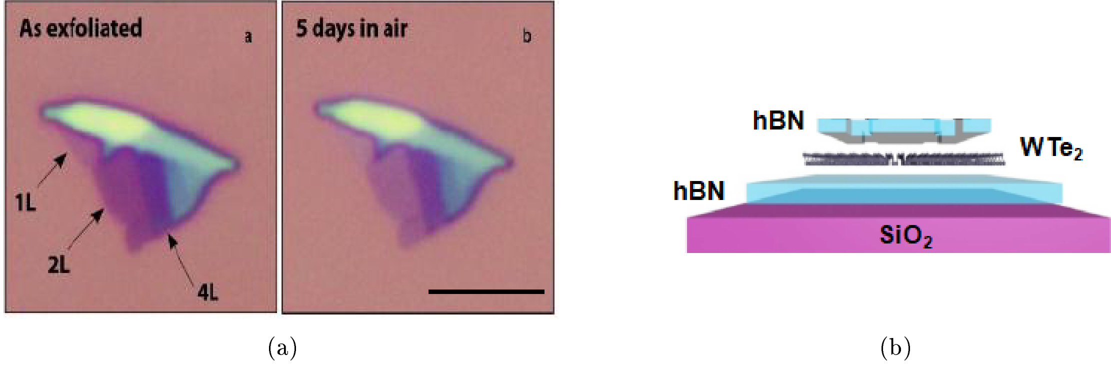

(a)

(b)

Figure 3.7: (a) Oxidation of WTe_2 under ambient conditions (scale bar 5 μm) [38]. (b) Schematic representation of the van der Waals heterostructure used to encapsulate thin layers WTe_2.

as already told in the previous chapter, emerges in low mobility sample characterized by strong spin-orbit coupling. From the plot in *figure 3.6 (c)* we can see the good agreement between the quantum corrections to the conductivity obtained experimentally and the predictions of the Hikami–Larkin–Nagaoka theory for WAL. Despite the precise nature of the spin–orbit interaction in WTe_2 is not clear, the data are fitted using expression (2.31) keeping B_{so} constant and allowing B_ϕ to vary as a function of temperature, coherently with the fact is inversely proportional to the phase-coherent time. Looking at *figure 3.6 (d)* we can notice that the relative strength of the effect increases as the layer thickness is decreased. This is reasonable because the magnitude of the WAL correction on the conductivity is always e^2/h, whereas the classical contribution decreases on thinning down the material. Also the magnetic field range in which weak anti-localization is visible becomes larger with decreasing thickness, as expected since thinner flakes have smaller mobility and hence shorter electronic mean free path.
Thus in thin layers crystals quantum interference effects dominate the transport and are responsible for the insulating behaviour. The origin of this disorder-induced localization is related to the non-perfect chemical stability of WTe_2 in presence of humidity, which leads to the oxidation of the outermost layers. As we can see in *figure 3.7 (a)*, a change in the optical contrast is clearly visible after some days of exposition to air; in addition to this, the degradation of the surface is confirmed by other experimental techniques like *X-ray photoelectron spectroscopy* (XPS) and *Auger electron spectroscopy* (AES) [63].
A solution to preserve the crystal quality is given by the possibility of encapsulate it between layers of inert compounds, as boron nitride, stacking different materials in a van der Waals heterostructure as the one depicted in *figure 3.7 (b)*. The encapsulation enables the study of the transport properties down to monolayer crystals, which has been the main purpose of the present work.

3.3 Edge states in monolayer T'-WTe_2

According to band structure calculations, strained monolayer WTe_2 is predicted to be a two-dimensional topological insulator. The spontaneous lattice distortion into the 1T' phase induces

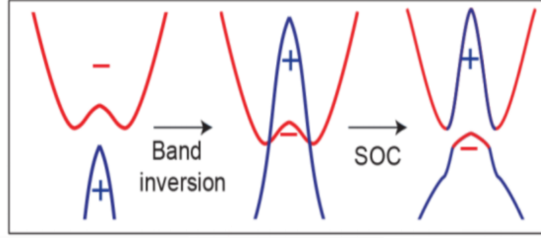

Figure 3.8: Schematic diagram of the bulk band evolution from a topologically trivial to a non-trivial phase, and then to a gap opening due to SOC [36].

indeed an intrinsic bands inversion and the strong spin-orbit coupling breaks the spin degeneracy opening a bulk bandgap, as we can see in *figure 3.8*. These are key elements for a quantum spin Hall state, hypothesis which has recently been reinforced by several experimental results. A gap has been observed with ARPES and STM and edge conduction has been detected by transport measurements.
Focusing on transport, measurements on encapsulated monolayer devices show a non-zero conductance even at low temperature, differently to what was found for non-encapsulated crystals which are insulating due to a disorder-induced localization.
In *figure 3.9* we can see how the two-terminal conductance varies in function of gate voltage for an encapsulated trilayer, bilayer and monolayer.

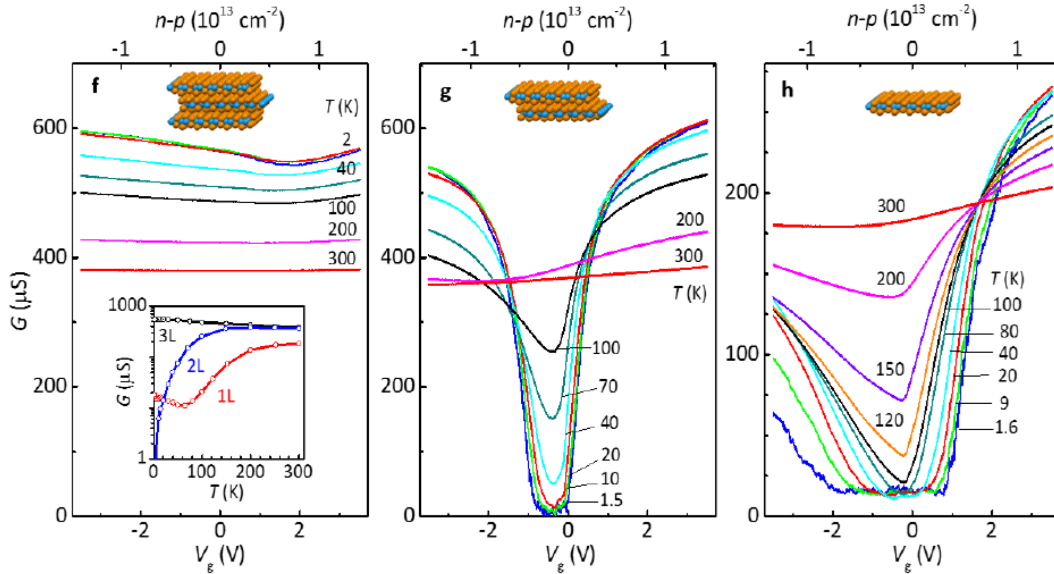

Figure 3.9: Temperature dependence of the conductance for similar contact pairs on a trilayer, bilayer, and monolayer device, respectively. The inset compares the temperature dependence of the conductance minimum in the three cases. [17].

The trilayer has a metallic behaviour with a conductance that increases on cooling down and

saturates at the lowest temperatures, like it happens in the bulk. On the contrary, the bilayer shows a strong gate dependence with a sharp minimum near $V_g = 0$, suggesting the presence of a bandgap. A similar gate tunability is observed in the monolayers, with the difference that below 100 K the minimum stops dropping and instead broadens into a plateau of conductance, on which there are mesoscopic fluctuations. This observation is consistent with the prediction of bandgap opening in monolayers crystals and despite the measured edge conductance could have different origins, some hints strongly connected it with helical edge states [17].
Further experimental proofs of edge conduction has been obtained by non local measurements and by grounding experiments with the purpose of separating the contribution of bulk and edge modes [17]. In particular, as suggested by the conductance trend as a function of gate voltage, the edge current can be isolated by working at low temperature and close to $V_g = 0$. A suppression of the edge conductance with the magnetic field is observed and strengthens the hypothesis of helical states since elastic backscattering is allowed once time reversal symmetry is broken.
The value of the measured edge conductance is about half of e^2/h, not in accordance with the theoretical predictions for helical modes. However, a perfect quantization has never been observed in a quantum spin Hall state and that is one of the reason why this state of matter is still not completely understood.
In the last chapter we will see how our measurements are consistent with these experimental results, giving an additional proof of the presence of edge current in encapsulated monolayer WTe_2.

Chapter 4

WTe_2 monolayer devices

The device fabrication constitutes a substantial part of this experimental work. As already mentioned, studying the intrinsic properties of WTe_2 monolayers requires an encapsulation between protective layers of inert material to prevent the crystal degradation. For this reason, preparing a sample suitable for our purpose is absolutely not trivial and has required the development and the optimization of targeted nano-fabrication processes.
The procedure to build the devices requires several steps, starting from *micro-mechanical exfoliation* of crystals and including *electron beam lithography* to pattern the metal contacts. Apart from these conventional nanofabrication processes, in order to assemble van der Waal heterostructures, a non-standard *transfer technique* has been developed, which allows to pick-up and align different atomically thin crystals with micrometric precisions.
In this chapter we will briefly discuss the main experimental techniques employed in the device fabrication, with a particular emphasis on the non-conventional aspects involved in the procedure. Two slightly different heterostructures are proposed: one with WTe_2 monolayers encapsulated between two layers of boron nitride with pre-patterned platinum contacts on the bottom hBN, the other with hBN as bottom layer and monolayer MoS_2 as cover layer with tunnel contacts on top.
Although of rather technical nature, the work described hereafter is part of a rapidly developing area of research, which focuses on the control and understanding of new structures based on the stacking of layers of atomic thickness.

4.1 General aspects of nanofabrication

In the following section we will retrace the basic steps of the device fabrication, in a chronological order, focusing mainly on the distinctive features of our samples.

4.1.1 Substrate preparation

The process to fabricate every type of device for transport measurements starts with the substrates preparation.
A conventional Si/SiO_2 wafer, i.e. highly p-doped silicon covered with a 285 nm layer of ther-

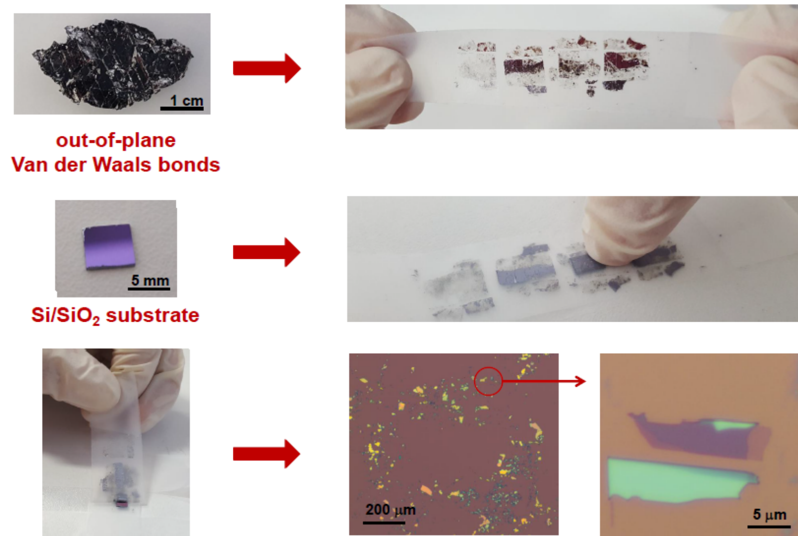

Figure 4.1: Micro-mechanical exfoliation with the scotch tape technique. The images at the bottom right show how the substrate appears in the optical microscope with different magnifications.

mally grown silicon oxide (which ensures a good contrast for the crystals identification and enables electrostatic gating), is cut with a diamond pen in chips approximately of 5x5 mm^2, depicted in *figure 4.1*.
Then, a cleaning protocol process is followed because, in order to have good devices, not only the materials which form the heterostructure itself must be of high quality, but also the chips must be clean and free from defects. Substrates always present impurities which can be originated essentially from organic contaminants or metal particles. To remove metal particles we use a nitric acid bath, after which substrates are rinsed in deionized water. Organic contaminants can be instead eliminated using solvents in an ultrasonic bath: first chips are cleaned in acetone, whose residues are then washed away using isopropanol (IPA).

4.1.2 Micro-mechanical cleaving

Naturally, the very first step to build a heterostructure is to isolate the atomically thin crystals (usually referred as *flakes*) that form the device. Flakes are isolated in different substrates and then stacked over each other using a transfer technique, which will be addressed in details later in this chapter.
The method to isolate the flakes is essentially the same developed by the Nobel prizes Geim and Novoselov to get graphene for the first time [2], known as micro-mechanical cleaving or exfoliation. It consists in the repeated mechanical exfoliation of bulk material[1] using a common adhesive tape. The tape is folded and unfolded several times in order to cleave the crystals into thinner flakes, until the thickness of the material is considered acceptable; looking back-lighting

[1]The bulk materials employed in this experimental work are either commercial or produced by research groups specialized in crystal grown. Boron nitride crystals are grown epitaxially, while WTe_2 and MoS_2 by means of chemical vapour transport.

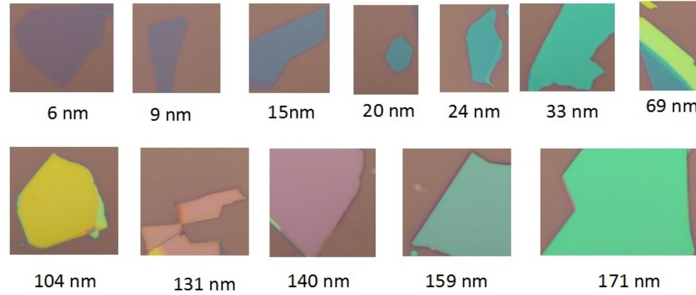

Figure 4.2: Optical images of boron nitrides flakes of different thickness, estimated by AFM analysis.

the scotch can help identifying the areas of the crystal which are more likely to produce the desired flakes. Then, the tape is placed on top of the targeted chip and gently pressed for few minutes in order to allow flakes to stick correctly to the oxide; after that, the scotch is removed carefully to avoid breakage of the crystals adhering to the substrate, as shown in *figure 4.1*. In this seemingly straightforward operation experience plays a key role in finding the optimal conditions to get monolayers crystals.
The procedure is the same for both boron nitride MoS_2 and WTe_2 flakes, even if for the latter is necessary to work under a protective atmosphere to prevent the degradation of the crystal. At this purpose WTe_2 crystals are stored inside a glovesbox, which contains less that one part per million oxygen.
Although the exfoliation technique looks very simple and "old", is so far the most powerful tool to get high quality flakes.

4.1.3 Atomically thin crystals characterization

After the exfoliation, the substrate is inspected under an optical microscope: several pictures are taken with specific illumination and exposure conditions and compared with a database for the thickness identification of flakes. In fact, the optical contrast[2] of thin flakes relative to the substrate evolves systematically with thickness. As we can notice from the boron nitride images collected in *figure 4.2*, different colours correspond to specific thicknesses, whose precise values are obtained by means of *Atomic Force Microscopy* (AFM).
For our purposes, "big" (typical dimensions of few tens of microns at the most) and uniform boron nitride flakes, preferable isolated from the others, are better candidates for a good device. In particular a large area, beside making easier the alignment process during the transfer procedure, ensures a safer encapsulation of the WTe_2. As buildings blocks of a heterostructure, the flakes should also be as flat as possible to avoid local strains and corrugations that lower the electronic quality. A thickness below 40 nm is usually chosen in order to have a higher gate capacitance (especially for the top gate, since the back gate capacitance is mostly determined by the SiO_2 layer).
For mono and bilayers crystals the step heights obtained with AFM cannot be considered com-

[2]The *optical contrast* is defined as $\frac{I_S - I_F}{I_S}$ where I_S and I_F are the intensities of the substrate and the flake in each of the three RGB channels.

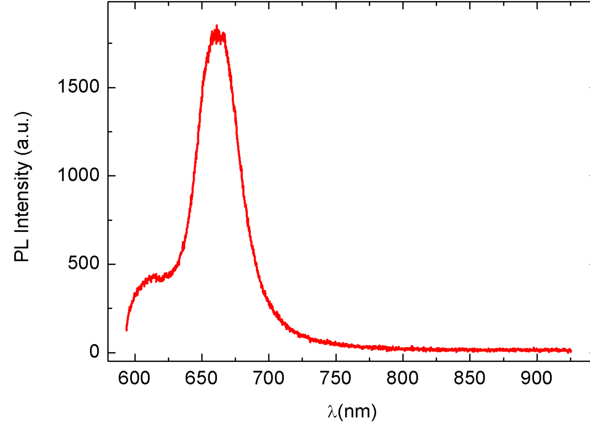

Figure 4.3: Photoluminescence spectrum of a Mo_2 monolayer; the exciton peak is clearly visible for a wavelength of 660 nm.

pletely reliable. An optical analysis with *Photoluminescence* (PL) or *Raman* constitutes a good alternative and is complementary to AFM. In particular PL is suitable to detect TMD materials in which a transition from indirect to direct bandgap semiconductors occurs in the monolayer form. As we can notice in the photoluminescence spectrum in *figure 4.3*, relative to MoS_2, the exciton peak at 660 nm is an unequivocal signature of the monolayer crystal.

Differently from graphene and boron nitride, WTe_2 monolayers can be identified quite easily (without the need of special filters) using an optical microscope; as we can see in *figure 4.4* a monolayer crystal is characterized by a light purplish colour.
A combined analysis of optical results and AFM height profiles of approximately 50 WTe_2 flakes demonstrates that layers exhibiting the same intensity under an optical microscope (i.e having the same thickness) shows reproducibly the same optical contrast and Raman spectra. Among the flakes investigated, the parts with the smallest height relative to the substrate systematically correspond to the region of lowest intensity in optical microscope images (even if the actual step height from the substrate is not exactly the same for different flakes). Since the intensity of monolayers compared to that of the substrate is rather large, thinner layers should have been easily detected if present, so it is possible to conclude that these regions correspond to individual monolayers. Having identified monolayers, the thickness of all other layers can be determined by following the height profile in AFM images, as individual crystalline steps are easily detected in this way. From this analysis, a specific optical contrast in the RGB channels (*fig. 4.4*) and a peculiar Raman spectrum (*fig. 4.5*) can be assigned unequivocally to the corresponding thickness of atomically thin WTe_2 flakes [38].
For the present work we are mostly interested in monolayers crystals, which have to be enough large to allow building a device within an acceptable error tolerance; moreover, due to the high tunability of the material properties with thickness, homogeneity is also particularly important. These requirements are not so easily complied since monolayer crystals tend to break in small pieces and flakes often contain parts of different thickness.

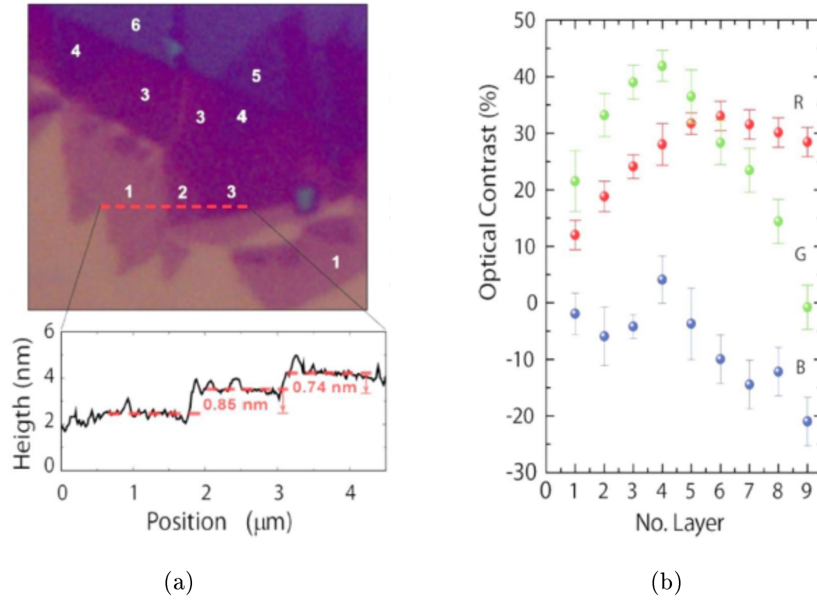

(a)

(b)

Figure 4.4: (a) Optical image and atomic force microscopy of an exfoliated WTe_2 flake containing layers of different thickness (from 1 to 6 monolayers). The AFM profile (the red dashed line indicates the position at which it was recorded) highlights steps corresponding to the expected height of individual WTe_2 monolayers (~ 0.7 nm). (b) Optical contrast measurements required for the attribution of the absolute number of monolayers. The error bars in the R G and B colours channels are the standard deviations obtained from the analysis of all the flakes with the same thickness [38].

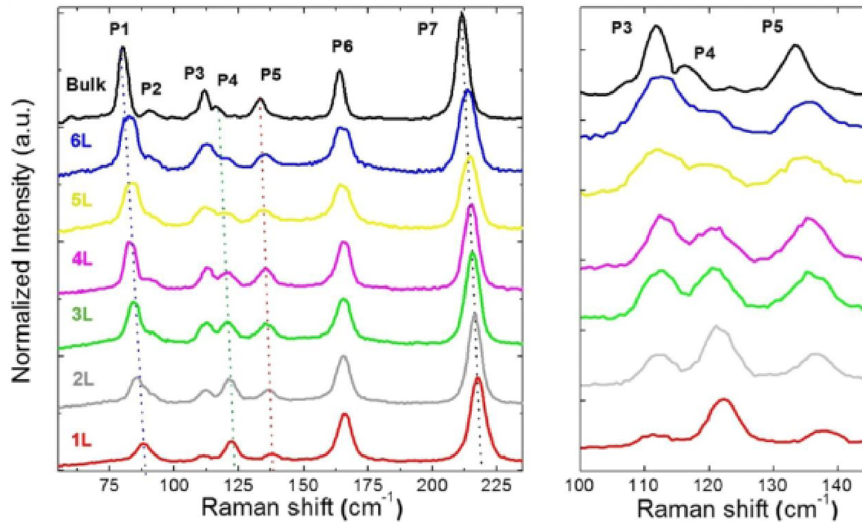

Figure 4.5: Raman spectra of bulk and few-layers WTe_2. Seven peaks, labelled as P1-P7, are observed in the range 50 to 250 cm^{-1} for all thicknesses except for monolayers (peak P2 is missing); the dotted lines put in evidence the shift of the peak positions. The range between 100 and 150 cm^{-1}, which is enlarged on the right, shows the evolution of peaks P3-P5. [38].

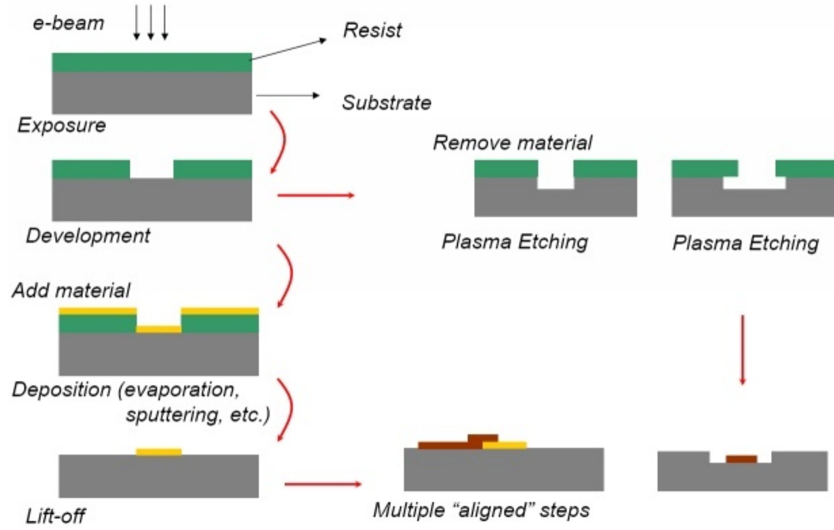

Figure 4.6: Contacts patterning with standard nanofabrication techniques. The mask, defined by lithography, can be used alternatively to deposit metal or to etching structures.

Substrates with suitable hBN or MoS2 flakes are annealed in a constant flow of argon and hydrogen at 400°C for 3-4 hours in order to clean up the surface from glue and other residues. WTe_2 substrates are instead stored inside the glovesbox and, to avoid the risk of degradation, have to be encapsulated in the shortest time possible (maximum few days).

4.1.4 Metal contacts

In order to study transport properties of materials, metal contacts have to be defined on the flake under investigation. This is done with state-of-the-art nanofabrication techniques: first contacts are patterned on a resits by means of electron beam lithography (EBL) and development in a chemical solution, then metal is deposited using an electron beam evaporation (EBE) and removed by lift-off. A scheme of the basic sequential operations, which will be addressed in more detail below, is shown in *figure 4.6*.
For WTe_2 monolayers devices encapsulated between boron nitride two steps lithography and evaporation are required: first the finest contacts are deposited on suitable hBN flakes, then, once the heterostructure is assembled, the coarser structures and the gate are added. To minimize strain in the device and reduce WTe_2 bending, only few nanometers of metal are deposited in the first metal deposition.
The alternative choice of using tunnel contacts on MoS_2 is particularly advantageous in term of fabrication: besides simplifying the alignment during the transfer procedure, it allows to define and deposit contacts all at once.

Electron beam lithography

Electron beam lithography employs a strongly collimated electron beam to draw custom shapes on a surface covered with an electron-sensitive film, known as resist. The e-beam breaks the polymer chains of the resist increasing its solubility respect to the "normal" pre-exposed state so that, when we immerse the sample in a chemical developer, the exposed zones are dissolved, while the unexposed area constitutes a mask for the subsequent metal deposition or etching.
We use a high resolution positive resist, called *polymethylmethacrylat* (PMMA), which has a different electron sensitivity depending on its molecular weight (e.g. 50K and 950 K). Two layers PMMA are *spin coated*[3] on the substrate and baked for some minutes above the glass transition temperature of the polymer (at about 170°C): more specifically PMMA 50K is put at the bottom and 950K on top. Having a bi-layer resist with the bottom layer more electron sensitive than the top layer enables, upon development, the formation of the *undercut* in the patterned path, visible in *figure 4.7 (a)*. This facilitates the subsequent *lift-off*, i.e. the removal of the unexposed regions of resist covered with metal.

Thought EBL is a very sophisticate instrument, its working principles is not very complicated. Electrons are generated by a filament through field effect emission and forced to pass between a series of collimators (electrostatic and magnetic lenses), which reduce as much as possible the aberrations and the dispersion of the beam before it is conveyed on the sample. Since the sample is much bigger than the maximum length at which the beam can be deflected without any aberration, just one small square area (called *write field*) of about 0.5 mm^2 can be exposed time by time. Once a write field area has been exposed, the stage which hosts the sample moves apart to expose the successive write field to the electron beam, and so on until the whole sample has been covered. The stage can move with a precision of the order of few nanometers thanks to a laser interferometer mounted on it. The whole chamber is in high vacuum in order to avoid the scattering of the electrons from charged particles.
Electron beam lithography resolution, which can reach 10 nm, is just limited by the *proximity effect*, i.e. the exposure of adjacent zones of the PMMA due to secondary electrons scattered by the underneath SiO_2. Although EBL goes beyond photolithography in terms of resolution (which in UV lithography is related to the wavelength of the light employed) the complex equipment and the slow exposure times makes it impractical as a mass production micro-manufacturing method.

Before the contacts definition, a preliminary step of EBL is necessary to write a *markers* mask on the substrate, used as a reference to align with sufficient precision the contacts design (made with a software CAD) and the sample surface. The design geometry, related to the specific purpose of the experiment, has to be adapted to the peculiar features of the selected flake. As a general rule, contacts are positioned preferable on clean and flat areas and attention is paid also in avoiding bubbles which can be present in the heterostructure. Previous works on graphene indeed suggest that these bubbles, probably due to local strains, could be correlated with a significant reduction of the electron mobility. In addition, it is advisable to increase the contacts width, approaching the end of the chip, in order to make them more robust when a

[3] *Spin-coating* is a procedure to deposit uniform thin film on a substrate: a small amount of coating material (e.g PMMA) is applied on the center of the substrate, which is rotated at high settable speed in order to spread the coating material by centrifugal force.

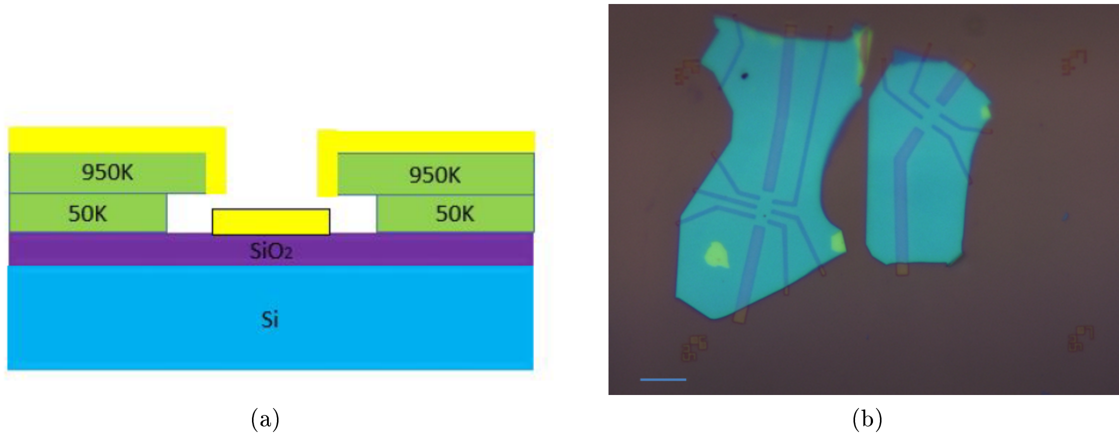

(a) (b)

Figure 4.7: (a) Sketch of the section of a sample after development and metal deposition; the undercut facilitates the subsequent lift-off. (b) Boron nitride flakes with platinum contacts in a Hall bar geometry; the markers used for the design alignment are also visible (scale bar 5 μm).

high precision is not required and to facilitate the subsequent bonding of the sample to the chip carrier. While the finest contacts, close to the flake, are less than 1 μm wide, the coarse structures far away from the heterostructure are usually 25 μm wide.
As already mentioned, for WTe_2 monolayers devices encapsulated in boron nitride, a first step lithography (without taking in consideration the preliminary writing of markers) defines contacts on hBN flakes considered suitable as bottom layers, like the ones shown in *figure 4.7 (b)*. Probes in a Hall bar geometry with various dimensions (from 5x2 μm^2 to 8x4 μm^2 approximately) are patterned in advance in order to have higher chances of compatibility with an exfoliated WTe_2 monolayer. This choice might seem not reasonable, but it should be taken in consideration that working with an air-sensitive material requires a strict observance of the time scales (defining custom contacts after the exfoliation of WTe_2 monolayer would increase too much the risk of material degradation).

Development, contact deposition and lift-off

After the lithography, the sample is developed for a fixed amount of time[4] in a solution of *Methyl Isobutyl Ketone* (MIBK) and IPA (MIBK:IPA=1:3), which removes the resist from the exposed paths (*fig. 4.8 (a)*). Since sometimes the developer MIBK leads to unwanted cracks on the PMMA over the hBN flakes, the development at 0°C in a solution of IPA and water ($H_2$0:IPA=1:3) constitutes a safer alternative.

Once that patterns are “revealed”, the sample is ready for the contacts deposition, realized using an electron beam evaporator that allows to deposit controllable thickness (with nanometric precision) of different materials.

[4]The development times vary depending on the *dose* (charge/area) used for patterning a specific structure with EBL, on the chemical developer, and also on the crystals on which contacts are defined. Usually samples are developed for some seconds, checking if necessary at the microscope how the structures evolve with time.

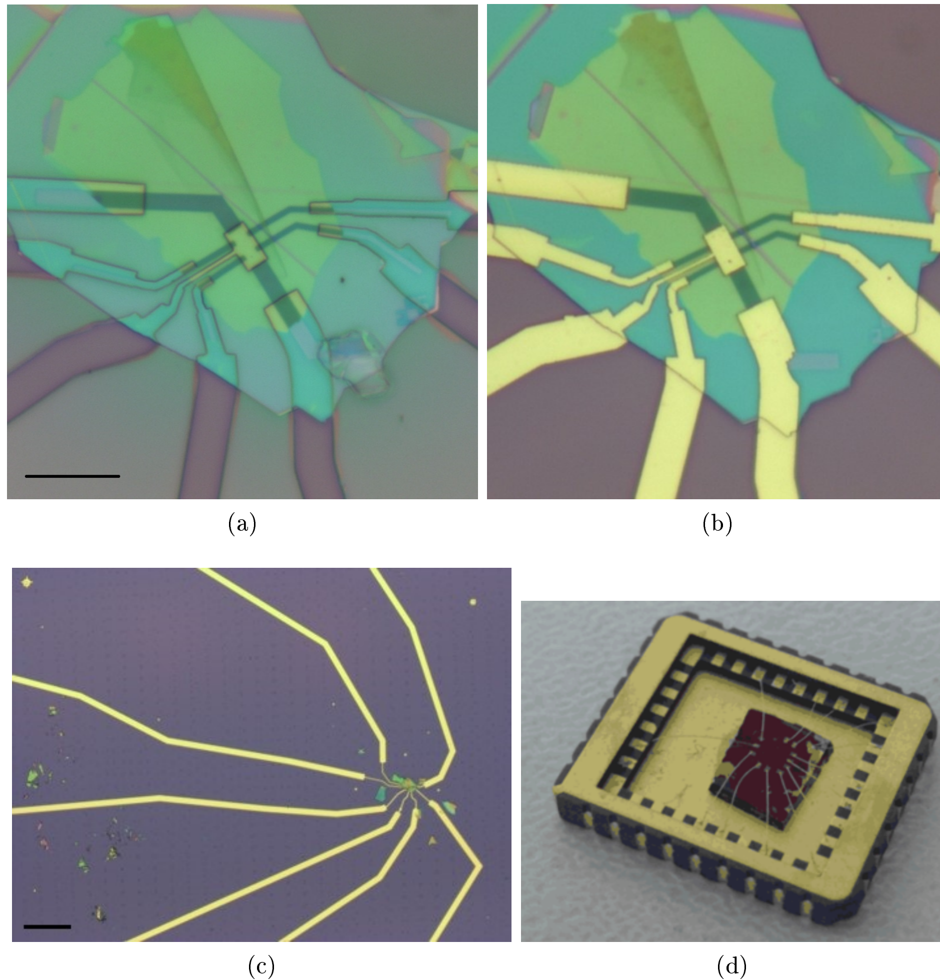

Figure 4.8: Optical images of the device after the development (a) and the contact deposition with the highest (scale bar 10 µm) (b) and the lowest (scale bar 200 µm) (c) magnification. (d) Sample bonded to a conventional chip carrier with gold wires and epoxy glue.

The EBE consists in a chamber, constantly pumped to keep high vacuum (10^{-8} torr), where a target crucible is bombarded with electrons and melted; the evaporated metal condenses on the surface of the sample which is placed upside down over the crucible. The thickness of the film is controlled by means of a quartz crystals positioned close to the sample holder, whose resonance frequency varies as a function of the amount of material that deposits on it.
For the hall bars on hBN bottom layer flakes we deposit a very thin layer of metal: specifically 2 nm titanium[5] (Ti) and 5 nm platinum (Pt). The first ensures a better adhesion to the substrate, making contacts more robust, while the second is chosen because it is suppose to

[5]Titanium is a *getter*, i.e. it adsorbs impurities from the wall of the chamber, leading to an improvement of the vacuum. For this reason, it is often evaporated in the chamber before other metals deposition to decrease the pressure.

have a good band alignment with monolayer WTe_2. In the second evaporation, in which the coarse structures are patterned, we deposit instead few nanometers Ti and a thicker layer ($\sim$ 70 nm) of gold (*fig. 4.8 (b)* and *(c)*).

After the deposition, the substrate is completely covered by metal but only in the exposed parts, corresponding to the design, metal is actually in contact with the silicon oxide. Elsewhere metal is laying on the resist (*fig 4.7 (a)*) and must be removed by the lift-off. This process consists in immersing the sample in warm acetone for several minutes until the PMMA is dissolved and the unnecessary gold on top of it is removed.

Thermal annealing and bonding

Once contacts are defined, samples are usually thermally annealed to remove the PMMA residues from the surface. After the second evaporation, this is not possible because the annealing could favour the diffusion of oxygen in the encapsulated WTe_2. For this reason, to ensure an effective removal of PMMA and a good quality contact, it is advisable to slightly overdevelop the pattern.

The very last step in the fabrication of the device consists in bonding the sample to the so-called chip carrier, in order to make it suitable for the insertion in the measurement system. The chip carrier, visible in *figure 4.8 (d)*, is nothing but a support for the chip, with standardized dimensions and several pins. All the contacts on the silicon are manually bonded to the chip carrier pins using gold wires and a conductive epoxy glue. If we want to use the SiO as a back gate an extra wire is also added, which connects a pin directly to the base of the substrate.
When the epoxy glue is completely dried (usually it takes some hours) the sample is finally ready to be cooled down and measured.

4.2 Transfer technique

The key step of fabrication of WTe_2 monolayers device consists in assembling the heterostructure, aligning different flakes with micrometric precision.
The transfer technique we employed in the present work, called the "pick-and-lift" method, is based on the strong van der Waals interactions which exist between the crystals. In fact, when a membrane with a 2D crystal on it is put in contact with another 2D crystal and it is then lifted up, there is a chance that the second crystal will stick to the first and will be lifted together with it.
The method relies on the use of a special polymer, the *polypropylene carbonate* (PPC), which becomes softer above the glass transition temperature (~ 40°C), enabling to trap the flakes in its viscous surface.
Before starting the transfer procedure is then important to prepare a glass plate with the polymer, which will be mounted on a micro-mechanical arm, described below. A rectangular piece (few cm^2) of *polydimethylsiloxane* (PDMS), an elastic polymer which ensures mechanical stability, is placed on one side of the glass plate. Then a PPC thin film, previously spun on a silicon substrate, is detached from the chip with the help of a scotch tape and placed on top of PDMS, paying attention to avoid as much as possible the formation of wrinkles. The flatness of the film is anyway improved baking the substrate at ~ 60°C for some minutes.

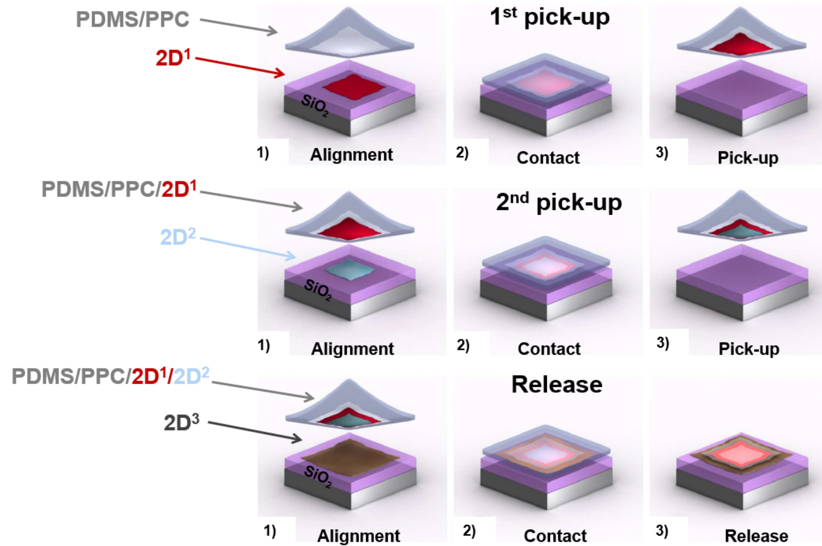

Figure 4.9: Pick-and-lift technique for assembly of van der Waals heterostructures [64].

The role of the temperature is fundamental in the transfer procedure, since it changes the texture of the PPC polymer.
Without caring about the technical issue of the alignment, which will be addressed afterwards, we can understand the basic working principle of this dry[6] transfer technique, looking at the schematic representation in *figure 4.9*. As we can see, an encapsulation requires three distinct steps; the procedure can be generalized to build more complex heterostructures repeating the process several times. In the initial step the PPC polymer is brought gently in contact with the flake we want to pick up and the temperature is raised to $\sim 70°C$ (the transfer set-up is equipped with a heater and a thermometer for the setting and the control of the temperature). Then, we have to wait for the cooling down ($\sim 26°C$ it is enough) and lift the PPC from the substrate; if everything works correctly, the desired flake and also crystals nearby are picked up. The second step is analogous, with the difference that we have to care about the alignment of the first flake already picked up (in our specific case the top boron nitride) and now on the polymer, with the second flake (WTe_2 monolayer) on the substrate. When the two flakes are in contact the temperature is raised again and, after the cooling down, the PPC with the two flakes stack is lifted. The last step, the trickiest in terms of alignment, consists in the release of the two flakes previously picked-up on the bottom boron nitride flake. This is done increasing the temperature to $\sim 110°C$ and lifting the PPC directly, without waiting for the cooling down. In *figure 4.10* we can see how the three steps of the encapsulation appear in the optical microscope. As we can notice in the top right image, relative to the alignment of the stack top-hBN/WTe_2 with Pt contacts on the bottom-hBN, it is very difficult to properly see the edges of the monolayer flake and the probes on hBN beneath it. Contrast enhancement software can help in this delicate alignment task but a proper choice of the thickness of the

[6]The pick-and-lift method is also called dry transfer to distinguish it from the wet transfer, which employs water.

bottom hBN can also be crucial in improving the visibility (hBN flakes with thickness below 30 nm seem to give a better contrast respect to thicker crystals).

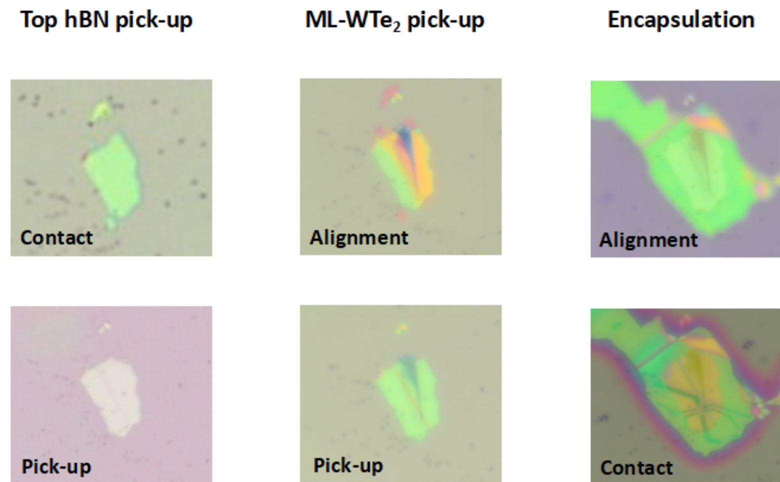

Figure 4.10: Optical images of the flakes during the three steps (corresponding to the three columns) of the transfer procedure.

4.2.1 Transfer set up

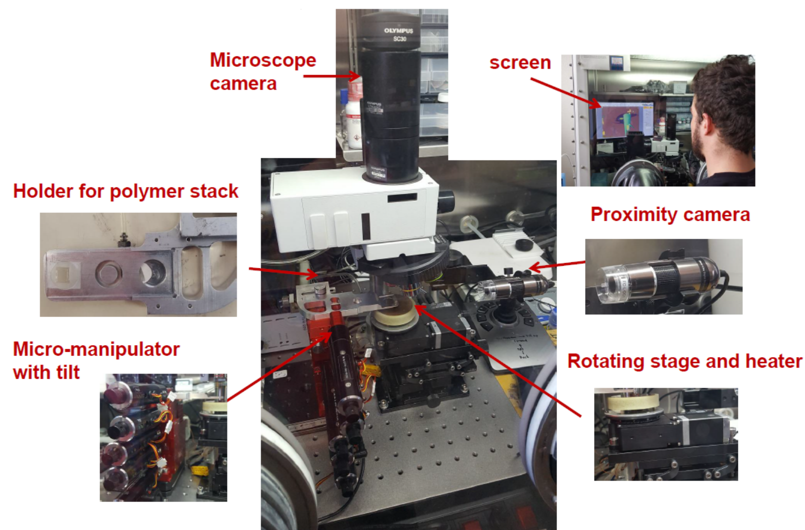

Figure 4.11: Detailed picture of our transfer set-up.

The required alignment would not be possible without a suitable transfer system, shown in *figure 4.11*. The transfer set-up consists in an optical microscope with a moving stage and a three-axis

(XYZ) micro-manipulator arm, that holds the glass plate with PPC and can be moved by three step motors connected to a joystick, down to a precision of 50 nm. The microscope stage, whose position can also be adjusted using apposite knobs, contains a sample holder with a hole and a small pump to create vacuum and keep the substrate stable during the alignment. The moving arm and the stage have to be aligned on the vertical axis under the microscope objective, from where it is possible to monitor the flakes during the procedure. Since the whole system is placed inside a glovesbox with a protective atmosphere, the microscope has to be coupled to a CCD camera which shows the images on a screen.
Once the glass plate with PPC is properly placed in the moving arm and the chip positioned on the microscope stage, with the concomitant use of the manipulator and the knobs for the horizontal movement of the stage with the sample, a uniform and clean part of PPC (there are always some wrinkles that should be avoided) is chosen and aligned vertically with the flake we are interested in picking up. Thanks to the PPC transparency, it is indeed possible to see through it, changing the working distance with the focus knob. Then, the glass plate is approached to the boron nitride lowering the arm of the manipulator until PPC contacts the substrate. In this simple first step it is important to minimize the strain on the surface, in order to reduce the risk of breaking the flake. At this purpose, it is useful to check in the microscope image if the flake moves laterally when the PPC progressively contacts the surface, which is a strong indication of the presence of mechanical stress. The stress is principally due to the non-perfect flatness of the PPC/PDMS stack on the glass plate so that, when it is approached to the sample, it does not touch the substrate horizontally. The micro-mechanical arm can be tilted to correct this planes misorientation but, in case of high stress, it is often more useful to lift up again the glass plate, rotate the sample holder of 180°[7] and re-approach the substrate.
The three-step procedure necessary for a standard encapsulation is then carried out as described previously. When two flakes have to be aligned (second and third step) the arm is slowly approached to the substrate continuously checking and adjusting the reciprocal position of the crystals (tuning properly the focus) until they touch each other. Due to the misalignment originated from some ineliminable strains and the micro-vibrations of the system, several corrections are often necessary, especially in the last step which requires micrometric precision.
Even if not specified before, after every pick up step is necessary to change the chip on the sample holder since the flakes chosen for the heterostructure are exfoliated on different substrates. Once the transfer procedure is complete, the sample is cleaned in chloroform to remove the PPC residues on the substrate.

In case the first layer that has to be picked-up is a monolayer, PPC often fails in "trapping" the flake. An alternative is constituted by a different polymer, called PC, which basically picks up every flake in the substrate. The procedure is almost the same except for the working temperatures that indeed depend on the nature of the polymer. In the first two steps the temperature is raised to 120°C, while in the final release it is increased up to 200°C. In this case, when the glass is lifted, the polymer remains on the substrate and PC residues have to be removed in chloroform at about 50°C.
Even if PC allows to pick up also monolayers flakes very easily, it has some drawbacks. First, it

[7] This rule of thumb allows to have the same alignment conditions but to change the area of the substrate in contact with the polymer.

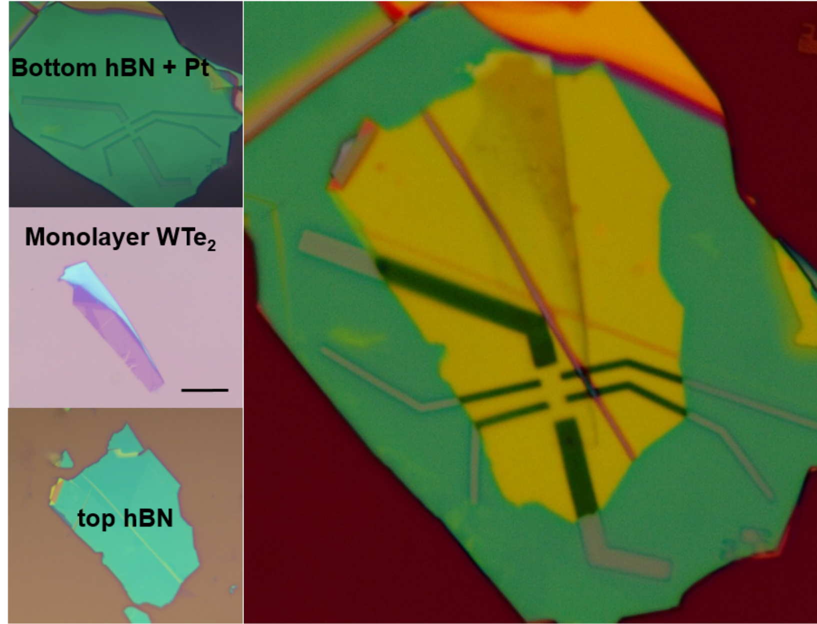

Figure 4.12: Optical image of the heterostructure with the monolayer WTe_2 encapsulated between a bottom layer hBN with pre-patterned platinum contacts and a top hBN (scale bar 10 μm).

is a less clean method, leaving more residues on the substrate, second, the more viscous nature of the polymer can lead to the breakage of the flakes. For these reasons, PPC is the only choice when very clean interfaces are required and it is usually preferred when the first flake to be picked-up is not a mono or bilayer crystal.

4.3 Heterostructures

The described transfer technique allows to assemble various kinds of van der Waals heterostructures. In the following section we describe two slightly different ways to realize WTe_2 monolayers devices which have been explored in the present experimental work.

4.3.1 Platinum contacts on bottom hBN

Flat, chemically inert and insulating, boron nitride represents the obvious choice to encapsulate monolayers WTe_2. In *figure 4.12* we can see the heterostructure obtained after the transfer procedure. As already mentioned, in this type of device a WTe_2 monolayer is encapsulated between a bottom hBN with platinum contacts and a top hBN (in the depicted case around 30 nm thick), which can be used as a dielectric for the top gate.
In the assemblage of the heterostructure care must be taken not to completely cover the platinum contacts on the bottom hBN flake, because they have to be connected with gold contacts in the second step lithography.

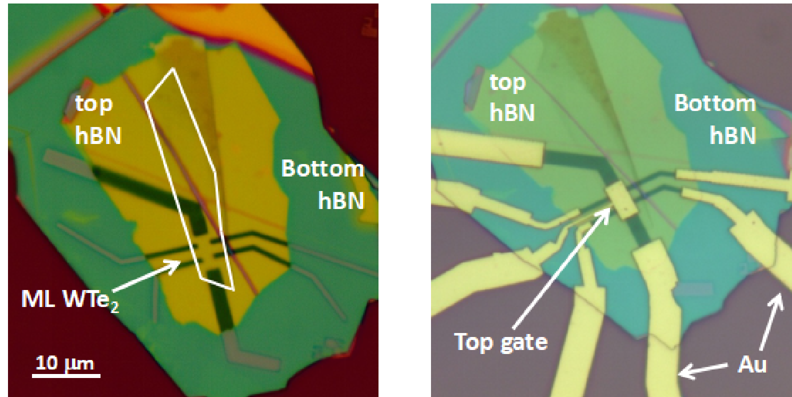

Figure 4.13: WTe_2 monolayer device encapsulated between two layers of hBN before (right) and after (left) the last contacts deposition.

The ultimate device, after the deposition of gold contacts which overlap the pre-patterned probes, is shown in *figure 4.13*, where we can see also the top gate.

4.3.2 Tunnel contacts through monolayer MoS_2

An alternative configuration in shown in *figure 4.14*: WTe_2 in this case is encapsulated between a bottom hBN and a top monolayer MoS_2. The choice of a monolayer as cover layer enables to

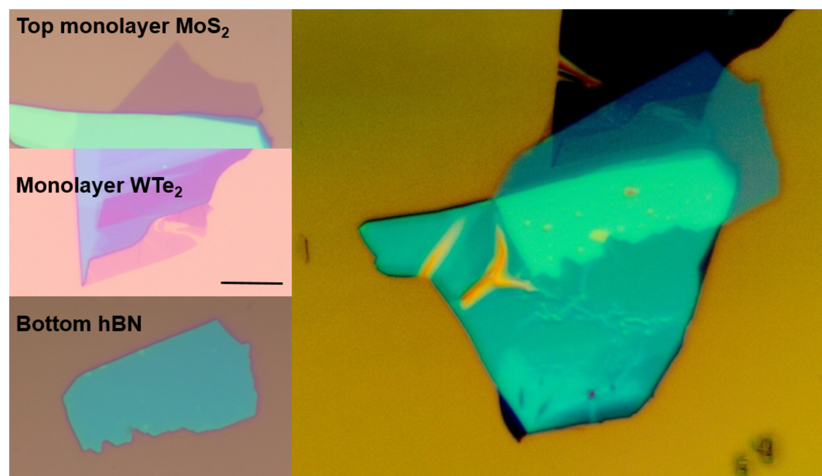

Figure 4.14: Heterostructure of monolayer WTe_2 encapsulated between a bottom layer hBN and a top monolayer MoS_2 (scale bar 10 μm).

put contacts directly on top of the heterostructure in only one step lithography and simplifies considerably the alignment in the last step of the transfer procedure. In fact, being monolayer MoS_2 insulating and only 0.7 nm thick, the current can tunnel through it, reaching the monolayer WTe_2 beneath. Also monolayer hBN could be used for the same goal, but monolayer

MoS_2 is chosen simply because it is more easily obtained by exfoliation.
A picture of the final device is shown in *figure 4.15*; as it is evident from the image, adding contacts after the transfer procedure allows to pattern the desired geometry, following the shape of the flake very precisely. In the depicted device, contacts are defined in this way to short-cut the thick part of the WTe_2 (which is not uniform in thickness) and with the aim of doing some non local measurements, varying the number of contacts in the current path and the distance between the probes. Unfortunately, the back gate of this device was not working properly so we will not go further in the discussion of the experimental results.
It is anyway remarkable the possibility to use tunnel contacts through monolayer crystals, since it allows big advantages in terms of fabrication time and success rate.

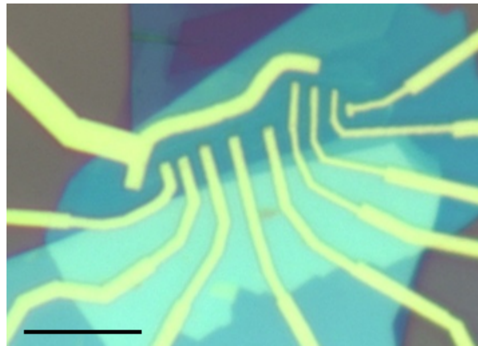

Figure 4.15: WTe_2 monolayer device with tunnel contacts (Pt/Au) through a monolayer MoS_2 (scale bar 10 μm).

Chapter 5

Electronic properties of WTe_2 crystals

The purpose of the present work is mainly to study the electronic properties of encapsulated monolayers WTe_2 by means of transport measurements on nano-fabricated devices which prevent the degradation of the crystal. In this chapter we will show the measurements we have performed and we will discuss the conclusion we can extract from their analysis.
First, we will briefly describe the measurement system that has been used to collect these data, which includes a liquid helium cryostat with a superconducting magnet to reach low temperatures and high magnetic fields. Secondly, we will address the actual data analysis starting with a quality assessment of our WTe_2 crystals in a bulk sample, in order to compare the values of the mobilities and carrier densities with the ones of crystals analysed in previous experimental works. Then, we will focus on the data obtained by a monolayer device which we have measured in more detail and that shows edge conduction, in accordance with current results of other research groups.

5.1 Measurement set-up

A system for low-temperature magnetotransport measurements generally consists in a *cryostat* containing the coolant and a superconducting magnet, an *insert* with a slot for the sample, and a set of electronic instruments (e.g. lock-in amplifier, multimeter, current/voltage sources, etc.) interfaced to the computer. Several types of different system architectures exist which may differ, for instance, for the cooling mechanisms or the insert structure.
To perform the measurements of this experimental work we used a *Heliox*^{TM} system produced by *Oxford Instruments*, whose working principle and main features are briefly explained in the following section.

5.1.1 The cryostat

The cryostat, as we can see in *figure 5.1 (a)*, is basically a dewar with a cylindrical shape, made of a double metal wall in the middle of which vacuum is pumped to prevent as much as possible the heat exchange with the environment. Inside the cryostat is stored the refrigerant fluid, i.e. ^4He (boiling temperature of 4.2 K at atmospheric pressure), which in a wet system

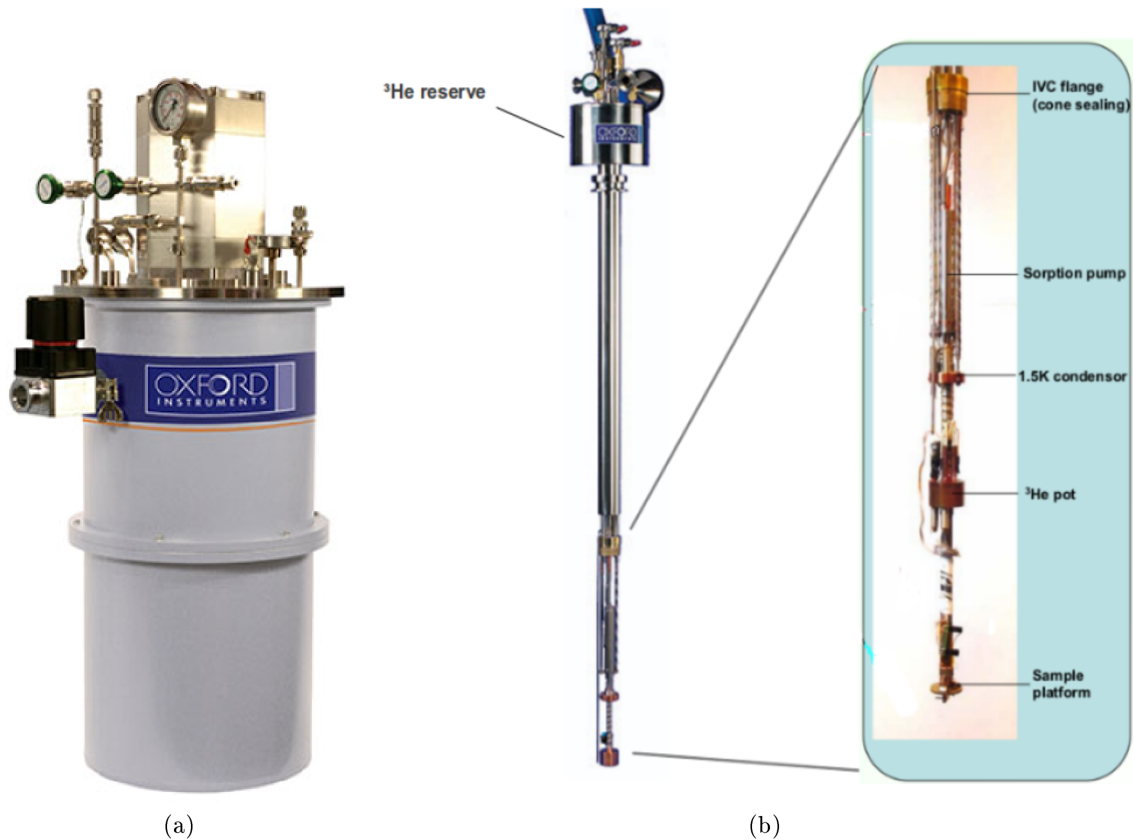

(a) (b)

Figure 5.1: Cryostat (a) and insert (b) of a $Heliox^{TM}$ system.

has to be refilled periodically because of the inevitable evaporation. The presence of a recovery line allows helium recycling, preventing its dispersion in the environment.
A superconducting magnet, which can generate a magnetic field parallel to the dewar axis with intensity up to 15 T, is placed at the base of the cryostat so that, when it is immersed in the helium bath, it is below its critical temperature ($T_c > 4.2$ K).
On top of the dewar there is a cap with a small circular opening for the insert.

5.1.2 The insert

The insert, shown in *figure 5.1 (b)*, is a device about two meters long, externally grounded, that, as the name suggests, is inserted from the top inside the cryostat. In this way the terminal part of the insert, the so-called *Inner Vacuum Chamber* (IVC), i.e. a cylindrical shell of brass kept in high vacuum with an external pump, is in contact with the helium bath.
At the bottom of the insert there is a small slot for the chip carrier, with a set of wires that connect each pin to a control panel out of the dewar.
As a result, the sample, hermetically closed inside the IVC, cools down reaching the thermal

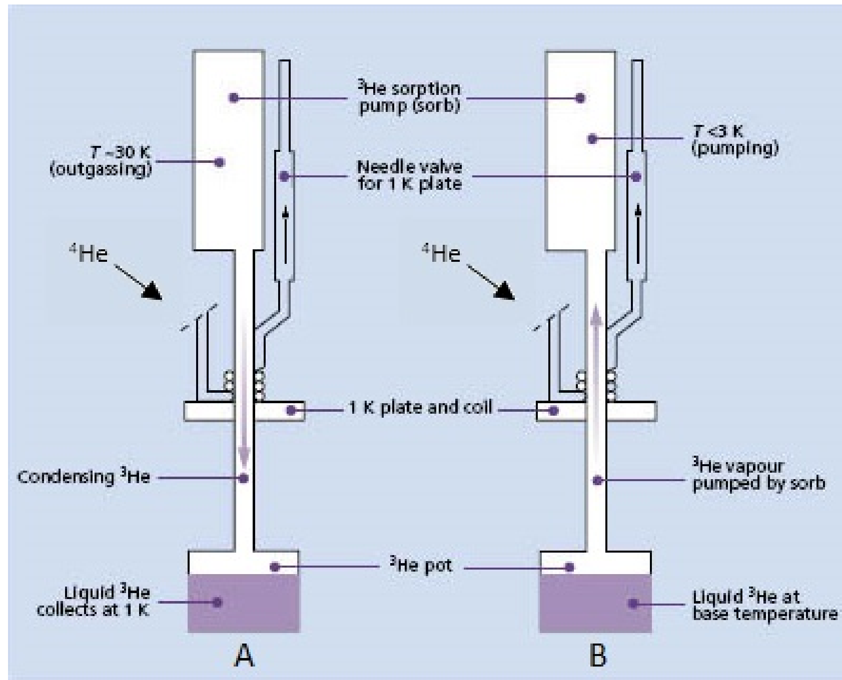

Figure 5.2: Scheme of the recondensing process of the ^{3}He.

equilibrium with the helium bath. In order to decrease the temperature to 4.2 K a small amount of helium gas, the so-called *exchange gas*, is used to enhance the heat thermalization.
A lower temperature can be reached removing the exchange gas and pumping on the *needle valve*, a thin tube immersed in the helium bath. In this way ^{4}He is collected in the 1.5 K condenser, also called *1 K plate*, where, due to the low pressure, it evaporates extracting heat from the plate that cools down to 1.5 K.

If the desired temperature is lower than 1.5 K, ^3He is needed for more cooling power. ^{3}He is contained inside a closed hermetic circuit extending from the ^3He *reserve* until the ^3He *pot*; always the same gas circulates in the circuit and no refilling is necessary. At 4 K, inside the circuit, the ^3He is in gaseous form and, in order to be employed, has to be recondensed following a particular procedure sketched in *figure 5.2*.
Heating up the *sorption pump* at about 30 K, by means of an embedded resistance, the pressure in it increases also due to the release of ^{3}He atoms adsorbed by the walls of the chamber. This gives rise to a flux of gas directed to the ^{3}He pot, where, because of the higher pressure, the gas collects in form of liquid ^{3}He with a temperature of $\sim$ 1 K (*fig. 5.2 A*). During this process, the heat is carried away through a flux of gaseous ^{4}He in a second separate circuit, which is in thermal contact with the ^{3}He circuit in correspondence of the 1 K pot. In this circuit, as described before, the ^{4}He is sucked from the bath at the bottom of the cryostat and, from the 1 K pot it goes to the recovery line.
After this preliminary phase, the heater is switched off and the pressure in the sorb decreases, causing an inversion of the ^{3}He flux which evaporates from the ^{3}He pot (*fig. 5.2 B*). That causes the temperature of the liquid ^{3}He to drop down to $\sim$ 250 mK and the sample, being in

thermal contact with the ^{3}He pot through a metal connection, thermalizes with it reaching the same temperature.
Naturally, this temperature can be conserved only for a limited period, determined by the time taken by the ^{3}He to evaporate, typically a couple of days. After that time, the temperature increases again to ~ 4 K, and, if a lower temperature is needed, the ^{3}He has to be recondensed again restarting the cycle.

5.1.3 Measurement instrumentation

In transport measurement two main different configurations are possible, depending on whether a current source or a voltage source is used. In *current-bias* a current is injected in the sample and a voltage drop is measured, while in *voltage-bias* a voltage is applied and a current is read. The choice of the more suitable configuration depends of the value of the resistance that has to be measured. Current-bias configuration is usually preferred when the resistance of the sample is not too high. In fact, the risk with this method is that, when the resistance of the material is high and the temperature is low, the heat released in the sample by joule effect becomes comparable to to the thermal energy of the electrons. Specifically, when

$$RI \geq \frac{k_B T}{e} \tag{5.1}$$

the joule effect starts to play an important role and the measured resistance gets an inconvenient dependence on the current. If the applied current is of the order of nA at a temperature of T=250 mK, according to equation (5.1) the heating is negligible up to resistances of about 100 KΩ. Otherwise, for sample of higher resistance is better to use instead a voltage bias configuration. For the measurements on WTe_2 samples we mainly use a current bias configuration, since the resistance values are generally lower than 100 KΩ.
The signal is sourced in AC using a *lock-in amplifier* with a frequency typically of 17 Hz, or more in general enough far from an entire multiple of the electrical noise frequency (50 Hz). The lock-in allows to extract (and eventually amplify) the signal from the background noise, removing all the signal components with frequency different from the input.
The measurements are commonly carried out as a function of different parameters, such as, temperature, gate voltage or magnetic field. The gate voltage is applied with a highly stable DC voltage source, connected to the computer for a remote control of the gate sweeping.
The data are gathered and elaborated with a computer interfaced to the instruments; in our case the software for the data acquisition has been implemented in $LabVIEW^{TM}$.

5.2 Characterization of bulk samples

To perform magnetotransport measurements it is useful to have devices shaped in a Hall bar geometry, with two big contacts mainly used to source and drain current and small lateral voltage probes (*fig. 5.3 (a)*). This configuration allows the measurement of four-terminal resistances, excluding the contribution of the contact resistance between the metal contacts and the material investigated.
To check the quality of the WTe_2 crystals we consider the bulk device depicted in *figure 5.3 (b)*

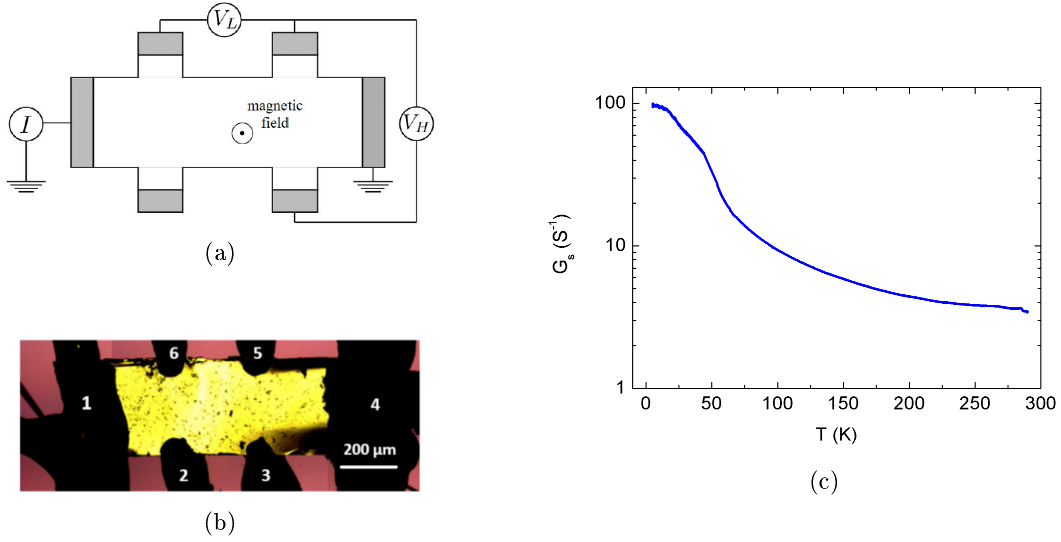

Figure 5.3: (a) Schematic representation of a Hall bar configuration; V_L is the longitudinal voltage and V_H the Hall voltage. (b) Optical image of a bulk sample of WTe_2 with a Hall bar geometry. (c) Temperature dependence of the four-terminal conductance for two adjacent probes in the bulk device, showing a metallic behaviour coherent with the theoretical prediction.

with a WTe_2 thickness of $t = 42.1\,\mu m$; the "large" dimensions of the sample allow to connect directly the gold wires to the crystal using epoxy.

We start the crystal characterization, observing how the resistance changes cooling the sample down from room to cryogenic temperatures. Sending current between contacts 1 and 4 and measuring the voltage drop across probes 2 and 3 we find a four-terminal resistance $R_4 \sim 0.3\ \Omega$ at 290 K which decreases by one order of magnitude at 4.2 K reaching $R_4 \sim 0.01\ \Omega$. As we can see in *figure 5.3 (c)*, the conductance increases decreasing temperature coherently with what is expected in bulk WTe_2 (see *fig. 3.6 (a)* for comparison).

In order to obtain the mobility of the charge carriers, we then analyse magnetotransport at base temperature (250 mK). In *figure 5.4 (a)* the longitudinal magnetoresistance is plotted varying the magnetic field between -14 T and 14 T. The trend is quadratic and non-saturating, in accordance with the prediction for a nearly perfect compensated semimetal; moreover Shubnikov-de Haas oscillations are visible for fields larger than $\sim$ 4 T. The oscillations can be extracted from the quadratic background (*fig. 5.4 (b)*) and their analysis provide us important informations. From the Fourier transform of the SdH oscillations we can extract the characteristic frequencies of the charge carriers. The spectrum in *figure 5.5* shows four dominant peaks corresponding to the four electron-hole pockets in the Fermi surface of bulk WTe_2 and it is consistent with spectra observed in other crystals (*fig. 5.6*). From the values of the frequencies using (3.1) and (3.2) we can calculate the densities of electrons and holes which can be used as initial estimates for the fitting of the longitudinal and transverse resistivities. Summing up the two concentration values relative to the splitted valence and conduction bands we obtain the following carrier

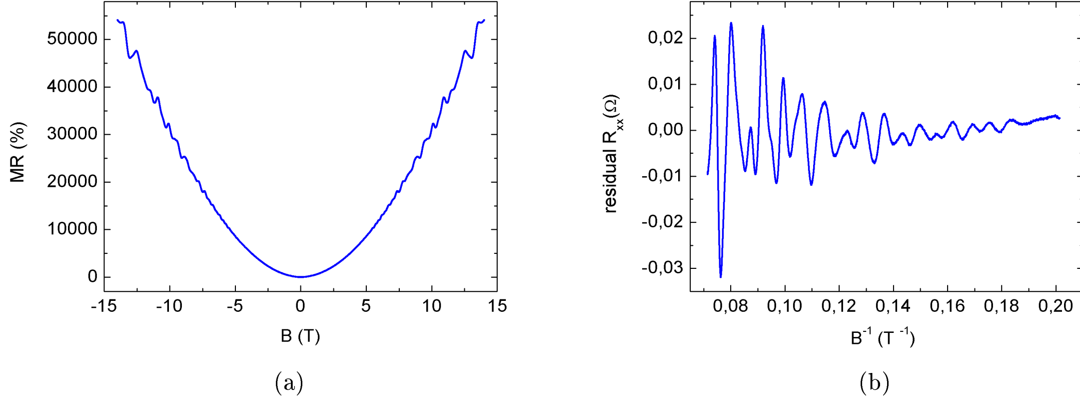

(a)

(b)

Figure 5.4: (a) Magnetoresistance measured between probes 2 and 3 at 250 mK. (b)Shubnikov-de Haas oscillations obtained by subtracting the quadratic background from the longitudinal resistivity, plotted as a function of B^{-1}.

densities for holes and electrons, respectively:

$$n_h = 1.580 \cdot 10^{19}\ cm^{-3} \qquad\qquad n_e = 1.776 \cdot 10^{19}\ cm^{-3} \tag{5.2}$$

which confirm the nearly compensated nature of the semimetal ($n/p \sim 1.124$). Using the

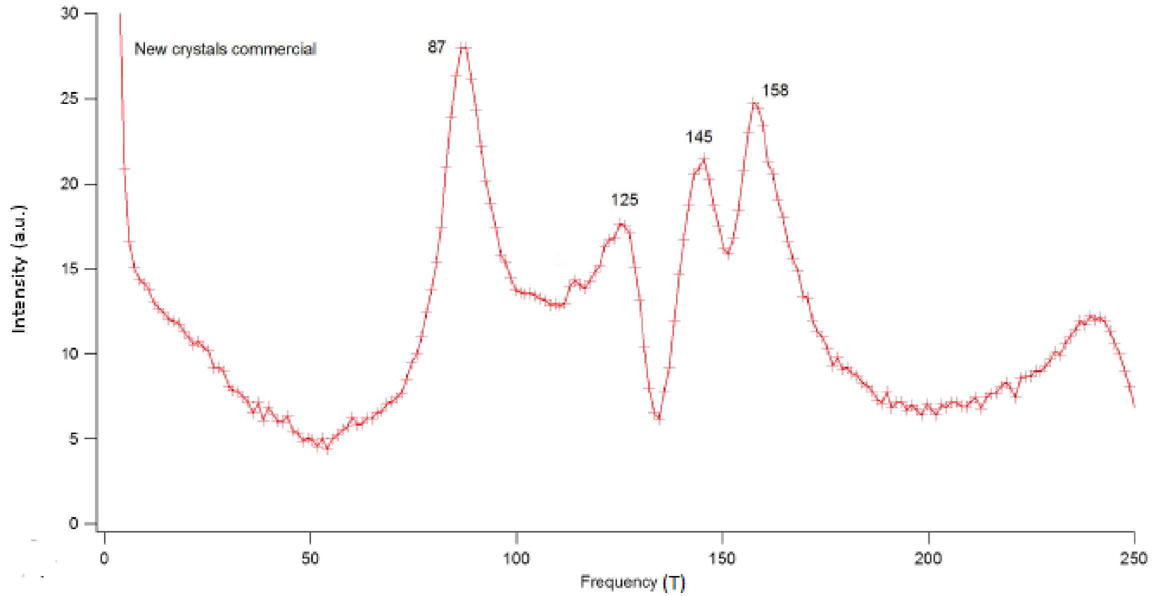

Figure 5.5: Fourier transform of the SdH oscillations; four dominant frequency peaks are clearly visible.

conditions (3.3) we can then estimates the mobilities for both carriers so that we have all the four parameters and we can use equations (2.43) and (2.44) to fit our experimental data.
The outcome of the fitting procedure is represented in *figure 5.7* for ρ_{xx} and ρ_{xy}. The agreement

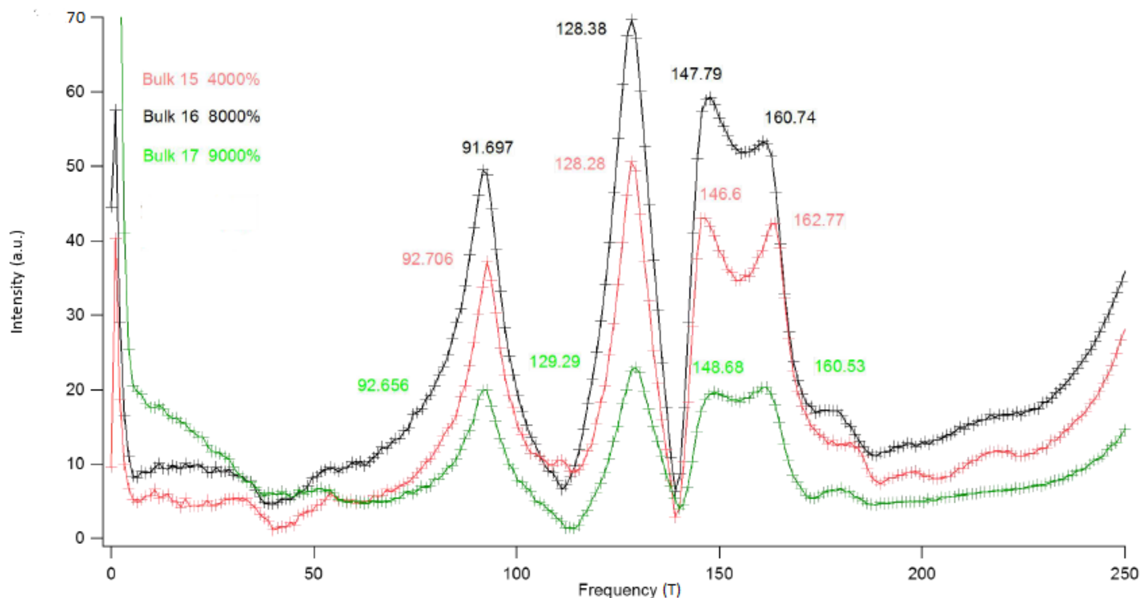

Figure 5.6: Frequency spectra relative to different crystals obtained in previous experimental work; the three samples analysed have different maximum values of magnetoresistance [38].

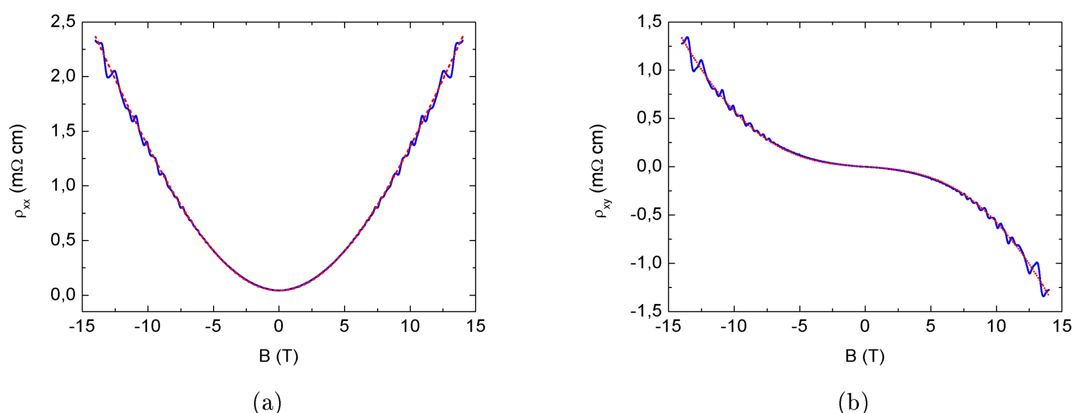

(a) (b)

Figure 5.7: (a) Longitudinal and (b) transverse resistivity as a function of the magnetic field at T=250 mK; the blue lines represent the experimental data and the red dotted line the theoretical fit with equations (2.43) and (2.44), respectively.

between the measurements and theory is excellent confirming that bulk WTe_2 is well described

by a classical two bands model. The values of densities and mobilities extracted from the fitting are very close to our initial guess, in particular:

$$\begin{aligned} n_h &= 1.111 \cdot 10^{19}\ cm^{-3} \qquad & n_e &= 1.260 \cdot 10^{19}\ cm^{-3} \\ \mu_h &= 4990\ cm^2/Vs & \mu_e &= 7238\ cm^2/Vs. \end{aligned} \tag{5.3}$$

As we could expect from the trend of the transverse resistivity, in our crystals both the charge density and the mobility are larger for electrons than for holes. Furthermore the obtained mobilities are consistent with expectations for bulk samples and confirm the good quality of the crystals.

5.3 Edge conduction in monolayer WTe_2

As it is evident from the description of the sample preparation in the previous chapter, the complexity of the devices required to study atomically thin crystals of WTe_2 increases drastically as compared to bulk samples.
In the following section we will present the results we obtained from the device shown in *figure 5.8 (a)*; the encapsulated WTe_2 monolayer is characterized by a thicker part on one side, as we can see from the optical image in *figure 5.8 (b)*. For this reason we can schematically represent the device like in *figure 5.8 (c)*, where the light-blue part represents the thicker part of the WTe_2 crystal and the yellow contact is the top gate.

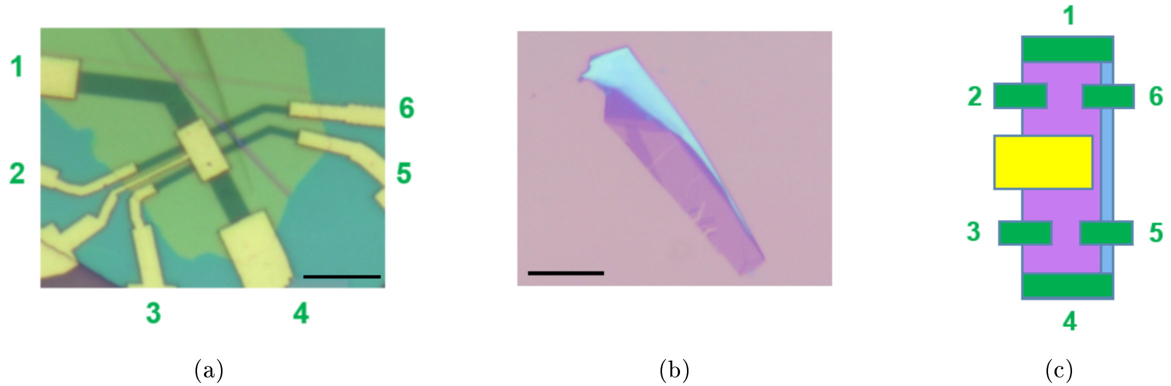

Figure 5.8: Optical images (scale bar 10 μm) of the WTe_2 monolayer device (a) and of the WTe_2 monolayer crystal encapsulated in it (b). (c) Scheme of the device.

Thickness dependent electronic properties

The non uniformity of thickness manifests in different trends of the resistances as a function of the temperature, measured in a four terminal configuration across two probes on opposite sides of the device in *figure 5.8 (a)*, sending current from contact 1 to 4. As we can notice in *figure 5.9*, while the thin side (voltage drop measured between probes 2 and 3) shows an insulating

behaviour, the thick one (between probes 6 and 5) is metallic.
Magnetoresistance measurements confirm the transport regime is different at the two sides of the sample, showing signature of weak anti-localization and an approximately quadratic magnetoresistance for the monolayer and the thick part, respectively (*fig. 5.10*).

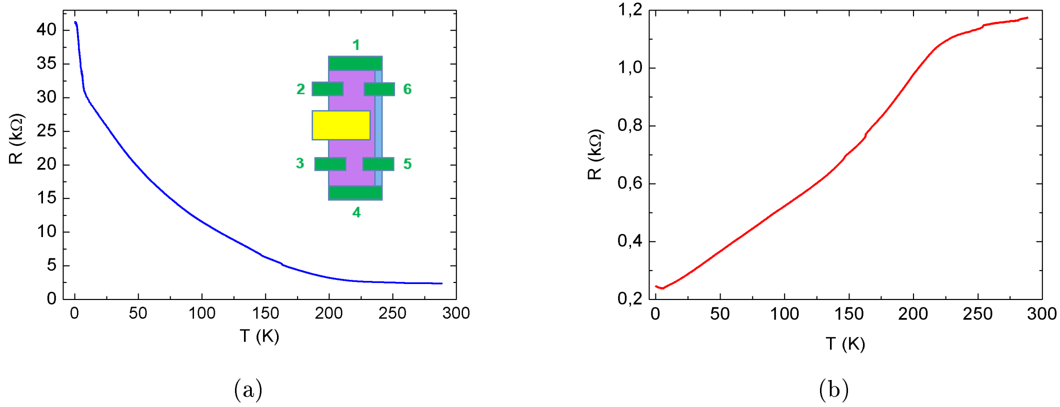

Figure 5.9: Temperature dependence of the resistance between two probes for the thin side (probes 2-3) which shows insulating behaviour (a) and for the thick one (probes 6-5) that shows a metallic trend (b).

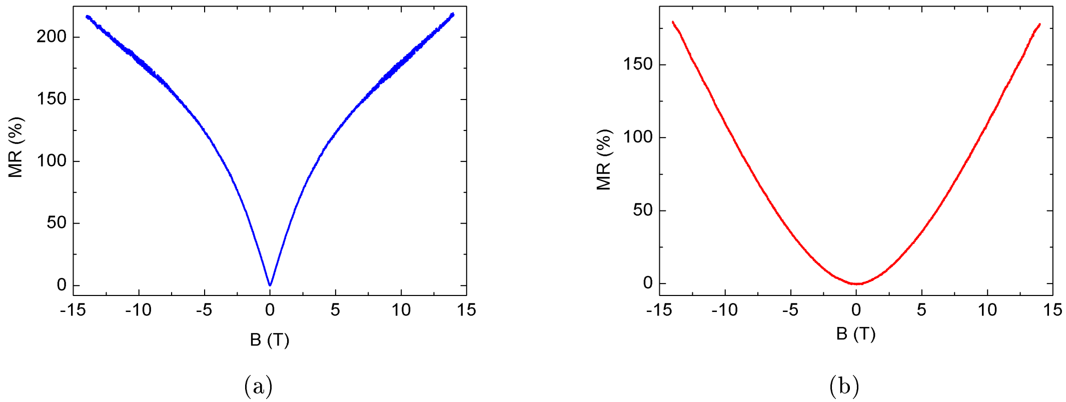

Figure 5.10: Magnetoresistance between two adjacent probes on the thin side (a) and on the thick side (b), measured at T=4.2 K. While the MR of the thin part (between probes 2-3) shows a trend typical of weak anti-localization, the thick part (probes 6-5) is fairly quadratic like in bulk samples.

Finally it is interesting to compare the different trends of the conductance as a function of gate voltage in *figure 5.11*. While the monolayer (blue curve) shows a peculiar gate dependence which will be analysed in depth in the next paragraph, the bulk part (red curve) has a high conductance, coherently with a nearly metallic behaviour.

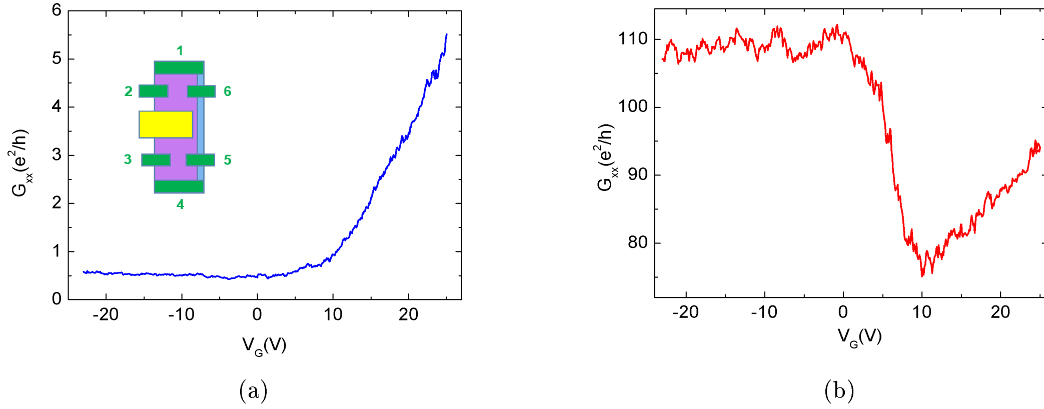

Figure 5.11: Conductance as a function of the gate voltage between two adjacent probes on the monolayer side (a) and on the bulk side (b), measured at 0.25 K in a four-terminal configuration. It should be noticed the high values of conductance on the thick part (probes 6-5).

Since the multilayer part has lower resistance it acts as a preferential path for the current in the crystal and it could affect our results. A possibility to exclude the contribution of the thick part consists in etching away the WTe_2 crystal between probes 6 and 5 in the device.
As we can see in *figure 5.12 (a)*, this is what has been done and the temperature dependence of the resistance of the etched device highlights an insulating behaviour on both sides. However,

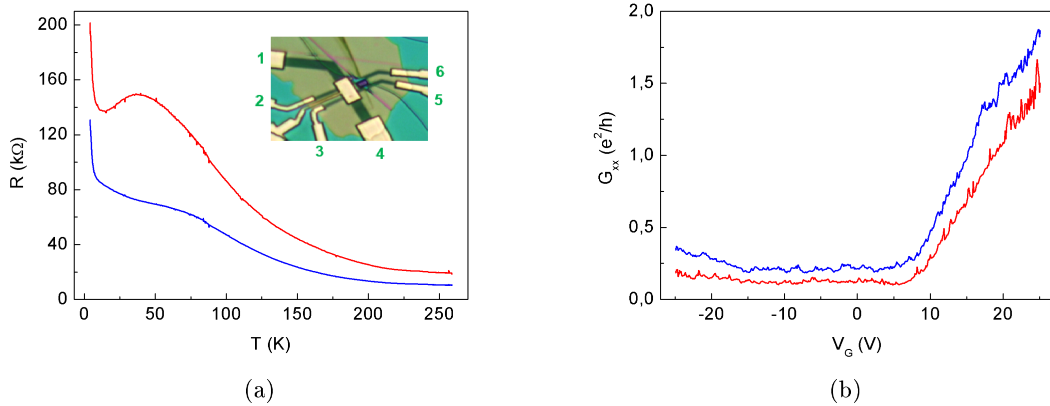

Figure 5.12: (a) Temperature dependence of the resistance across two probes at the opposite sides of the device after the thick part of WTe_2 between probes 5 and 6 has been etched away, as it is visible in the inset. We can notice that both display a metallic trend but the resistance values increased after etching. (b) Conductance as a function of the gate voltage for the same two pairs of contacts, which highlights the same gate dependence. The measurements are performed at T=4.2 K. In both figures the blue curves are relative to the pair of contact 2-3, while the red one to the pair 6-5.

the etching procedure most likely compromised the integrity of the crystal (the monolayer is more exposed to air) and the values of the resistance are larger compared to the ones of the previous measurements.
An additional proof which confirms that the bulk part has been etched away is given by the gate dependence of the conductance: differently from what observed before etching, in this next step the curves are characterized by a similar behaviour (*fig. 5.12 (b)*).

5.3.1 Observation of a gap

If we now consider again the resistance-temperature (R-T) curve in *figure 5.7 (a)*, which shows an insulating behaviour, we can obtain the value of the *activation energy* E_a from the *Arrhenius plot* of the conductance

$$ln(G) = ln(G_0) + \frac{E_a}{k_B}\frac{1}{T}. \tag{5.4}$$

The activation energy in a semiconductor is nothing but the distance between the Fermi level and the conduction band and, in case of intrinsic semiconductors, the value of the energy gap can be simply calculated multiplying E_a by a factor of two.
From the fitting of $ln(G)$ at high temperatures, that we can see in *figure 5.13*, we extract an activation energy of around

$$E_a \sim 30\ meV \tag{5.5}$$

which gives us a rough estimate of the order of magnitude of the energy gap. Although the precise value of E_g depends on the position of the Fermi energy inside the gap and then on the

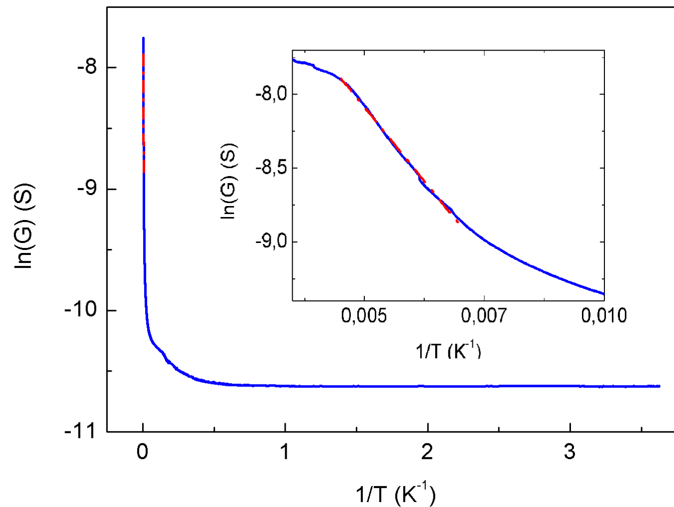

Figure 5.13: Logarithm of the conductance as a function of the reciprocal of the temperature. Fitting the linear part at high temperatures, it is possible to extract the activation energy. The measurements are performed at zero gate voltage (V$_G$=0).

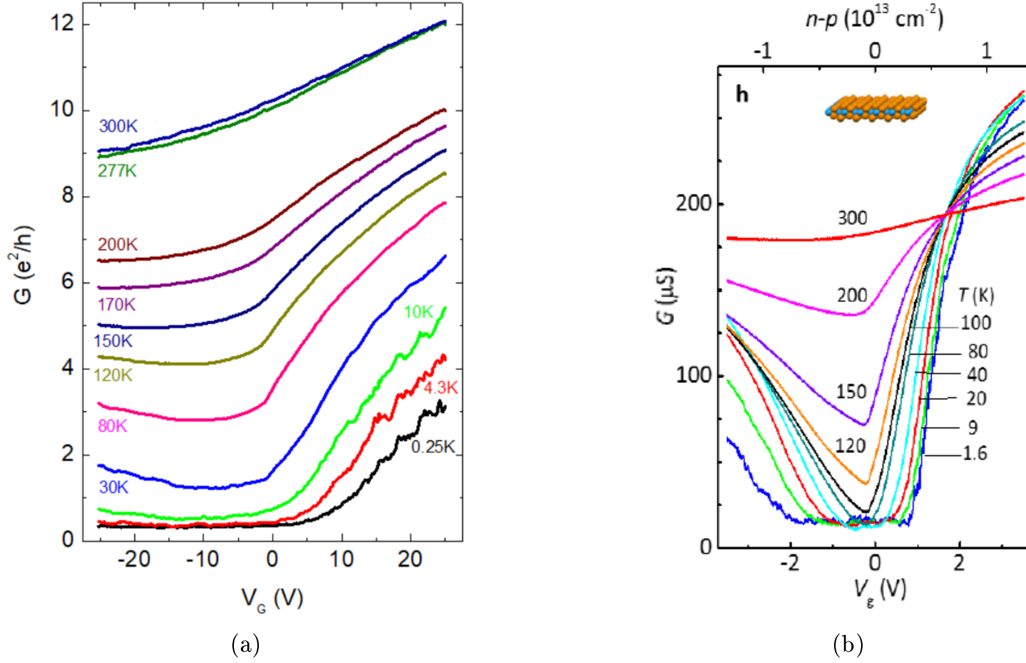

Figure 5.14: (a) Conductance as a function of gate voltage at different temperatures between two adjacent probes of the WTe_2 monolayer device shown in *figure 5.6*; plateaus are clearly visible at low temperatures. (b) Temperature dependence of the conductance obtained by Z. Fey et al. [17].

gate voltage at which the measurements are performed, our result is not too far from the value of the energy gap estimated through ARPES and STM measurements, equal to 45-55 meV [36] (see *fig. 1.6 (b)*). Moreover it is sufficiently consistent with the observation of the ineffectiveness of the gap at room temperature, where the thermal energy is enough high to activate the charge carriers ($E(300K) = k_B T \sim$25 meV). The obtained value seems to be slightly overestimated but it has to be taken in consideration that at these small energy scales also the effect of impurities or defects in the material could play an important role. For this reason it is already satisfactory that the analysis of our data highlights the presence of a gap, whose order of magnitude is in accordance with the expectations.
The existence of a gap in monolayer WTe_2 is confirmed by the gate dependence of the two-terminal conductance at different temperatures shown in *figure 5.14 (a)*. Interestingly, the conductance stops dropping at low temperatures and a plateau characterized by a non-zero value of G is clearly visible below 4.3 K. As we can see from the comparison with *figure 5.14 (b)*, the observed behaviour is consistent with the results currently obtained by other research groups. An ambipolar transport is present, though in our case the gate dependence is much more evident for the electron side than for the hole one, showing that the Fermi energy at $V_G = 0$ is much closer to the conduction band.
The observation of a non-zero value of conductance inside the gap, which is equal to 0.336 e^2/h at 250 mK (*fig. 5.15*), strongly suggests the presence of edge states.
As already seen in *chapter 2*, the two-terminal conductance in case of helical states is predicted

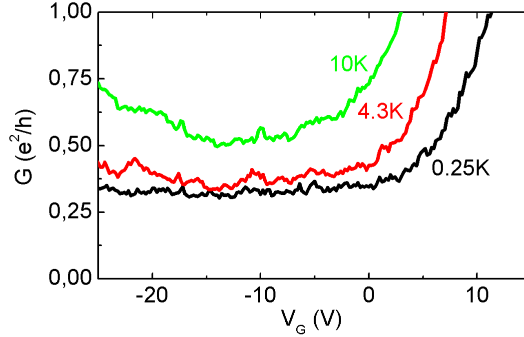

Figure 5.15: Zoom-in of selected curves of the conductance at low temperatures which highlights the plateaus inside the gap. The values are shown in units of e^2/h.

to be $2e^2/h$ because we need to consider one quantum mode present at each edge. However, considering the geometry of our multi-terminal device, if we measure between two adjacent probes it is reasonable to expect the contribution of one edge state to be much more relevant than the contribution of the other one, whose conductance is reduced by the several contacts in the current path, as predicted by the theory. In addition, the "big" dimensions of the WTe_2 crystal, together with the presence of the thicker part on one side, could also play a non negligible role. In fact, even if protected helical states should have a conductance independent of the length, previous experimental results suggest that the long path along the edge of the crystal could be another reason for the suppression of one conductive channel. From these considerations, measuring the voltage drop between contacts 2 and 3 in the device shown in *figure 5.8 (a)*, we can reasonably expect a two-terminal conductance of e^2/h, i.e. a conductance about a factor of three larger than the value we found in our measurements.
Despite it is encouraging that the measured conductance is fairly constant in the gap (except for mesoscopic fluctuations) and it never exceeds the predicted value, the absence of a precise quantization of G confirms once again the puzzling nature of the quantum spin Hall effect. Possible reasons to explain the reduced value of the conductance could be the presence of magnetic impurities in the material, which would break the time reversal symmetry, or the imperfect transmission between the metal contacts and the edges.
The latter is probably the most important factor, especially if we consider the values of contact resistance R_c found for the device. Comparing the four-terminal and two-terminal measurements we can obtain a rough estimate of R_c, which results to be about 6.5 $K\Omega$ at room temperature and increases with the cooling down.
The non optimal quality of the contacts could be due to the non perfect adhesion between the bottom platinum probes and the WTe_2 crystal that is placed on top of them. The way in which the heterostructure is assembled, in fact, inevitably introduces some strain and, even if the pre-patterned contacts on the bottom boron nitride are only few nanometers thick, the monolayer is most likely a bit bent.
In order to get a better adhesion between the probes and the WTe_2 crystal we tried an alter-

native heterostructure using tunnel contacts through monolayer MoS_2, as described in the last part of the previous chapter. Monolayer MoS_2 is indeed insulating ($E_g = 1.8$ eV) and it is only 0.7 nm thick so that the current is expected to be able to tunnel through it. In this case the contact resistance would be determined by the tunnelling barrier and then it should be also independent of temperature. The device we realized confirms the possibility of making tunnel contacts through monolayer MoS_2 with a contact resistance at room temperature of about 1.5 KΩ, hence smaller than the one measured with platinum bottom contacts. Although the results obtained by a single sample cannot be considered conclusive and measurements on other devices are necessary, these first data seem promising and, considering also the advantages in terms of fabrication-time and difficulty, this heterostructure could be a valid alternative for future developments.

5.3.2 Non-local measurements

A further proof of the presence of edge conduction can be obtained by non-local measurements, as already mentioned in *chapter 2*.
In *figure 5.16* we can see the non-local conductance as a function of gate voltage measured in some different configurations in the device of *figure 5.8 (a)*. To avoid the influence of the thicker part of the WTe_2 crystal we short-cut probes 5 and 6, so that we can assume the device to be five-terminals.
From a first look at the conductance trends it is clear the presence of plateaus inside the gap which confirm the existence of edge states. Moreover a non-zero voltage drop across probes far away from the contacts between which the current is sourced implies non-local transport and constitutes an additional hint of edge conduction.
Following the Landauer-Büttiker approach it is possible to calculate the expected values of the non-local resistances in case of helical states, as described in *section 2.6.3*. In particular the transmission coefficients T_{ij} between probe j and its neighbour i are different from zero clockwise for spin-up states and counter-clockwise for spin-down states:

$$\begin{cases} T^{\uparrow}_{12} = T^{\uparrow}_{23} = T^{\uparrow}_{34} = T^{\uparrow}_{45} = T^{\uparrow}_{51} = 1 \\ 0 \quad otherwise \end{cases} \qquad \begin{cases} T^{\downarrow}_{21} = T^{\downarrow}_{32} = T^{\downarrow}_{43} = T^{\downarrow}_{54} = T^{\downarrow}_{15} = 1 \\ 0 \quad otherwise. \end{cases} \tag{5.6}$$

Generalizing equation (2.15) for a five-terminal configuration we obtain the following transmission matrix:

$$\begin{pmatrix} 2 & -1 & 0 & 0 & -1 \\ -1 & 2 & -1 & 0 & 0 \\ 0 & -1 & 2 & -1 & 0 \\ 0 & 0 & -1 & 2 & -1 \\ -1 & 0 & 0 & -1 & -2 \end{pmatrix} \tag{5.7}$$

If we put an arbitrary voltage probe to zero and we set the conditions of conservation of current, considering that it must vanish at all the probes expect the source and drain, we can solve the associated system of equations. For instance, applying a current between probe 1 and 2 and

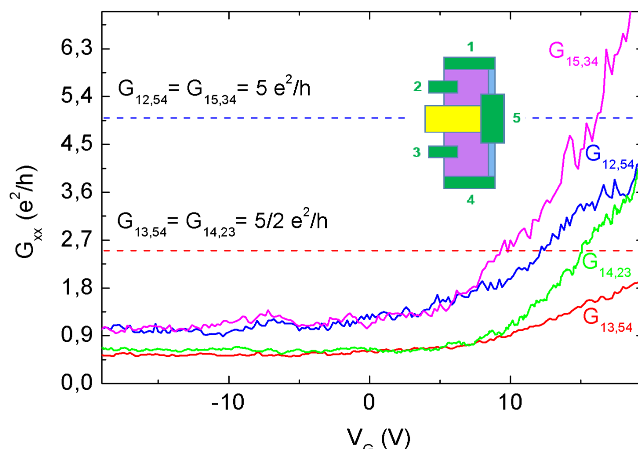

Figure 5.16: Non-local conductance for three different configurations and four-probe conductance ($G_{14,23}$) as a function of gate voltage, at T=250 mK. The predicted values for helical states are visible in dashed lines.

measuring a voltage across probes 5 and 4, we have the following conditions

$$\begin{cases} I_1 = -I_2 = I \\ I_3 = I_5 = I_4 = 0 \\ V_4 = 0 \end{cases} \tag{5.8}$$

so that the five equations are non-independent and we can calculate the non-local resistance

$$R_{12,54} = \frac{V_5 - V_4}{I} = \frac{V_5}{I} = \frac{1}{5}\frac{h}{e^2}. \tag{5.9}$$

In an analogous way it is possible to find the resistance values for the other configurations. The calculated conductances are shown in *figure 5.16* with dotted lines, while the experimental data in straight lines. As we can see from the graph, the measured values are not in accordance with the expectations but interestingly the conductances scale proportionally with the theoretical predictions. In particular from our data emerge conductances a factor of five smaller than the expected values. Moreover it is remarkable the comparison between the conductance values inside and outside the gap, obtained by different configurations. While inside the gap the conductance is the same for configurations with the same number of contacts in the current path (like $G_{12,54}$ and $G_{15,34}$), coherently with the presence of edge states, outside the gap the peculiar geometry (e.g. the different distances between contacts) of the considered configurations comes into play.
These results, consistently with the two-terminal measurements discussed in the previous paragraph, confirm edge conduction in monolayer WTe_2 but besides highlight the presence of elements responsible for a suppression of the conductance.

5.4 Results

The results obtained from the study of transport properties in our devices, with atomically thin WTe_2 crystals encapsulated in layers of inert materials, are in accordance with the data presented by Z. Fey et al. [17] and provide evidence for edge conduction, as expected in a scenario based on a topological insulator.
The activation energy extracted from the resistance-temperature curve shows the presence of a gap in WTe_2 monolayer, whose order of magnitude is in line with the value obtained through STM and ARPES spectra [36] (45÷ 55 meV) and emphasises the potential of monolayers TMDs as a large bandgap class of 2D topological insulators.
The observation of plateaus of conductance when the charge carriers density is tuned, varying the applied gate voltage, confirms the presence of a gap, and the constant non-zero measured value strongly suggests the existence of edge states inside the gap. Edge conduction is further highlighted by non-local measurements in different configurations, which show conductances of the order of fractions of e^2/h that follow a trend in agreement with what is predicted by the Landauer-Büttiker formalism.
The measured two-terminal conductance (G=0.33 e^2/h) is smaller than the one expected for helical states in an ideal two-dimensional topological insulator, and also the values of the conductance obtained by the non-local configurations are reduced as compared to the predictions. The motivations linked to the suppression of the edge current are still unknown, even if it is probable that in these devices the quality of the contact between the metal and the edge states plays an important role. The difficulty of making a good contact is due to the small physical dimensions of the helical states, which are located on a nanometric extension along the sample boundaries. That leads to a transmission probability from the contact to the one-dimensional edge mode much smaller than one and makes not trivial the filling of all the available states for the electrons. Furthermore, differently from the quantum Hall state, in which the presence of the magnetic field ensures several bounces of the electrons on the contact and then maximizes the probability of transmission in the lead, in the quantum spin Hall state if the carriers are reflected back at the interface they simply do not enter any more in the contact.
This is most likely the reason why a perfect quantization has, so far, never been observed in a quantum spin Hall state. Then, in order to proper investigate the possible physical origin of the deviation of the experimental data from the quantized values predicted by the theory, it would be certainly important to reduce the scattering contribution given by bad quality contacts. In that regard, for future developments in the direction of a better comprehension of the quantum spin Hall effect, it seems crucial finding a better way to realize contacts in these devices.

Conclusions

Aim of the present thesis is the investigation of the electronic properties of WTe_2 in the few layer form by means of transport measurements in suitable nano-fabricated devices. Theoretical calculations have indeed recently predicted strained monolayer WTe_2 to be a 2D topological insulator (alternatively called quantum spin Hall state). Topological insulators are a novel class of materials characterized by an insulating bulk with unconventional conducting channels at their physical boundaries, referred as helical states.
Since the material is not completely stable in air the oxidation of the surface significantly affects transport in few layer crystals, leading to a disorder-induced metal-insulator transition. The solution proposed to prevent the degradation is an encapsulation of monolayer WTe_2 between layers of an inert 2D material, like hexagonal boron nitride.
For this purpose, it is required the development and the optimization of targeted nanofabrication processes. The sample fabrication requires several steps and constitutes an important part of this experimental work. Besides more conventional techniques, like micro-mechanical exfoliation of crystals and electron beam lithography to pattern the metal contacts, it is remarkable the development of a non-standard transfer procedure. The "pick-and-lift" method, also dubbed dry transfer, exploits a special polymer, the polypropylene carbonate (PPC), which changes texture above the glass transition temperature, enabling to trap and pick-up atomically thin crystals. A dedicated transfer set-up, mounted on an optical microscope coupled to a CCD camera and placed inside a glovesbox with a protective atmosphere, allows to properly align the different layers of the van der Waals heterostructure with micrometric precision.
The samples are investigated by means of magnetotransport down to 0.250 K. The collected data show the presence of a gap in encapsulated monolayer WTe_2 below temperature of ~ 100 K, whose order of magnitude is in accordance with values extracted from ARPES and STM spectra (45-55 meV) [36]. The detection of a non-zero current inside the region corresponding to the bulk bandgap, with a fairly constant value independent from gate voltage, suggests the existence of helical states. The hypothesis of edge conduction is strengthened by non-local measurements in different configurations which follow a trend in agreement with what is predicted by the Landauer-Büttiker formalism. The measured two-terminal conductance (~ 0.33 e^2/h) is smaller than the ones expected for helical states in an ideal two-dimensional topological insulator, and also the values of the non-local conductances are reduced as compared to the predictions. The motivations linked to the suppression of the edge current are still unknown, even if it is probable that in these kinds of devices the quality of the contact between the metal and the investigated crystal plays an important role.
In conclusion the data relative to selected encapsulated WTe_2 monolayer samples are in accor-

dance with the results presented by Z. Fey et al. [17] and provide evidence for edge conduction, as expected in a scenario based on a 2D topological insulator. Nevertheless, the absence of a precise conductance quantization confirms the puzzling nature of the quantum spin Hall effect and suggests that improving contacts in these devices could be a key step in the direction of a better comprehension of the phenomenon.
More in general, this experimental work demonstrates the possibility of encapsulating thin layers material in van der Waals heterostructures, preserving the crystal quality. The opportunities offered by the proposed method open up a new route for the study of air-sensitive 2D materials and for the assembly of heterostructures of increasing complexity.

Acknowledgments

Finally, here we are.
It seems almost unbelievable to be really at the *end* of this long route, especially after almost a year of “work” in Geneva, followed by some months of hard study. Many things happened during my Master and if I am approaching now the last step of this journey it’s not only thanks to my stubbornness (which is not negligible..) but it’s thanks to all the amazing people I had by my side during the way.

First of all, I would like to thank my supervisor Prof. Alberto Morpurgo to give me the opportunity to join his group one year ago and to live a first “real” academic research experience. *Grazie* Alberto for your valuable tips and your helpful observations during all stages of this experimental work.
At the same way, I would like to thank Prof. Daniela Cavalcoli, who even if geographically far, constantly supported me, with competence and kindness.
A special thanks to my *teacher* Nacho, who taught me everything I know in the laboratory, making funny even the most tedious procedure. Thanks Nacho for your endless patience and for always have been beside me inside (and outside) the lab... I know it wasn’t an easy task ;).
I am sincerely thankful to all people of the group, for the precious help during the everyday work life. The friendly environment I found at university of Geneva played definitively an important role in my decision to pursue a PhD here. I thank my office mates, David, Haijing and Marc with whom I shared many coffees and smiles. Thank you Nico for solving my last-minutes doubts and for “taking care” of my (bad) mood in this last period.. I really appreciated it.

My deepest thanks goes to my parents. Grazie mamma, grazie babbo, per *esserci* sempre e comunque e supportarmi in ogni mia scelta nel migliore dei modi. Nell’ultimo anno le nostre cene “insieme” su skype mi hanno regalato un sorriso anche nei momenti più duri. Grazie per essere così speciali, presenti e unici.
Thanks to all people of my italian world who never made me feel alone even if I was away...you are my strenght. Grazie Daniela per credere sempre in me e starmi vicino in tutti i piccoli e grandi passi della mia vita. Grazie a quelle pazze delle mie amiche, Pisa, Elga, Fra, Vale, Sere, Ludo, Simo, Ghiga..senza di voi questi anni non sarebbero stati così divertenti e indimenticabili. Grazie Chiara per essere un mio insostituibile punto di riferimento da ormai 10 anni (ma siamo davvero così vecchie?!) a questa parte.

Last but absolutely not least I would like to thank the *latinos*, my second family in Geneva. Eli, Diego, Adi, Clari, Jose, Nacho, Emy, David, Julia and Sofia... *gracias*. When I left one year ago I would have never imagined to be able to “build” such strong bonds in so a short time.

Thanks for the everyday coffees in Science II, for the barbecues at the lake and for the crazy Tuesdays (oops..) in PP. You made my Geneva life more colourful and I am happy to come back there to start everything again, *together*.

Giulia

Bibliography

[1] P. R. Wallace. "The band theory of graphite". *Phys. Rev.*, 71(9), 622–634 (1947).

[2] K. S. Novoselov, A. K. Geim, S. V. Morozov, D. Jiang, Y. Zhang, S. V. Dubonos, I. V. Grigorieva, and A. A. Firsov. "Electric field effect in atomically thin carbon films". *Science*, 306(5696), 666–669 (2004).

[3] L. D. Landau. "Zur Theorie der phasenumwandlungen II". *Phys. Z. Sowjetunion* 11 (1937).

[4] L. D. Lifshitz Landau. "E. M. Statistical Physics, Part I". *Pergamon*, Oxford (1980).

[5] N. D. Mermin. "Crystalline order in two dimensions". *Phys. Rev.*, 176, 250–254, (1968).

[6] A. F. Morpurgo. "The ABC of 2D materials". *Nature Physics* 11, 625–626 (2015).

[7] L. Wang et al. "One-dimensional electrical contact to a two-dimensional material". *Science*, 342(6158), 614–617 (2013).

[8] A. H. Castro Neto, F. Guinea, N. M. R. Peres, K. S. Novoselov, and A. K. Geim. "The electronic properties of graphene". *Rev. Mod. Phys.*, 81(1), 109–162 (2009).

[9] S. Kim et al. "High-mobility and low-power thin-film transistors based on multilayer MoS2 crystals". *Nature Commun.* 3, 1011 (2012).

[10] D. Xiao et al. "Coupled Spin and Valley Physics in Monolayers of MoS2 and Other Group-VI Dichalcogenides". *Phys. Rev. Lett.* 108, 196802 (2012).

[11] J.H Chen et al. "Intrinsic and extrinsic performance limits of graphene devices on SiO_2". *Nature Nanotech.* 3, 206–209 (2008).

[12] C. R. Dean et al. "Boron nitride substrates for high-quality graphene electronics". *Nature Nanotech.* 5, 722–726 (2010).

[13] Z. Wang et al. "Strong interface-induced spin–orbit interaction in graphene on WS2". *Nat. Commun.* 6, 8339 (2015).

[14] A. K. Geim and I. V. Grigorieva. "Van der Waals heterostructures". *Nature* 499, 419–425, (2013).

[15] Georgiou T. et al. "Vertical field-effect transistor based on graphene–WS2 heterostructures for flexible and transparent electronics". *Nature Nanotech.* 8, 100–103 (2013).

[16] A. Avsar et al. "Air-stable transport in graphene-contacted, fully encapsulated ultrathin black phosphorus-based field-effect transistors". *ACS Nano* 9, 4138–4145 (2015).

[17] Z. Fey et al. "Edge conduction in monolayer WTe_2" *Nature Physics* 13, 677-782 (2017).

[18] E. Y. Ma et al. "Unexpected edge conduction in mercury telluride quantum wells under broken time-reversal symmetry". *Nat. Commun.* 6, 7252 (2015).

[19] A. Bansil et al. "Topological band theory". *Rev. Mod. Phys.* 88, 021004-1 (2016).

[20] X.L. Qi and S.C. Zhang. "Topological insulators and superconductors". *Rev. Mod. Phys.*, 83(4):1057–1110 (2011).

[21] J.E. Moore. "The birth of topological insulators". *Nature* 464, 194 (2010).

[22] D. J. Thouless et al. "Quantized Hall Conductance in a Two-Dimensional Periodic Potential". *Phys. Rev. Lett.*, 49, 405 (1982).

[23] S. Murakami, N. Nagaosa, S. C. Zhang. "Spin-Hall insulator". *Phys. Rev. Lett.* 93, 156804 (2004).

[24] M. Z. Hasan and C. L. Kane. "Topological insulators". *Rev. Mod. Phys.* 82, 3045 (2010).

[25] C. L. Kane, E. J. Mele. "Z_2 topological order and the quantum spin Hall effect". *Phys. Rev. Lett.* 95, 146802 (2005).

[26] B. A. Bernevig, T. L. Hughes, S. C. Zhang. "Quantum spin Hall effect and topological phase transition in HgTe quantum wells". *Science* 314, 1757–1761 (2006).

[27] M. König et al. "Quantum Spin Hall Insulator State in HgTe Quantum Wells". *Science* 318, 766 (2007).

[28] I. Knez et al. "Evidence for helical edge modes in inverted InAs/GaSb quantum wells". *Phys. Rev. Lett.* 107, 136603 (2011).

[29] D. Hsieh. et al. "A topological Dirac insulator in a quantum spin Hall phase". *Nature*, 452, 970-974 (2008)

[30] H. Zhang et al. "Topological insulators in Bi_2Se_3, Bi_2Te_3 and Sb_2Te_3 with a single Dirac cone on the surface". *Nature Physics*, 5, 438-442 (2009).

[31] D. Hsieh et al. "A tunable topological insulator in the spin helical Dirac transport regime". *Nature* 460, 1101–1105 (2009).

[32] I. Garate, M. Franz. "Inverse spin-galvanic effect in a topological-insulator/ferromagnet interface". *Phys. Rev. Lett.*, 104, 146802 (2010).

[33] L. Fu, C. L. Kane. "Superconducting proximity effect and Majorana fermions at the surface of a topological insulator". *Phys. Rev. Lett.* 100, 096407 (2008).

[34] G. P. Collins. "Computing with quantum knots". *Sci. Am.* 294, 57–63 (2006).

[35] M. N. Ali et al. "Large, non-saturating magnetoresistance in WTe_2". *Nature* 514, 205-208 (2014).

[36] S. Tang et al. "Quantum spin Hall state in monolayer 1T'-WTe_2". *Nature Physics* 13, 683-688 (2017).

[37] X. Qian et al. "Quantum spin Hall effect in two-dimensional transition metal dichalcogenides". *Science* 346 (6215), 1344-1347 (2014).

[38] L. Wang et al. "Tuning magnetotransport in a compensated semimetal at the atomic scale". *Nat. Commun.* 6, 8892 (2015).

[39] X. Chen et al. "High-quality sandwiched black phosphorus heterostructure and its quantum oscillations". *Nat. Commun.* 6, 7315 (2015).

[40] B. Fallahazad et al. "Shubnikov–de Haas Oscillations of High-Mobility Holes in Monolayer and Bilayer WSe_2: Landau Level Degeneracy, Effective Mass, and Negative Compressibility". *Phys. Rev. Lett.* 116, 086601 (2016).

[41] P. Mohanty et al. "Intrinsic decoherence in mesoscopic systems". *Phys. Rev. Lett.*, 78, 3366–3369 (1997).

[42] S Washburn and R. A. Webb. "Quantum transport in small disordered samples from the diffusive to the ballistic regime". *Reports on Progress in Physics*, 55, 1311 (1992).

[43] S. Datta. "Electronic transport in mesoscopic systems" *Cambridge university press* (1995).

[44] D. Costanzo et al. "Gate-induced superconductivity in atomically thin MoS_2 crystals" *Nature Nanotech.* 11, 339-344 (2016).

[45] S. M. Sze. "Physics of semiconductor devices" *Wiley* (1981).

[46] E. H. Rhoderick. "Metal-semiconductor contacts". *Oxford* (1980).

[47] Y. Liu et al."Van der Waals metal-semiconductor junction: Weak Fermi level pinning enables effective tuning of Schottky barrier" *Science Advances*, 2 (2016).

[48] B. J. van Wees et al. "Quantized Conductance of Point Contacts in a Two-Dimensional Electron Gas" *Phys. Rev. Lett.* 60, 9 (1988).

[49] S-Q. Shen "Topological Insulators. Dirac Equation in Condensed Matters". *Springer* (2012).

[50] C. W. J. Beenakker and H. van Houten. "Quantum Transport in Semiconductor Nanostructures"*Solid State Phys.*, 44, 1-228 (1991)

[51] S. Hikami, A. I. Larkin, Y. Nagaoka. "Spin–Orbit Interaction and Magnetoresistance in the Two-Dimensional Random System". *Prog. Theor. Phys.* 63(2), 707–710 (1980).

[52] P. W. Anderson. "Absence of Diffusion in Certain Random Lattices". *Phys. Rev.* 109 (5), 1492–1505 (1958).

[53] S. Washburn and R.A. Webb. "Quantum transport in small disorder samples from the diffusive to the ballistic regime" *Rep. Prog. Phys.* 55, 1311-1383 (1992).

[54] A. Douglas Stone. "Magnetoresistance fluctuations in mesoscopic wires and rings". *Phys. Rev. Lett.* 54, 2692–2695 (1985).

[55] M. Buttiker. "Absence of backscattering in the quantum hall effect in multiprobe conductors". *Phys. Rev. B* 38, 9375–9389 (1988).

[56] H. C. Manoharan. "Topological insulators. A romance with many dimensions" *Nat. Nanotech.* 5, 477-479 (2010).

[57] E. H. Sondheimer and A. H. Wilson. "The theory of the magneto-resistance effects in metals". *Proc. R. Soc. London Series A Math. Phys. Sci.* 190, 435–455 (1947).

[58] D. J. Thouless et al. "Quantized hall conductance in a two-dimensional periodic potential". *Phys. Rev. Lett.* 49(6), 405–408 (1982).

[59] F. D. M. Haldane. "Model for a quantum hall effect without landau levels: Condensed-matter realization of the parity anomaly". *Phys. Rev. Lett.* 61(18), 2015–2018 (1988).

[60] M. Büttiker. "Edge-State Physics Without Magnetic Fields" *Science* 325, 278-279 (2009).

[61] A. Roth et al. "Nonlocal Transport in the Quantum Spin Hall State" *Science* 17, 325, 294-297 (2009).

[62] D. Rhodes et al. "Role of spin-orbit coupling and evolution of the electronic structure of WTe_2 under an external magnetic field" *Phys. Rev. B* 92, 125152 (2015).

[63] F. Ye et al. "Environmental Instability and Degradation of Single- and Few-Layer WTe_2 Nanosheets in Ambient Conditions" *Small* 12, 5802 (2016).

[64] K.S. Novoselov et al. "2D materials and van der Waals heterostructures" *Science* 353, 6298 (2016).